The Pennsylvania State University
The Graduate School
College of Engineering

AERODYNAMIC ANALYSIS OF HELICOPTER ROTORS USING A HIGHER-ORDER, FREE-WAKE METHOD

A Dissertation in
Aerospace Engineering
by
Tenzin Choephel

© 2016 Tenzin Choephel

Submitted in Partial Fulfillment
of the Requirements
for the Degree of

Doctor of Philosophy

December 2016

The dissertation of Tenzin Choephel was reviewed and approved* by the following:

Mark D. Maughmer
Professor of Aerospace Engineering
Dissertation Advisor, Chair of Committee

Kenneth S. Brentner
Professor of Aerospace Engineering

Sven Schmitz
Associate Professor of Aerospace Engineering

Virendra Puri
Distinguished Professor of Agricultural and Biological Engineering

Götz Bramesfeld
Special Member
Assistant Professor of Aerospace Engineering
Ryerson University

Phillip J. Morris
Boeing/A.D. Welliver Professor
Interim Head of the Department of Aerospace Engineering

*Signatures are on file in the Graduate School.

Abstract

The wake has a strong influence on the aerodynamics of a helicopter rotor, and the accurate prediction of its geometry and the resulting induced velocity field is extremely important for rotorcraft aerodynamic analysis. In this thesis, a new higher-order, free-wake method for rotor aerodynamic analysis is presented. The method uses elements of distributed vorticity to model the lifting surfaces and the associated wake. The use of such higher-order spanwise elements ensures higher resolution compared to traditional filament-based free-wake analysis and does not require explicit vortex core modeling with a user-specified core size. Since the method uses a full-span, singularity-free, relaxed wake, it can resolve the effect of on-blade, partial-span devices.

The free-wake method is validated in both hover and forward flight against measured data from well-documented experiments. In hover, the blade spanwise lift coefficients predicted by the free-wake analysis correlate well with the measured data from the classic Caradonna-Tung model rotor experiment. The figure of merit, which is a measure of rotor efficiency, predicted by the present method is compared to that from the experiments conducted by Knight and Hefner, and the correlations are found to be quite good given the level of fidelity of this method, which is based on potential flow theory. Rotor downwash, which is one of the most important considerations in rotor aerodynamic analysis, is predicted very well by the free-wake method when compared to measured data from a full-scale rotor test performed by Boatwright. These correlation studies provide a lot of promise as to the ability of the method in predicting the challenging aerodynamics of a helicopter rotor in hover.

Validation studies are also performed to assess the accuracy of the free-wake analysis in predicting downwash distribution in forward flight. Comparison of numerical predictions with experimental data requires the rotor to be trimmed to the conditions recorded in the experiment. To ensure this, the free-wake program is coupled with RCAS, a comprehensive helicopter analysis code developed by the

US Army, in order to take advantage of its robust trim algorithm, among other capabilities. The coupling is achieved through what is called a "loose-coupling methodology", whereby data is exchanged at the end of each coupling iteration or "converged" rotor revolution. The downwash distributions predicted by the present method are compared to measured data for a model rotor at various advanced ratios and thrust levels taken at the U.S. Army/NASA Langley Research Center (LaRC) facility. The free-wake method not only captures the important phenomena observed in the experiments but the results also correlate well with the measured data both in terms of magnitude and distribution. However, exceptions exist at the highest advance ratio, where other methods also demonstrate poor correlations. The results from this free-wake analysis are also compared to predictions by other existing methods such as the University of Maryland free-wake method (UMD-FW) and the vortex transport method (VTM). The present method yields results comparable to the ones obtained using VTM, both of which correlate better with measurements than does UMD-FW.

Sensitivity studies show that the blade panel density and azimuthal time-step size do not have a significant influence on the solution fidelity. In addition, free-wake analyses with the azimuthal time-step size of $\Delta\psi = 3^o$ demonstrate the robustness of the method even with small time-steps, which is important for certain problems including rotor acoustics.

The thesis concludes with a discussion on the capability of the new free-wake method in resolving on-blade, partial-span devices. An analysis of a 2-bladed rotor with a partial-span deflection is performed and the resulting changes in sectional loadings, downwash distribution, wake geometry and aggregate performance parameters are highlighted to demonstrate its potential as a tool for future rotorcraft analysis.

Table of Contents

List of Figures

List of Tables

List of Symbols

Letter Symbols

A, B, C	Circulation coefficients
$\{A\}$	Solution vector of circulation coefficients
c	Blade chord
cl_{α}	Airfoil lift curve slope
C_T	Thrust coefficient
C_{Mx}	Pitching moment coefficient about the longitudinal axis of the rotor
C_{My}	Pitching moment coefficient about the lateral axis of the rotor
cl_{Pot}	Section lift coefficient calculated from potential resultant force
$cl_{profile}$	Airfoil lift coefficient from the look-up table
$cd_{profile}$	Airfoil drag coefficient from the look-up table
D	Matrix of influence coefficient
e	Hinge offset
$\vec{F}_{Res\_Pot}$	Integrated potential resultant force on a spanwise distributed vorticity element
g	Vector of trim constraint forces and moments

I_β	Blade flapping inertia
k	Singualarity constant
K	Average of the integrated circulation of the distributed vorticity element
M	Time steps per revolution
N	Number of spanwise distributed vorticity elements
P	Number of blades
r_c	Root cutout
R	Rotor radius
$\{R\}$	Vector of known quantities at each time step
Re	Reynolds number
S_{Ref}	Reference area of a distributed vorticity element
T	Rotor thrust
U_∞	Freestream wind velocity
URF_Γ	Under-relaxation factor for bound circulation
URF_v	Under-relaxation factor for induced velocity
$\vec{V}_{rel}$	Component of total velocity in the plane parallel to the blade section
$\vec{V}_t$	Vector of trim variables
$\vec{V}_{total}$	Vector sum of kinematic velocity and induced velocity
$\vec{w}_1$	Velocity induced by vortex filament
w_2	Velocity induced by vortex sheet
$\vec{w}_{surface}$	Velocity induced by surface distributed vorticity elements
$\vec{w}_{wake}$	Velocity induced by wake distributed vorticity elements

Greek Symbols

α_{cl_Pot}	Angle of attack calculated from the potential resultant lift coefficient (referenced to the airfoil chordline)
α_{ZLL_Pot}	Angle of attack calculated from the potential resultant lift coefficient (referenced to the airfoil zero lift line)
α_{TPP}	Tip path plane angle of attack
β	Blade flapping angle
β_o	Coning angle
β_{1c}	Longitudinal flapping coefficient
β_{1s}	Lateral flapping coefficient
$\Delta(\Gamma)^n$	Sum of the difference between the current and the previous iteration bound circulation at the nth coupling iteration
$\Delta(v)^n$	Sum of the difference between the current and the previous iteration induced velocity at the nth coupling iteration
η, ξ, ζ	Local coordinate system of the distributed vorticity element
η_i	Half span of the distributed vorticity element
γ	Vorticity, derivative of circulation
Γ	Circulation
λ_h	Hover inflow ratio
λ_i	Inflow ratio
Λ	Sweep angle of the distributed vorticity element
μ	Advance ratio
ν	kinematic viscosity
Ω	Rotor speed
ρ	Air density
ψ	Blade azimuth angle
σ	Rotor solidity

$\sigma(v)^n$	Relative difference in induced velocity between successive iterations
θ	Blade pitch
θ_o	Collective pitch
θ_{1s}	Longitudinal cyclic coefficient
θ_{1c}	Lateral cyclic coefficient
Θ	Blade section twist angle
χ	Wake skew angle

Abbreviations

ACP	Aerodynamic Computation Point
$AFDD$	Aero Flight Dynamics Directorate
$CAMRAD$	Comprehensive Analytical Model of Rotorcraft Aerodynamics and Dynamics
CCW	Counter Clock Wise
CFD	Computational Fluid Dynamics
$CHARM$	Comprehensive Hierarchical Aeromechanics Rotorcraft Model
CVC	Constant Vorticity Contour
FM	Figure of Merit
LDV	Laser Doppler Velocimetry
$RANS$	Reynolds Averaged Navier-Stokes
$RCAS$	Rotorcraft Comprehensive Analysis System
$ROBIN$	ROtor Body INteraction
RPM	Revolution Per Minute
$UMD-FW$	University of Maryland Free-Wake
VTM	Vorticity Transport Method

$VVPM$ Viscous Vortex Particle Method

Indices

LE Leading Edge

TE Trailing Edge

Acknowledgments

This work could not have been completed without the constant support of my advisor Dr. Mark Maughmer, whose technical guidance has made me not only a better engineer but also an independent thinker. I would also like to thank Dr. Kenneth Brentner, Dr. Sven Schmitz, Dr. Virendra Puri and Dr. Götz Bramesfeld for agreeing to be in my doctoral committee and reviewing this thesis. Many thanks to the Department of Aerospace Engineering for the wonderful education I received in the course of my graduate studies. Special acknowledgment is due to the US Army for providing funding for the project from which this thesis materialized. I am indebted to my master's advisor, Dr. Edward Smith, for financially supporting me through the initial years of my graduate school and for helping me get connected with this work.

I am grateful to Dr. Hossein Saberi and Mathew Hasbun of Advanced Rotorcraft Technology Inc., who have been very patient and helpful in providing the relevant materials and answering RCAS-related questions. I must also acknowledge the few instructive communications, in person and via email, I have had with Dr. Robert Ormiston at the initial stages of this work.

Thanks are due to all of my colleagues, past and present, and friends including Frank Cody, Kevin Ferguson, Ethan Corle, Bernardo Viera, Amandeep Premi, Pankaj Jha, Jim Coder, Dave Maniaci and Regis Thedin not only for all those helpful and instructive discussions, but also for those crazy and fun-filled time we have had over the last many years, making my graduate school experience something to cherish for the rest of my life.

I would also like to acknowledge the help and support of Mr. Kirk Heller in facilitating the use of aerospace department computational resources that have been indispensable in this work. I must also thank Dr. Bramesfeld and his student Bill Bissonette at Ryerson University for suggestions on MATLAB plotting techniques. Thanks a lot, also, to the rest of the faculty and the staff for being so supportive throughout the time I have been associated with the department.

Last but not the least, I am eternally indebted to my beautiful family for always supporting me and being so patient as I continued to remain a student for so long! Lots of love to pala (miss you!), ama, chocho, acha, Silnon, Kunsel and Tsephel.

Dedication

I would like to dedicate this accomplishment to my Late father Pema Dorjee and to my mother Dorjee Bhuti for sacrificing so much for me and my siblings. I would also like to dedicate this work to my brother Ngawang Norbu who has been a father figure to us after dad passed away.

Chapter 1
Introduction

Helicopters are a class of airborne vehicles that use large-diameter rotating wings to perform efficient vertical takeoff and landing. Unlike their fixed wing counterparts, these vehicles do not depend on forward motion to generate the necessary lift to stay in the air. Not only can they hover, but also fly backwards. However, this versatility comes at a price. Helicopters are generally noisy, susceptible to aeromechanical instabilities and vibrations, and are limited in their ability to fly at high forward speeds. These are results of highly complex and nonlinear conditions in which these vehicles operate. A better understanding of the complex aerodynamic environment can potentially enhance the performance envelope of rotary wing aircraft.

The accurate modeling of helicopter flowfield is important for the improved prediction of rotor loads, performance and acoustics. In particular, rotor downwash analysis remains one of the most challenging tasks for rotor aerodynamics modeling. The interaction of the rotor wake with the rotor blades has a significant influence on the variation of blade airloads. The unsteady nature of the rotor wake causes vibration of the vehicle in hover as well as in forward flight. The wake also creates a hazardous environment around the helicopter when it is operating close to the ground, especially so in the case of helicopters and tiltrotors with high disk loading. The rotor wake prediction is also important for the determination of rotor/airframe interaction. Thus, an accurate prediction of rotor wake development is important.

1.1 Nature of the Rotor Wake

Rotary-wing aircraft generate unsteady vortical flows that are generally more complex than those associated with most flight vehicles, even though the fundamental physics is not very different. The vortical wake structures of typical single-rotor and tiltrotor aircraft are shown in Figures 1.1 and 1.2.

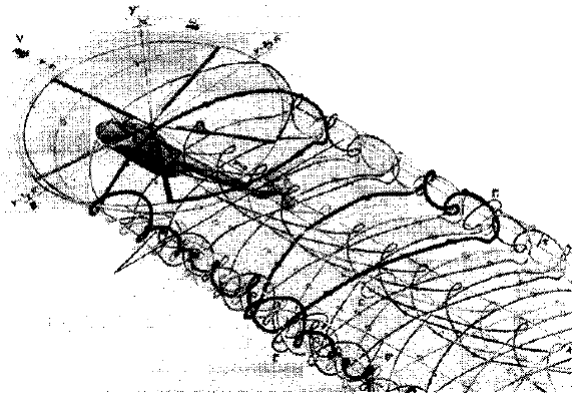

Figure 1.1. The wake structure of a helicopter rotor in forward flight characterized by a complex interaction of blade tip vortices [1].

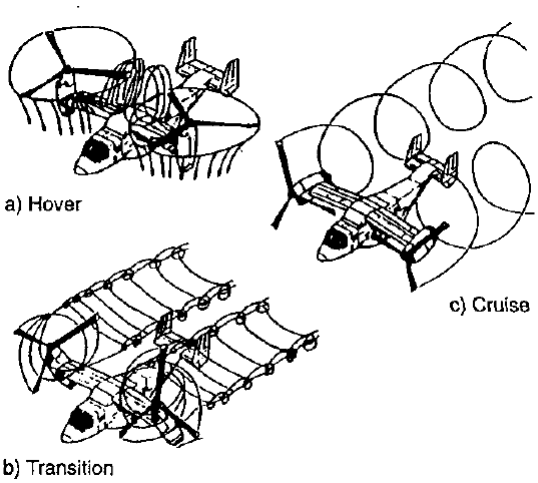

Figure 1.2. The wake structure of a tiltrotor in various flight regimes [1].

The shed vorticity from the rotor blades initially rolls up into seemingly discrete, concentrated tip vortices that remain close to the rotor for the initial few rotor

revolutions depending on the forward speed. When these vortices are close to the rotor, they induce local variations in the airflow approaching the rotating blades as well as the fuselage. These vortices also interact with themselves before convecting downstream, eventually forming a far wake that somewhat resembles the wake pattern behind a fixed-wing aircraft, characterized by two large super vortices at the right and left edges of the wake.

The wake vortices are extremely complex motions of air that are invisible to naked eye but, under certain conditions, can become visible without artificial intervention. Under the right combination of atmospheric temperature and humidity, condensation can occur in the tip vortices due to the decreased pressure in them, rendering the trajectories of the vortices visible. Figure 1.3 shows the tip vortices from a two-blade helicopter made visible by natural condensation.

Figure 1.3. Natural condensation trails generated by the tip vortices of the helicopter wake (Photo source:www.jazzroc.wordpress.com).

1.1.1 Rotor Wake in Hover

In hover, the wake is generally radially axisymmetric. Figure 1.4 shows flow visualization pictures taken in the wake of a two-bladed rotor. In the experiment, a fine mist of submicron atomized oil particles was introduced into the wake and illuminated with a thin sheet of laser light positioned on a radial plane extending

from the axis of the rotor. The sheet was pulsed once per revolution to create an instantaneous illumination of the wake [23].

Figure 1.4 shows two noteworthy flow features. First, the blade tip vortex cores are identified by the dark voids. These voids are caused by the oil particles spiraling radially outward due to the centrifugal forces in the vortices. The particles reach a radial equilibrium when the centrifugal force is balanced by the pressure force. The voids can, however, be larger than the actual viscous core size of the tip vortex. Second, as can be observed in Figure 1.4, a shear layer is trailed behind the blade, which is marked by the discontinuity in the streaklines. This shear layer, often called a "vortex sheet," is formed when the boundary layers from the upper and lower blade surfaces merge at the trailing edge. The strength of the vortex sheet is related to the spanwise change in blade bound circulation. The tip vortex and the vortex sheet are both convected below the rotor disk as the blade rotates. Also, the contraction of the wake is clearly observed by the radially inward displacement of the tip vortex cores.

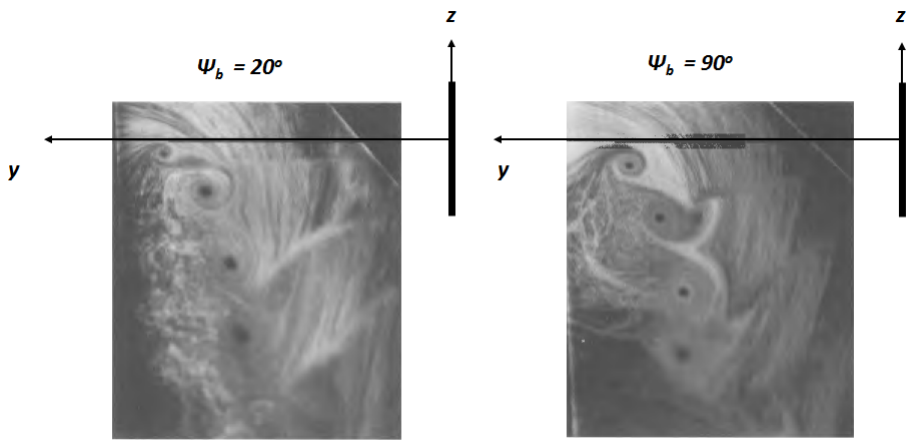

Figure 1.4. Flow visualization images of the rotor wake using laser light sheet technique. [2]

The radial contraction (y/R) and the axial convection (z/R) of the wake structures can be quantified by digitizing the flow visualization images such as those

shown in Figure 1.4. The data obtained from such procedures are often plotted, as shown in Figure 1.5. The characteristics of the tip vortex geometry shown here are representative of what would result with any lightly loaded hovering rotor. Up to the first blade passage, which happens at a wake age of $\psi_w = \frac{360^o}{\text{number of blades}}$, the tip vortices generated by either of the 1-bladed and 2-bladed rotors convect down relatively slowly. The axial convection increases abruptly after the first blade passage. At the same time, the radial position of the tip vortices contracts to an asymptotic value of approximately $y/R \approx 0.78$.

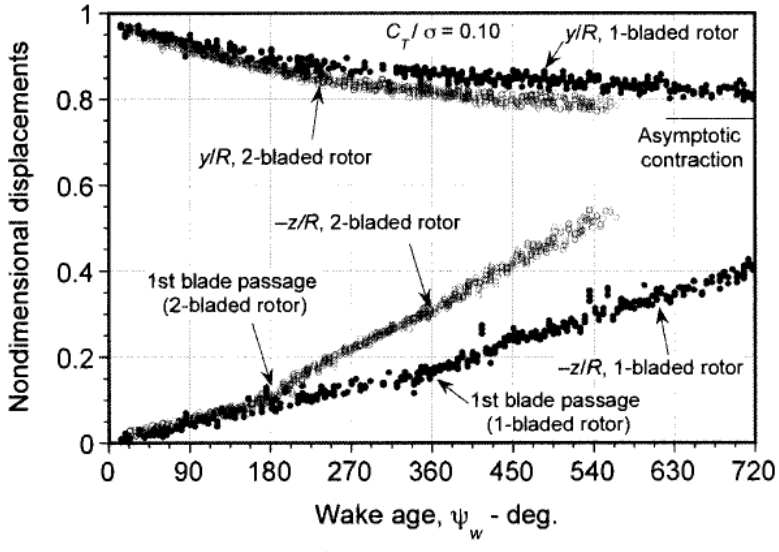

Figure 1.5. Movements of the tip vortices from one- and two-bladed rotors in hover. $C_T/\sigma = 0.1$ [3].

The tip vortex and the vortex sheet undergo complex mutual interaction as they develop. This interaction is beautifully illustrated by Leishman [2] and shown in Figure 1.6. The data points have been obtained by digitizing the flow visualization images such as those shown in Figure 1.4. The vortex sheet is initially trailed along the length of the blade and is relatively straight, with a rolled-up tip vortex at the blade tip. The tip vortex and the vortex sheet then convect axially below the rotor disk. Since the induced downwash is highest near the blade tip, the sheet convects more rapidly below the tip region, while becoming progressively more inclined to

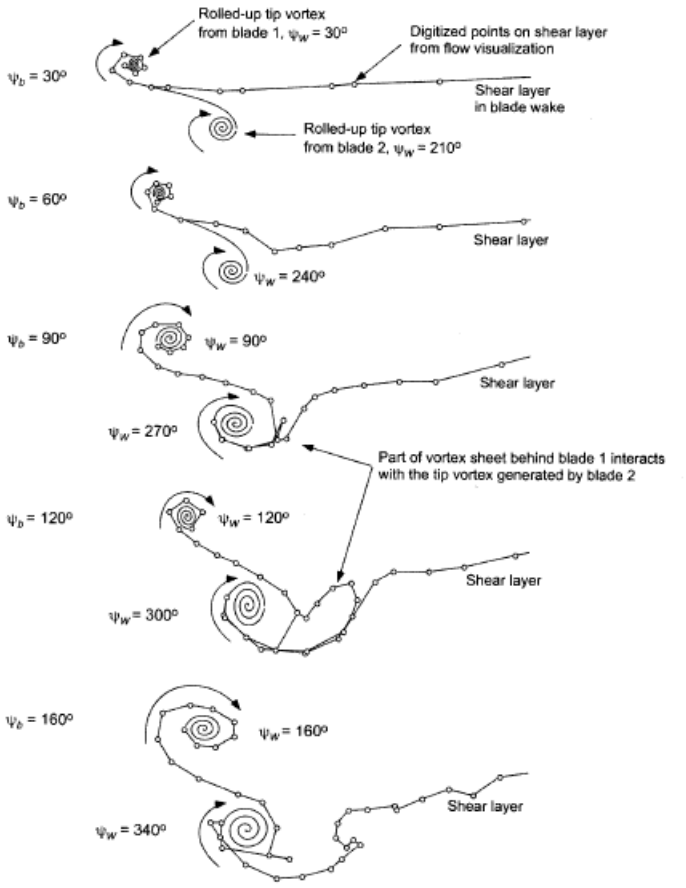

Figure 1.6. Interaction of tip vortices shed from the blades in hover. [2]

the disk plane. The vortex sheet also interacts with the tip vortex generated by another blade, resulting in complex interactions.

1.1.2 Rotor Wake in Forward Flight

The rotor wake in hover was observed to be nominally axisymmetric. However, the same cannot be said about the rotor wake in forward flight, thanks to the forward or edgwise component of velocity at the rotor plane. The wake is convected not only below but also behind the rotor, resulting in a complicated structure. Figure 1.7 shows the general features of a rotor wake in forward flight, where smoke was released from the blade tips to track the vortex trajectories. The tip vortices are initially formed as a series of interlocking epicycloids. Mutual interactions between

the filaments result in distortion of the vortices, mostly in the plane perpendicular to the disk plane. This distortion is especially strong at low advance ratios, where the vortices are closest together. It can also be observed that the wake elements along the lateral edges roll up into what are called "super vortices", structures that resemble the wake roll-up behind fixed-wing aircraft.

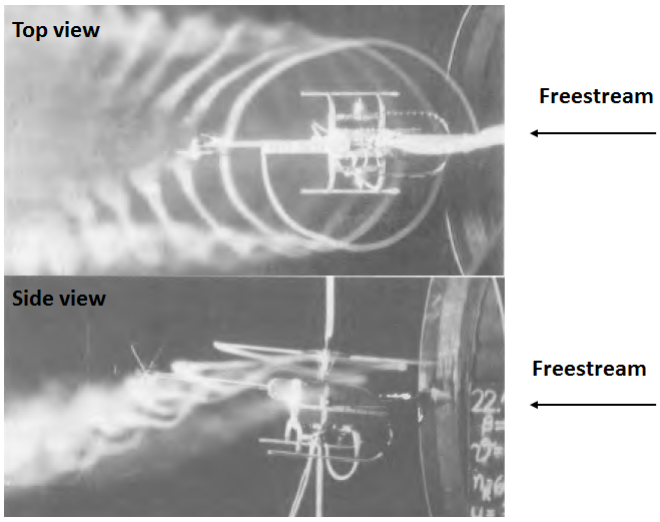

Figure 1.7. Smoke flow visualization of the wake of a two-bladed rotor in forward flight (Photo: Reinert Muller).

Leishman and Bagai [2] performed experiments using the technique of shadowgraphy to examine the positions of the tip vortices generated by an isolated rotor. Wake boundaries obtained from the experiments are shown in Figure 1.8 for a rotor in hover and in forward flight at three advance ratios. One can observe that the vortices at the leading edge of the disk are initially convected above the rotor tip path plane within the first 90^o of wake age. This is because of the presence of a small region of upwash at the front of the disk and a strong longitudinal inflow gradient. On the other hand, at the rear of the disk, the vortices are convected quickly away from the rotor.

An distinctive feature of the wake dynamics in forward flight is that, due to the proximity of the vortices generated by the blades, the tip vortices can interact with the blades in a number of ways. This phenomenon is called blade-vortex

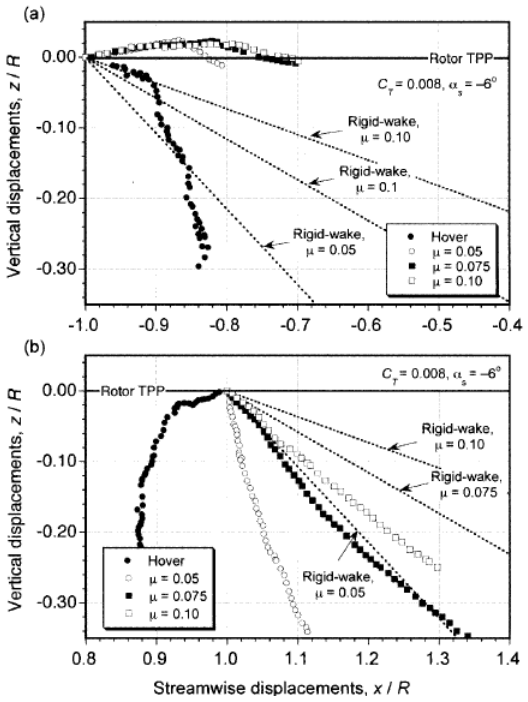

Figure 1.8. Tip vortex positions in a plane parallel to the longitudinal centerline of an isolated, four-bladed rotor at $C_T = 0.008$ and a shaft tilt angle of 3^o. (a) Front of the disk. (b) Rear of the disk. [2]

interactions or BVIs. BVIs can result in highly unsteady local airloads on the blades, which can cause significant noise with focused directivity [24]. Examples of the tip-vortex interaction when viewed from above a two-bladed rotor is shown for three advance ratios in Figure 1.9. It can be seen that BVIs can occur at many different locations over the disk, with different orientations between the blade axes and the vortices. The largest number of BVIs can occur at low advance ratios, where the vortices are convected downstream at relatively slower rates.

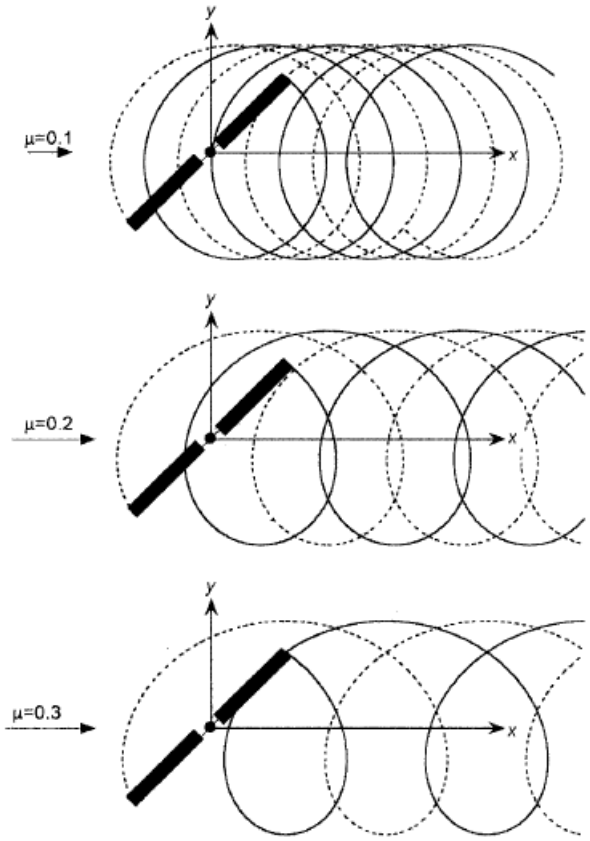

Figure 1.9. Top view of the tip vortex trajectories for a two-bladed rotor in forward flight. [2]

1.2 A Review of Analysis Methods for Rotor Wake Dynamics and Induced Inflow

Engineers have used various approaches to model the effect of the helicopter rotor wake and its resulting induced velocity field. These methods include classical momentum theory, potential flow theory, and the Eulerian grid-based methods such as computational fluid dynamics (CFD). Each of these methods will be briefly reviewed in the following sections. It should be mentioned here that the terms “inflow”, “induced inflow”, “downwash”,“induced downwash” and “induced downwash velocity” are all used to refer to the same thing in this thesis.

1.2.1 Momentum Theory

Momentum theory was the first analytical tool available to early helicopter designers. It is based on the application of the three basic conservation laws (conservation of mass, momentum and energy) to a control volume enclosing the rotor and its flowfields. This approach allows a first order analysis of rotor performance, such as power and thrust, without actually considering the details of what is happening locally at the blade section. The momentum theory was first developed by Rankine [25] for the analysis of marine propellers. The theory was further developed by W. Froude [26] and R.E. Froude [27], Lanchester [28], and Betz [29]. The fundamental assumption in the momentum theory is that the rotor can be treated as an "actuator disk," which is an infinitely thin surface that supports a pressure difference across it. This pressure difference generates a net thrust. Power is required to generate the thrust, which is supplied in the form of torque to the rotor shaft. Work that is done on the rotor results in a gain in kinetic energy of the rotor slipstream which is an energy loss and is referred to as induced power. Momentum theory was formally generalized by Glauert [30, 31].

The basic conservation laws (of mass, momentum and energy for steady, inviscid, and incompressible flow) can be applied to a rotor in hover to relate the rotor thrust to the induced velocity at the rotor disk plane to obtain

$$\lambda_h \equiv \lambda_i = \frac{1}{\Omega R}\sqrt{\frac{T}{2\rho A}} = \frac{1}{\Omega R}\sqrt{\frac{T}{A}\frac{1}{2\rho}} \tag{1.1}$$

where λ is called inflow ratio, which is the induced downwash velocity at the rotor disk normalized by the tip speed. Inflow is an important quantity in rotor aerodynamics because it changes the effective angle of attack at which the blade sections see the local freestream velocity.

It also follows from a control volume analysis that $v_\infty = 2v_i$ This means that the rotor wake contracts as the fluid velocity approaches v_∞ far from the rotor-disk.

The wake radius far from the disk is found to be $r_\infty = \frac{1}{\sqrt{2}}R$. The factor $\frac{1}{\sqrt{2}}$ is called the contraction ratio.

A similar analysis can be performed for a rotor in forward flight to yield the implicit equation

$$\lambda = \mu \tan\alpha + \frac{C_T}{2\sqrt{\mu^2 + \lambda^2}} \tag{1.2}$$

A numerical procedure, such as fixed-point iteration or Newton-Raphson iteration, is generally used to solve for λ.

Two comments must be made with respect to the above relations. First, the inflow derived in this way does not account for the presence of a discrete number of blades, and second, the induced velocity is applied uniformly over the entire rotor disk, which is why this situation is also referred to as 'uniform inflow'. Hence, the wake velocity fields computed using momentum theory in the early works are not very accurate. An approach called blade element theory was later combined with the basic momentum theory to improve the predictive capability.

In blade element theory (or BET), the blade is considered to be made up of a number of aerodynamically independent chordwise strips or elements. With this approach, two-dimensional airfoil characteristics can be used to compute the forces and moments experienced by the blade section locally at any span station. In using momentum theory, when the chord at the tip is finite, BET yields a nonzero lift all the way out to the end of the blade. In reality, the lift drops to zero at the tip because of three-dimensional flow effects, as shown in Figure 1.10. The loss of lift at the tip is an important consideration in computing the rotor performance which, if neglected, will lead to a significant overestimation of the rotor performance.

An approximate method to account for the tip losses is to assume that the blade sections outboard of the radial location $r = BR$ contribute to profile drag but generate no lift. The parameter B is called tip loss factor. Prandtl derived an expression based on a two-dimensional model of the rotor wake, which for a low

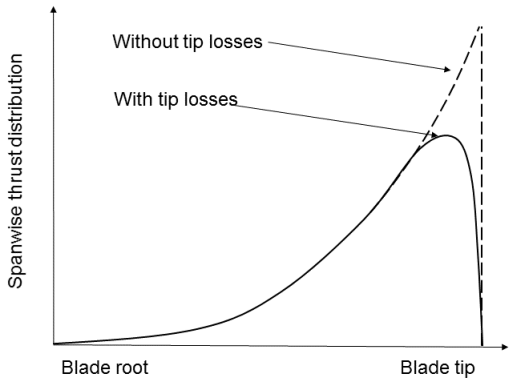

Figure 1.10. Tip-loss effect at the blade tip region.

inflow rotor, is given by

$$B = 1 - \frac{\sqrt{2C_T}}{N} \tag{1.3}$$

Typically, this gives $B = 0.96$ to 0.98.

An approach called blade element momentum theory (or BEMT) was first proposed by Gustafson and Gessow [32], and Gessow [33] for hovering helicopter rotors. The method involves invoking the equivalence of the thrust calculated from momentum theory and blade element theory. For hover, this results in

$$\lambda(r) \equiv \lambda_i(r) = \frac{\sigma C_{l_\alpha}}{16}\left(\sqrt{1 + \frac{32}{\sigma C_{l_\alpha}}\theta r} - 1\right) \tag{1.4}$$

Eq. (1.4), inflow can be solved as a function of radius for any given blade pitch, blade twist distribution, planform, and airfoil section.

In practical applications, Eq. (1.4) is solved numerically, allowing incorporation of arbitrary radial twist variations, planform etc. The blade is discretized into a number of elements of span Δr. The inflow is solved numerically using the discretized equation

$$\lambda(r_n) = \frac{\sigma C_{l_\alpha}}{16}\left(\sqrt{1 + \frac{32}{\sigma C_{l_\alpha}}\theta(r_n) r_n} - 1\right) \tag{1.5}$$

where $n = 1, N$ is the span element location, r_n the radius and $\theta(r_n)$ the blade pitch at the mid-span of each of the elements.

Using the formulation of Eq. (1.5), inflow is computed at a constant value of thrust and shown in Figure 1.11 for a rectangular blade with different linear twist rates. It can be observed that the inflow for a blade with ideal twist is uniform, which yields a linear variation of lift from the root to the tip.

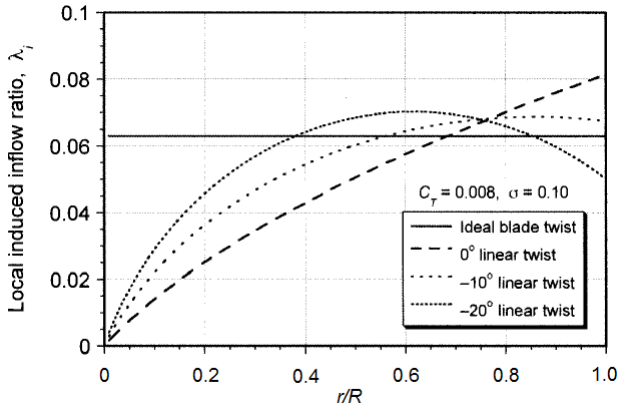

Figure 1.11. Spanwise inflow distribution predicted with BEMT. [2]

1.2.2 Classical Inflow Models

In forward flight, inflow is often calculated with the help of what are called "inflow models," which are formulated on the basis of experimental results or more advanced vortex theories etc. Since they are simple to use, inflow models have been used in many problems in helicopter aerodynamics, aeroelasticity, and flight dynamics. Two such inflow models are briefly described here.

1.2.2.1 Linear Inflow Models

The variation of inflow, based on the original form suggested by Glauert [34], is expressed as

$$\lambda_i = \lambda_o \left(1 + k_x \frac{x}{R} + k_y \frac{y}{R}\right) = \lambda_o (1 + k_x r \cos\psi + k_y r \sin\psi) \tag{1.6}$$

where k_x and k_y are constants representing the deviation of the inflow from the uniform value predicted by the simple momentum theory. Linear inflow models attempt to approximate the physical inflow distribution on the rotor as shown in Figure 1.12.

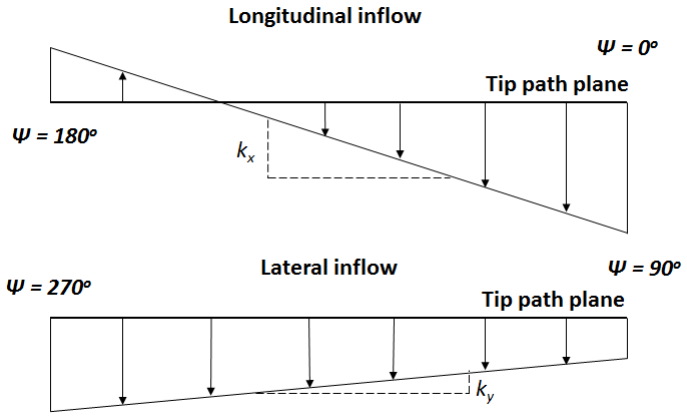

Figure 1.12. Inflow as approximated by linear inflow models.

One approximation of k_x used by Coleman et al. [35] is given by

$$k_x = \tan\left(\frac{\chi}{2}\right) \tag{1.7}$$

where χ is the wake skew angle and is given by $\tan^{-1}\left(\frac{\mu_x}{\mu_z + \lambda_i}\right)$. μ_x and μ_z are advance ratios defined parallel and normal to the rotor disk. k_x approaches unity for high-speed forward flight and does not result in the small region of upwash usually measured at the front of the rotor disk.

Another model used for approximating k_x and k_y is attributed to Drees [36]. According to Drees model, the coefficients are approximated by

$$k_x = \frac{4}{3}\left(\frac{1 - \cos\chi - 1.8\mu^2}{\sin\chi}\right) \quad and \quad k_y = -2\mu. \tag{1.8}$$

The approximations to the coefficients k_x and k_y suggested by various researchers is summarized in table 1.1.

Author(s)	k_x	k_y
Coleman et al. [35]	$\tan\frac{\chi}{2}$	0
Drees [36]	$\frac{4}{3}\frac{(1-\cos\chi-1.8\mu^2)}{\sin\chi}$	-2μ
Payne [37]	$\frac{4}{3}\frac{\mu}{\lambda(1.2+\frac{\mu}{\lambda})}$	0
White and Blake [38]	$\sqrt{2}\sin\chi$	0
Pitt and Peters [39]	$\frac{15\pi}{23}\tan\frac{\chi}{2}$	0
Howlett [40]	$\sin^{\chi}$	0

Table 1.1. Approximations to the coefficients k_x and k_y

In general, the approximations suggested by Drees [36], Payne [37] and Pitt and Peters [39] are found to compare the best with experimental results.

1.2.2.2 Inflow Model of Mangler and Squire

Another inflow model that has been used in rotor analyses is that proposed by Mangler and Squire [4]. The method is based on using incompressible, linearized Euler equations to relate the pressure field across the rotor disk to an induced inflow. The loading on the rotor disk is expressed as a linear combination of two basic distributions: Type-I, which is an elliptical distribution, and Type-III, which is a loading that goes to zero at the center and the edges of the rotor disk. The two loading types are illustrated in Figure 1.13. The loading can be expressed as

$$\Delta p_m \propto r^{m-1}\sqrt{1-r^2}, \quad m = 1, 3 \tag{1.9}$$

The idea is that, although these two types of loadings represent the two extremes, the actual loading on the disk will likely comprise a combination of the two such that

$$\Delta p = w_1\Delta p_1 + w_2\Delta p_2, \quad w_1 + w_2 = 1 \tag{1.10}$$

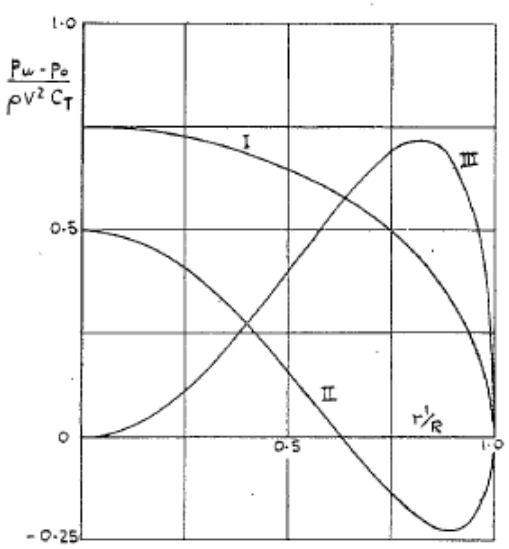

Figure 1.13. Type-I and Type-III loadings used by Mangler and Squire [4]

The inflow resulting from the assumed loading distribution is written as a Fourier series

$$\lambda_i = \frac{2C_T}{\mu}\left[\frac{c_0}{2} + \sum_{n=1}^{\infty}(-1)^n c_n(r,\alpha)\cos n\psi\right] \tag{1.11}$$

where α is the disk angle of attack. The coefficients in Eq. (1.11) are determined from the assumed loading.

The disadvantage of this method is that it requires the loading on the rotor to be either known or assumed a priori.

1.2.2.3 Dynamic Inflow

Dynamic inflow models or "finite-state wake models" are often used for stability analysis and real-time simulations. The basic idea of these models can be thought of as being based on the steady inflow model used by Mangler and Squire [4]. In these models, the effects of the wake are represented as a set of ordinary differential equations (ODEs), relating the rotor inflow and the aerodynamic loadings. The

most popular model of dynamic inflow is that developed by and Pitt and Peters [41], which was later extended and generalized by Peters et al. [42].

To formulate the dynamic inflow equations, momentum theory can be used to derive the relationships between the aerodynamic forces and pitching moments with the inflow across the disk. The thrust, T, can be expressed as the change in momentum through the rotor disk, that is,

$$T = 2\rho \int_0^R \int_0^{2\pi} v^2 r d\psi dr, \tag{1.12}$$

where v is the inflow or induced downwash. Similarly, the pitching moment (positive nose-up) is given by

$$M_y = -2\rho \int_0^R \int_0^{2\pi} v^2 r^2 \cos\psi d\psi dr, \tag{1.13}$$

and the rolling moment (positive roll to the starboard) is given by

$$M_x = -2\rho \int_0^R \int_0^{2\pi} v^2 r^2 \sin\psi d\psi dr, \tag{1.14}$$

The inflow, again, is expressed as a linear distribution of the form

$$v = v(r, \psi) = v_0 + v_c r \cos\psi + v_s r \sin\psi, \tag{1.15}$$

where v_0, v_c and v_s are the uniform, longitudinal, and lateral contributions to the inflow, respectively. The Eqs. (1.12), (1.13) and (1.14), along with the representation in Eq. (1.15), relate the aerodynamic loadings to the induced velocity field, which can be expressed in matrix form as

$$\begin{Bmatrix} v_0 \\ v_c \\ v_s \end{Bmatrix} = [L] \begin{Bmatrix} C_T \\ C_{M_y} \\ C_{M_x} \end{Bmatrix} \tag{1.16}$$

where $[L]$ is called a coupling or 'gain matrix'. The vector on the right hand side comprises of only aerodynamic contributions. The time lag in the development of wake are introduced through the use of a time constant matrix $[\tau] = [L][M]$, where $[M]$ is a matrix of unsteady terms. With this definition, the dynamic inflow model is written as

$$[\tau] \begin{Bmatrix} \dot{v_0} \\ \dot{v_c} \\ \dot{v_s} \end{Bmatrix} + \begin{Bmatrix} v_0 \\ v_c \\ v_s \end{Bmatrix} = [L] \begin{Bmatrix} C_T \\ C_{M_y} \\ C_{M_x} \end{Bmatrix} \tag{1.17}$$

or

$$[M] \begin{Bmatrix} \dot{v_0} \\ \dot{v_c} \\ \dot{v_s} \end{Bmatrix} + [L]^{-1} \begin{Bmatrix} v_0 \\ v_c \\ v_s \end{Bmatrix} = \begin{Bmatrix} C_T \\ C_{M_y} \\ C_{M_x} \end{Bmatrix} \tag{1.18}$$

These ODEs relate the unsteady inflow to the rotor thrust and pitching moments. The time constants are functions of the wake skew angle. Dynamic inflow is a global, low frequency model for the wake-induced velocity. The model is generally sufficient to capture wake effects on the dynamic behavior of the lowest-frequency blade modes and the aircraft flight dynamics [43]. These models have been used in various problems in rotor aeroelasticity and flight dynamics [44]; however, the limitation of this model is that it is basically a linear model.

In summary, while momentum theory can be modified and improved with empirical corrections, including a provision for tip loss factor to account for the effect of the rotor wake, and blade element treatment, it is insufficient for the level of accuracy needed for routine design studies performed in the industry. For example, Figure 1.14 shows experimental results for the lateral flapping angle and compares it with predictions using uniform inflow, undistorted wake and free wake. Obviously, uniform inflow predictions are way off compared to the experimental

data. Another approach that is widely used in evaluating the induced inflow is that based on potential flow theory, which will be discussed next.

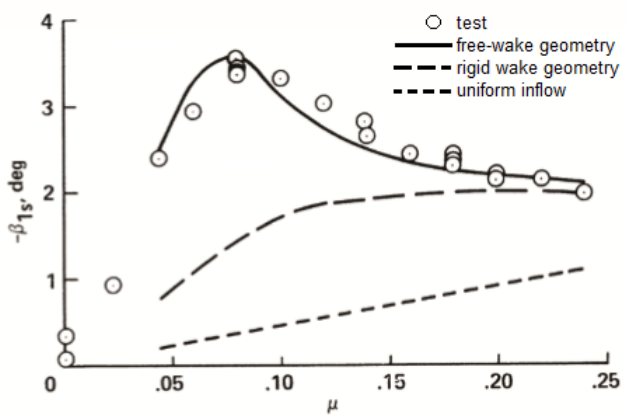

Figure 1.14. Calculation of lateral flapping angle using various wake models compared to experiment. [5]

1.2.3 Vortex Wake Methods

Vortex wake methods are based on potential flow theory, which is formulated with the assumption that the flow is inviscid and that no-slip condition is replaced with flow tangency at what are called control points. The lifting surfaces are replaced with singularities to satisfy flow tangency. Generally, lifting surfaces such as wings and rotor blades are modeled with vortex singularities. Specifically, the lift distribution is approximated by lifting-lines, vortex-lattices or vortex panels. In keeping with the Helmholtz vortex laws, these vortices cannot begin or end in the flow field and must continue from the surface into the wake.

There are three ways of handling the wake: fixed or rigid wake models, prescribed wake models, or free-wake models. Each of these models will be described briefly.

1.2.3.1 Fixed- or Rigid-Wake Methods

In fixed-wake model, the wake once generated remains in the same initial position and is unaffected by the flow field, but induces velocities on the lifting surfaces. The trailed vortices are represented by skewed helical filaments. The position of the filaments is defined geometrically and based on the flight conditions and momentum theory. For example, using a cartesian coordinate system centered at the rotor hub, the x, y, and z components of the vortex filaments are defined as

$$\begin{aligned} \frac{x}{R} &= \frac{r}{R}\cos(\psi - \phi) + \mu_x\phi + \lambda_x\phi \\ \frac{y}{R} &= \frac{r}{R}\sin(\psi - \phi) + \mu_y\phi + \lambda_y\phi \\ \frac{z}{R} &= \frac{r}{R} + \mu_z\phi + \lambda_z\phi \end{aligned} \tag{1.19}$$

where ψ is the azimuthal angle of the reference blade, and ϕ is the vortex wake age. μ_x, μ_y, and μ_z are the advance ratio components along x, y and z directions. The uniform inflow model proposed by Gluaert (Eq. (1.2)) is used to estimate the induced inflow components λ_x, λ_y, and λ_z. Figure 1.15 shows a comparison between a numerical rigid wake and a corresponding experimental wake structure for a rotor in hover.

Fixed-wake models do not predict the contraction of the wake in hover, which leads to blade load calculations that differ significantly from experiment as rotor solidity, thrust level, and tip Mach number are increased [45]. The predicted wake geometries also differ significantly from the reality in edgwise flow. Having said that, the advantages of this wake model, however, lie in its simplicity, numerical efficiency, and its ability to reasonably model the primary effects of the wake skewness in forward flight.

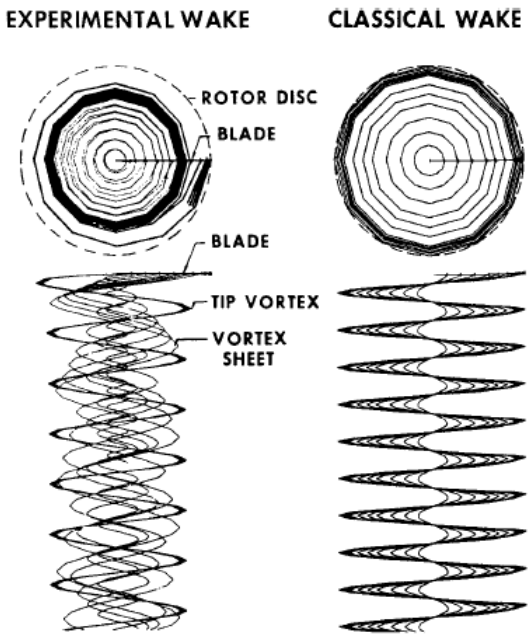

Figure 1.15. Comparison of rigid rotor wake in hover with experiment [6].

1.2.3.2 Prescribed-Wake Methods

In prescribed-wake models, the positions of the vortices are updated as a function of the wake age based on empirical data, such that the wake contraction effect is taken into account. Much of this method was developed using careful analysis of photographs to track vortex trajectories. Landgrebe did a pioneering work in implementing a prescribed wake model for the analysis of rotor wake geometry [6]. He used smoke emitted from rakes in a single place for visualization of the wake of a two-bladed rotor. Figure 1.16 shows the cross-section of the wake. Both the tip-vortex and the inboard vortex sheet are visible in the figure. Also a significant wake contraction can be observed which is predicted by momentum theory as discussed earlier.

These experimental studies of the rotor wake were used in the development of analytical expressions for the time-averaged radial and axial positions of the wake. The axial coordinate of the tip-vortex is described by an expression of the form

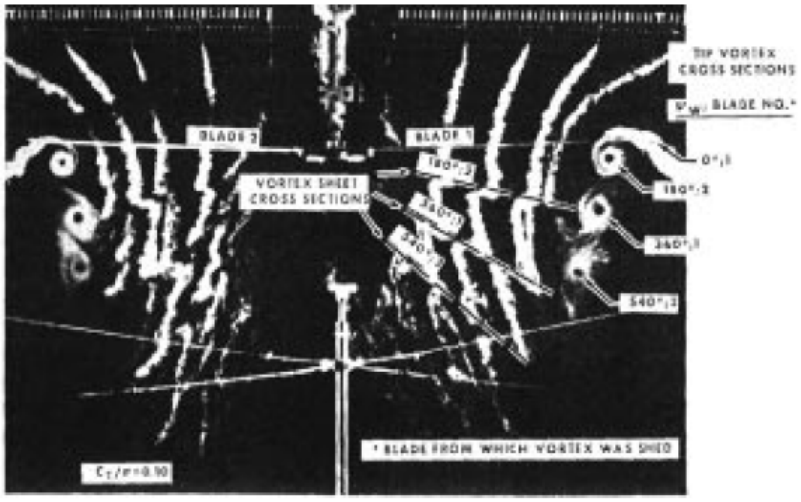

Figure 1.16. Cross-section of smoke flow visualization of a two-bladed rotor from Landgrebe [6].

$$\begin{aligned} \bar{z} &= k_1 \psi_w \quad for \quad 0 \le \psi_w \le \frac{2\pi}{b} \\ \bar{z} &= \bar{z}_{\psi_w} = \frac{2\pi}{b} + k_2(\psi_w - \frac{2\pi}{b}) \quad for \quad \psi_w \ge \frac{2\pi}{b} \end{aligned} \tag{1.20}$$

where $\bar{z}$ is a nondimensional distance below the rotor disk and is normalized by the rotor radius. ψ_w is the azimuthal wake coordinate relative to the blade, and b is the number of blades. k_1 and k_2 are parameters which are obtained from experiment. k_1 is observed to vary linearly with C_T/σ, and k_2 is observed to vary linearly with $\sqrt{C_T}$. The radial location of the tip-vortex was found to correlate well with an expression of the form

$$\bar{r} = A + (1 - A)e^{\lambda_w \psi_w} \tag{1.21}$$

where $A = 0.78$, $\lambda_w = 0.145 + 27C_T$, and $\bar{r}$ is a nondimensional distance normalized by rotor radius.

The rate of decent of an element of the tip-vortex is essentially constant before it passes beneath the following blade, at which time it jumps to another constant descent speed. These formulas are used in prescribed wake models to compute

the rotor airloads. Similar formulas are suggested by Gray [46]. A correction to these formulas was developed by Kocurek and Tangler [47]. Prescribed wake methods are very efficient computationally; however, experimental data is required such that this method is not truly predictive. This method has been extended to numerical computation of rotor airloads for a range of flight conditions by Egolf and Landgrebe [48].

While rigid wake and prescribed wake methods keep the computational expenses low, they do not represent the actual physics involved and depend on the empirical data. In comparison with the above two approaches, free-vortex wake methods, or simply "free-wake methods," are the most realistic from the physics point of view and will be discussed next.

1.2.3.3 Free Vortex Wake Methods

In free vortex wake methods, the wake is allowed to develop and deform freely due to the influence of velocities induced by the wake elements and lifting surfaces. This is the industry standard today, and with computers becoming faster and more powerful, the free-wake calculation has become more and more practical.

In free-wake methods, two types of solution methodologies have been used: 1. The so-called time-stepping, time-marching, or time-accurate methods, and 2. Relaxation, iterative, or spatial-relaxation methods. In a time-stepping method, the simulation may or may not start with an initial wake configuration. Wake rows are generated and relaxed at each time step until a steady solution, based on the convergence of a certain aerodynamic quantity, is achieved. In a relaxation method, starting with an initial wake configuration attached to the blade, the wake is relaxed until its geometry no longer distorts between successive iterations.

Relaxation Methods

Scully [49], and Clark and Leiper [50] made pioneering contributions in the development of an iterative method for the free-wake analysis of helicopter rotors. In Ref. [50], for example, the trailed vorticity is discretized into several filaments and each of the filament is further discretized into straight line segments. The procedure involves starting the computation with an initial rigid wake geometry, and allowing it to reconfigure itself based on the velocity field induced by the previous wake structure. This velocity field is calculated by taking the average of the velocity at a point in the flowfield from the previous iteration and the predicted velocity field from a wake configuration that is distorted by the blade rotation only. The iterations are performed until the wake positions no longer change between successive iterations. The near, relaxed-wake region consists of two revolutions, and a far boundary condition wake consists of about thirty ring vortices.

Scully [51], in a major revision to his 1967 effort, presented an iterative scheme to compute the distortions to the tip vortex geometries due to their mutual interactions. The tip vortex configurations are updated at each iteration by accounting for the self-induced distortions. A weighted averaging scheme is used to update the wake geometry whereby the current distortion function is averaged with the distortions from the previous computations. The wake is typically allowed to distort for two iterations. A rigid/prescribed inboard sheet is also included in the model. In hover analysis, six to twelve turns of free-wake geometry are computed, with a semi-infinite vortex cylinder below that to account for the far wake boundary condition. In forward flight, two to four turns of the vortex filaments are used, depending on the advance ratio. This method is used in this work to compute the higher-harmonic rotor airloads. The approach described above was later adopted by Johnson [52], and implemented in his computer program, CAMRAD (A Comprehensive Analytical Model for Rotorcraft Aerodynamics and Dynamics).

In 1983, Bliss et al. [53] developed an influence coefficient method based on a Newton-Raphson type iterative approach to analyze rotors in hover and axial climb.

The rotor wake was modeled using curved vortex filaments.

Later, Miller and Bliss [7] developed a method that solved the free-wake problem in an iterative, non-Lagrangian fashion that avoided the time domain problem. In the time-marching approach, the wake collocation points are identified as Lagrangian fluid markers that move with the local fluid velocity with time, and the updated locations of these points are determined by integrating the wake equations over a finite azimuthal step. In this new iterative approach, the azimuthal or time variable is transformed into what is called a "constant age" variable, which is defined as the difference between the current time and the time that a Lagrangian point was generated from the blade. If t is the current time and τ the time that collocation points were introduced into the wake at the upstream end of the filament, the constant age parameter is given as $\alpha = t - \tau$. With this definition, the age, α, of a Lagrangian marker on a vortex filament will vary from zero at the blade to some maximum value defined by the maximum length of the filament. The Lagrangian collocation points may be defined by the position function $\vec{R}(\tau, t)$. With the above transformation of the time variable into constant age parameter, the position of a collocation point, i, may be defined as $\vec{X}_i(t) = \vec{R}(\alpha_i, t)$. Under a steady-state condition, the collocation point returns to the same location each period. For example, a point with a constant age of zero will always be located at the trailing edge of the blade and will return to the same position after each revolution. Figure 1.17 shows a comparison between the Lagrangian and the constant-age description for a single blade over one rotor period (revolution).

Since for a constant angular velocity of the rotor, $t \propto \psi$, a boundary condition is defined that enforces wake periodicity in the azimuthal (time) direction as

$$\vec{X}_i(\psi + n2\pi) = \vec{X}_i(\psi) \quad where \quad n = \pm 0, 1, 2, ..., \infty \tag{1.22}$$

The induced velocities determined from the Biot-Savart law are linearized, and the wake partial differential equations are solved in a perturbation form.The

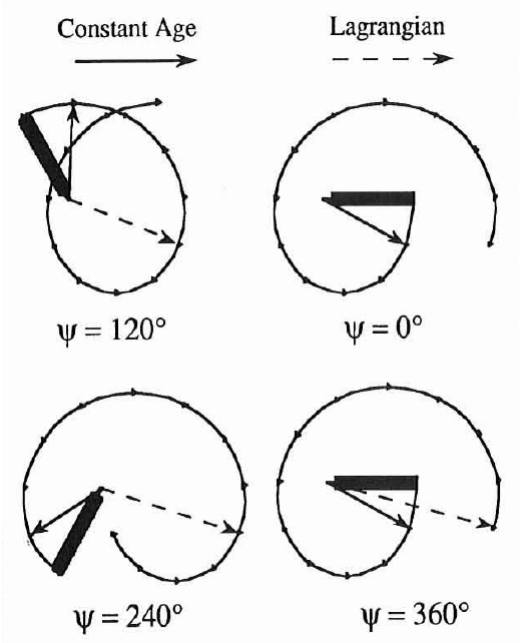

Figure 1.17. Constant age vs. Lagrangian points over one rotor period, with both initially coincident at $\psi = 0^o$ [7].

resulting PDE's are discretized using an explicit Lax-Wendroff finite differencing scheme that is second order accurate in space and time.

Bagai [54], and Bagai and Leishman [8] developed an iterative scheme, which uses the basic idea of the constant age variable described earlier. In this method, the wake is modeled with vortex filaments emanating near the tip of the blades. In the numerical implementation, these filaments are discretized into straight line segments connected by collocation points, as shown in Figure 1.18.

By assuming that every vortex filament (collocation point) is convected through the flow field at the local velocity, a partial differential equation governing the geometry of a single vortex filament is given by

$$\frac{\partial \vec{r}(\psi,\zeta)}{\partial \psi} + \frac{\partial \vec{r}(\psi,\zeta)}{\partial \zeta} = \frac{\vec{V}_\infty}{\Omega} + \frac{1}{\Omega}\sum_{j=1}^{N_v} \vec{V}_{ind}(\vec{r}(\psi,\zeta), \vec{r}(\psi_j,\zeta)) \tag{1.23}$$

where N_v is the number of tip vortex filaments.

The summation is performed over all the trailed vortex filaments in the flow

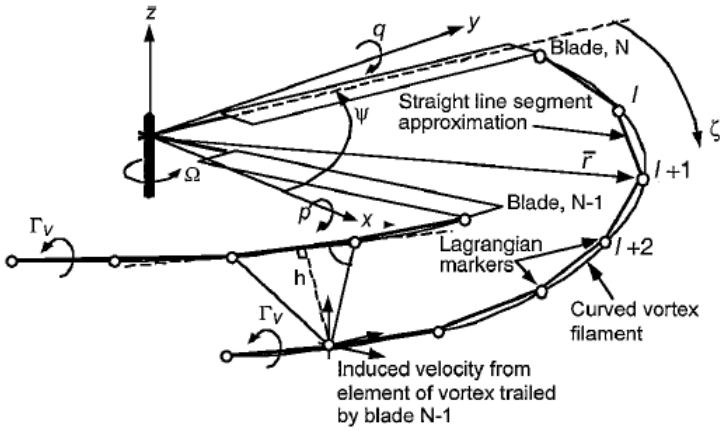

Figure 1.18. Discretized wake system [8].

field that contribute to the induced velocity at the computation point in question. The induced velocity in equation 1.23 is computed using the Biot-Savart law

$$\vec{V}_{ind}(\vec{r}(\psi,\zeta),\vec{r}(\psi_j,\zeta)) = \frac{1}{4\pi}\int \frac{\Gamma(\psi_j,\zeta)d\vec{\zeta_j}(\vec{r}(\psi,\zeta)-\vec{r}(\psi_j,\zeta))}{|\vec{r}(\psi,\zeta)-\vec{r}(\psi_j,\zeta)|^3} \tag{1.24}$$

where $\vec{r}(\psi,\zeta)$ is the point in the flow field that is influenced by the j^{th} vortex at $\vec{r}(\psi_j,\zeta)$ with strength $\Gamma(\psi_j,\zeta)$.

To solve the vortex convection PDE, it is spatially and temporally discretized. A computational domain is defined as a discretized grid in time (ψ) and space (ζ). The partial derivatives in the governing PDE are discretized using a finite-difference approximation. Bagai and Leishman [8] uses a 'five-point central diffference' scheme, where the derivatives are evaluated at the point $(k-1/2, i-1/2)$, using the points (k,i),$(k,i-1)$,$(k-1,i)$,$(k-1,i-1)$ in the discretized computational domain as shown in Figure 1.19.

The solution of the free-wake problem is based on a relaxation scheme, where wake periodicity is enforced as a boundary condition, and the initial condition defines the point along the rotor blade from which the vortex filament originates. These conditions can be stated as

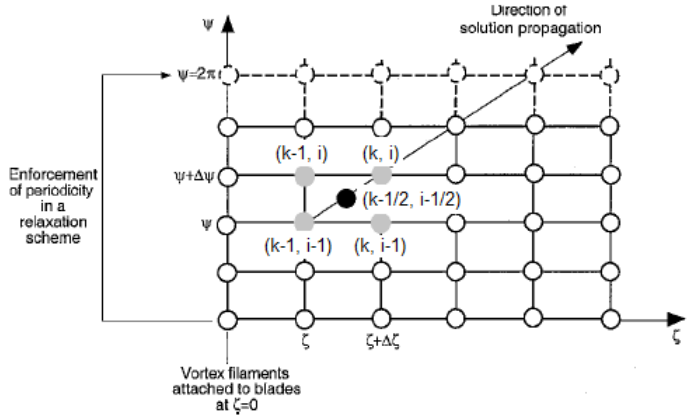

Figure 1.19. Computational domain for free-wake problem [8].

Boundary conditions:

$$\vec{r}(\psi, \zeta) = \vec{r}(\psi + 2\pi, \zeta) \tag{1.25}$$

Initial conditions:

$$\begin{aligned} \vec{r}(\psi, \zeta = 0) &= r_v(\cos\beta\cos\psi\cos\alpha + \sin\beta\sin\alpha)\vec{i} \\ &\quad + r_v(\cos\beta\sin\psi)\vec{j} \\ &\quad + r_v(\sin\beta\cos\alpha - \cos\beta\cos\psi\sin\alpha)\vec{k} \end{aligned} \tag{1.26}$$

An initial prescribed wake geometry is often used, in addition to the above boundary and initial conditions, to begin the free-wake calculations. The solution is stepped in the ζ direction in an iterative manner, and the solution is taken to be converged when the L_2 norm of the positions of the wake collocation points between two successive iterations is within a specified tolerance.

To avoid numerical singularities in the Biot-Savart integration of the induced velocity expression, some form of viscous core model is used. A popular core model used is that proposed by Vatistas et al. [55], where the tangential velocity in the vortex is expressed as

$$v_\theta(h) = \frac{\Gamma h}{2\pi(r_c^{2n} + h^{2n})^{1/n}} \tag{1.27}$$

where n is an integer variable and h is the radial distance from the center of the vortex of circular cross section. The viscous core radius r_c is defined as the radial location where maximum tangential velocity occurs. This location marks the boundary between inner (rotational) flow and the outer (potential) flow. Researchers have suggested that the velocity profile of the rotor tip vortices may closely correspond to $n = 2$ such that

$$v_\theta(h) = \frac{\Gamma h}{2\pi(r_c^4 + h^4)^{1/2}} \tag{1.28}$$

The use of viscous core model serves as a smoothing technique to prevent numerical singularities when computing induced velocities due to the discrete filaments. The initial value of the core radius chosen is based either on experimental observation or by experience.

Time-Stepping Methods

An explicit, time-stepping, free-wake method was first introduced by Landgrebe [6], among others. The wake is modeled using a single tip vortex from each blade, with the filaments discretized into a number of straight line segments of about 15-30 degrees angular step between each. A vortex core radius of about 10% of the blade radius is used to resolve the numerical singularity in the Biot-Savart law. The strength of the tip vortex is determined from the bound circulation on the blade, which is modeled using a lifting-line approach. The wake collocation points on the tip vortices are convected through the flowfield at their local velocity. In order to limit computational time, the wake is divided into two regions: near-field and far-field. Only the near-field collocation points are updated at each time step.

Five turns of the tip vortices are modeled, with the blade unsteady aerodynamic effects being accounted for by using unsteady airfoil data as the shed vortices are neglected in the free-wake model. The solution is assumed to be converged once a periodic wake structure is achieved.

Sadler [56] used an explicit, forward time integration free-wake method to solve for wake geometry in forward flight from an impulsively started rotor. The near-wake is comprised of shed and trailed vortex filaments, while the far-wake is made up of only trailed filaments. The author uses curved vortex elements, as opposed to straight segments, with the implementation of a solid-body-rotation, vortex-core model to improve correlation with the measured data. The author forces the computed induced velocity to a maximum cut-off value, equal to a percentage of the rotor tip-speed, to prevent excessively large velocity perturbations in the flowfield. This was one of the first methods applied to the study of basic multi-rotor systems, including rotors with the non-uniform blade spacing.

Bliss et al. [57] presented a free-wake analysis using curved vortex elements. The curved vortex elements are implemented in a forward-flight, free-wake analysis using a time stepping approach. A far boundary condition wake is attached to the end of each free vortex filament. The main goal of the investigation was to examine the use of curved vortex elements and its advantages over using straight segments. In 1987, Bliss et al. [9] developed a full-span, free-wake model that used curved vortex filaments laid down along the constant vorticity contour lines in the wake, as shown in Figure 1.20. This provides a representation that does not need the modeling of shed and trailed vortices separately. The method is applied only to high speed forward flight since convergence remains an issue at lower advance ratios. The takeaway from this work is that accurate wake modeling is the most important factor in the prediction of higher harmonic airloading. In a study analyzing the rotor aerodynamic loads, Ref. [58] provides further explanation on the use of constant vorticity contour (or CVC) wake model: Although the use of

the full-span CVC wake model is important to the computation of wake motion and wake-induced velocities in the region near the rotor, it is generally computationally expensive to retain this model over the full length of the semi-infinite wake. Thus, a provision has been made for collapsing the full-span CVC wake into a freely distorting root/tip vortex pair for regions suitably far downstream of the rotor. For regions still further downstream, the freely distorting trailers are replaced by a prescribed filament pair...As with all lagrangian wake models using vortex filaments, a vortex core model is required to remove singularities from the flowfield...Since filamentary vortices are still used, some effective core structure must be imposed to remove the flow-field singularities associated with the curved vortices. The CVC wake model has since been incorporated into CHARM (Comprehensive Hierarchical Aeromechanics Rotorcraft Model), a comprehensive code developed by Continuum Dynamics, Inc.

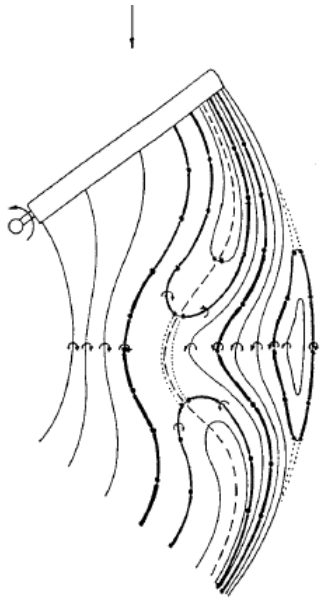

Figure 1.20. Contours of constant vorticity strength in the wake on the advancing side modeled with curved vortex elements [9].

Egolf [59] presented a time-marching, free-wake method, where the wake vorticity is convected at its local velocity, made up of the freestream and the self-induced

velocities. The wake is modeled as a full-span array of vortex box elements with straight sides and constant strengths. A vortex sheet core model is used to remove numerical problems near the discrete vortex segments constituting the vortex box elements - the author calls this a "pseudo" core model. The vortex core radii are sized according to the initial size of the vortex box elements. The method is applied to both a main rotor and a tail rotor operating under blade-vortex interaction conditions. The author states that a larger core radii results in predictions that are smoother. The method is observed to be stable at advance ratios between 0.14 and 0.35, but exhibited instabilities in hover. Later, the same author parallelized the free-wake method to take advantage of advancements in computing capabilities.

Bhagwat and Leishman [60] extended the free-wake methodology developed by Bagai and Leishman [8] to enable transient analysis of rotor wake.

1.2.4 Computational Fluid Dynamics

The physical aspects of any fluid flow phenomenon are governed by three basic principles: 1) mass is conserved; 2) momentum is conserved (Newton's second law); and 3) energy is conserved. These fundamental principles can be expressed in terms of basic mathematical equations, which in their most general form are either integral or partial differential equations. The set of nonlinear, partial differential equations in their most general form are often called the "Navier-Stokes equations". Computational fluid dynamics is a numerical technique of replacing the integrals or the partial derivatives in these equations with discretized algebraic forms, which in turn are solved using digital computers to yield numbers for the flowfield variables at discrete points in space and time. To solve these algebraic equations, the flow domain is discretized so that a computational mesh is generated. This computational mesh comprises a distribution of spatial points called nodes. The flow equations are solved at these discrete nodes, while the flowfield values between these nodes are simply interpolated from the known values at neighboring nodes.

The numerical discretization of the governing equations are performed using either finite difference or finite volume schemes. Furthermore, various approximations can be made to reduce the nonlinearity of the Navier-Stokes equations. For example, the assumption of inviscid flow reduces the Navier-Stokes equations to the Euler equations. Further, assuming the flow to be steady, irrotational and isentropic, one obtains what is called the full-potential equation.

Analysis of the helicopter rotors using Euler methods, discussed in Refs. [61, 62], and Navier-Stokes methods, discussed in Refs. [63–65], began in the late 1980's. However, initially, the rotor inflow was accounted for by using either external wake models or inflow tables. Efforts to capture the rotor wake from first principles without relying on external wake models emerged in the early 1990's, thanks to the enormous improvement in computing capabilities during the 1980's. Some of the initial works were published by Srinivasan et al. [66], Duque et al. [67], Hariharan et al. [68], and Ahmad et al. [69], among others. The tip vortices in most of these analyses are captured up to one revolution, beyond which the vortices diffuse due to numerical dissipation.

Steinhoff [70] came up with a method to alleviate the excessive diffusion of vorticity in the wake by using a "vortex-embedding" approach. He introduces an additional term into the Navier-Stokes equations that acts as an external force to prevent the diffusion of vorticity. The method was applied to incompressible blade-vortex interaction problem [71], and it was concluded that the approach held promise for compressible wake calculations. However, the choice of the additional term for the "vortex-embedding" method directly affects the solution quality.

More recently, Strawn and Djomehri [72] computed the wake of a UH-60A rotor in hover. They found that even with a structured grid with a large number of nodes, the numerical dissipation of the vorticity overwhelms the physical behavior of the system. Duraisamy and Baeder [73] used a high-resolution Reynolds-averaged Navier-Stokes (RANS) solver to study the evolution of tip vortices from rotating

blades. They used higher-order schemes to reduce error from numerical diffusion by means of grid clustering and using overset meshes. A fair agreement was achieved with the experimental swirl velocity measurements up to 300^o of wake age behind the blade. The study concludes that in order to accurately resolve the evolving tip vortex, the use of a refined overset mesh, high-order schemes and a modification to the turbulence model are necessary. Narducci [10] used OVERFLOW (a finite-difference based CFD solver developed by NASA) to calculate the flowfields of the S-76 rotor. The entire solution domain, including the near and the far fields, contain 63.4 million grid points. The grid is clustered to resolve the blade tip vortices and stretches in the region of less importance. An example of the blade and the background grid system is shown in Figure 1.21. The problem is solved on 240 cores of a high performance Linux cluster. A single case took a wall-clock time of approximately 117 hours.

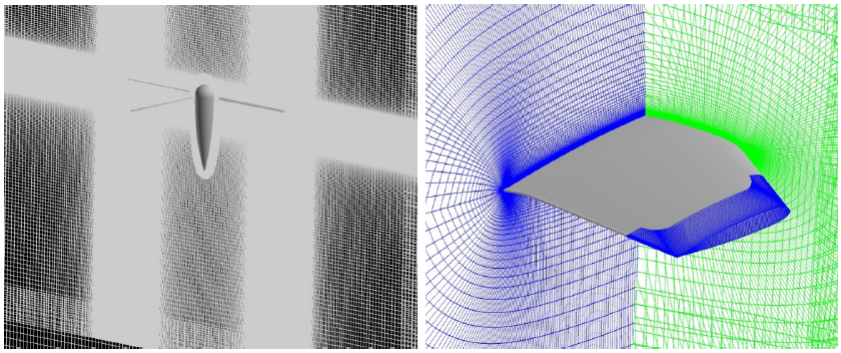

Figure 1.21. Blade and background grid for Boeing OVERFLOW simulation [10].

Overall, CFD methods are not only computationally expensive, but also suffer from numerical limitations in preserving concentrated regions of vorticity. This is why they have not yet made a significant impact on helicopter design, which generally requires much faster solutions because of its iterative nature.

Traditional RANS methods solve for conservative variables $(\rho, \rho u, \rho v, \rho w, \rho e)$ or non-conservative variables (ρ, u, v, w, e). An alternative approach that has shown good promise in long-range wake propagation is a method that is based

on solving, although still in Eulerien grid-based fashion, the RANS equations in vorticity-velocity form

$$\frac{\partial \omega}{\partial t} + \mathbf{u} \cdot \nabla \omega - \omega \cdot \nabla \mathbf{u} = S + \nu \nabla^2 \omega \tag{1.29}$$

In this approach, the primary conserved variable is the vorticity. One such successful approach called the vorticity transport model (VTM) was developed by Brown [74], and Brown and Line [75]. This method basically evolves the vorticity transport equation shown in Eq. (1.29) on a Cartesian grid surrounding the rotor. In the computational implementation, distribution of cells are used in the computational domain to track the vorticity field as it evolves. The method allows computational cells to be created in regions of flow dominated by vorticity and subsequently destroys them when vorticity moves elsewhere. This model is applied to a number of different rotor wake-related problems with good correlations. A wake geometry computed by this method is shown in Figure 1.22.

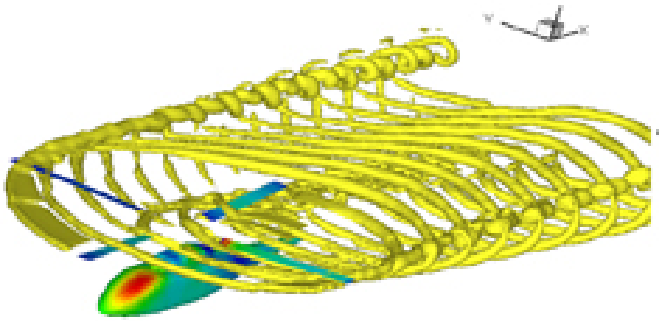

Figure 1.22. Wake geometry in forward flight computed by VTM.

Recently, Advanced Rotorcraft Technology (ART) developed a new approach to wake analysis called the viscous vortex particle method (VVPM). Although the basic concept has been around for a while, it has not been specifically applied to the problem of rotor wake dynamics until recently. The crux of the method involves solving the same vorticity transport equation, discussed earlier, but in a grid-free,

Lagrangian manner [11]. The vorticity field in the wake is represented by a set of Lagrangian vector-valued particles, each of them uniquely defined by their position vectors and the total vorticity contents. For an isolated rotor simulation, the blade is the only source of vorticity. The vorticity generated behind the rotor blade due to the spanwise change in bound vorticity is interpolated and used to generate vortex particles, which are eventually convected through the flowfield in keeping with the vorticity transport governing equation. Figure 1.23 shows a vortex particle simulation for an isolated two-bladed rotor in forward flight.

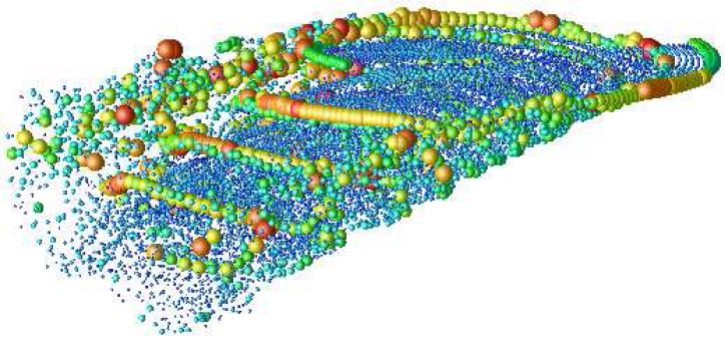

Figure 1.23. Vortex particle vorticity simulation in forward flight for a two-bladed rotor at $\mu = 0.0095$ and $C_T = 0.0032$ [11].

This method has been successfully incorporated in RCAS (Rotorcraft Comprehensive Analysis System), a comprehensive rotorcraft program developed by the US Army AFDD with major support from ART.

At the same time, a new class of methods called "hybrid CFD-Lagrangian methods" have emerged where the blade near-field flow is solved using RANS, while the far-field wake is modeled using potential flow formulations, such as prescribed wake or free-wake models Refs. [76, 77]. Figure 1.24 shows an example of a hybrid methodology developed at the Georgia Institute of Technology. The trailing vortex from the blade is modeled as a piecewise helix of vortex filaments that have the freedom to distort. The influence of these free-wake filaments is modeled as a velocity imparted to the RANS grid boundary. More recent hybrid methods attempt

to combine RANS CFD in the near blade flow with vorticity transport methods in the far field flows.

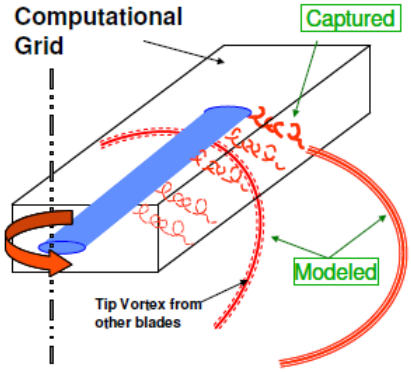

Figure 1.24. Hybrid RANS-freewake methodology [12].

1.3 Motivation of the Current Work

Since CFD methods have not matured to the point where it can be applied to the calculation of the rotor wake within a reasonable time and with reasonable computational resources, free-vortex wake methods are routinely used to model the rotor wake during the design phase of a helicopter. Current predictive free-wake analysis methods make use of discrete vortex filaments, straight or curved, to model the wake. The discrete vortex filaments in the wake present several numerical problems. From the theoretical point of view, there is of course a discretization error associated with modeling a continuous shed vortex sheet with discrete vortex filaments. More importantly, unrealistically large velocities are induced at the core of the filaments due to the singular nature of the vortices. This presents a problem when velocities are computed at control or collocation points that approach very close to the velocity inducing filaments, causing the solution to not only yield unrealistic results but can also cause the solution to "blow up". This behavior is exacerbated with a higher density of wake filaments, longer timesteps for wake

relaxation and wake models that extend far downstream of the blade. Most often, in the free-wake methods currently used by the rotorcraft community, this problem is dealt with by the implementation of vortex core models, which help smooth out velocity spikes in the numerical computations. However, the use of core models violates the theoretical and mathematical formulations of potential flow theory. In addition, the solution is dependent on the choice of core size. Peters [78] sums up the robustness of the current filament-based free-wake models by stating that they rely on many convergence parameters such as vortex-core size, number of radial and azimuthal filaments, and the number of wake turns used before truncation. In addition, he states, the models are fairly unstable at lows speeds and completely unstable in hover.

Also, most of the current free-wake methods often use a single tip filament, representing the tip vortex, to model the rotor wake. The inboard wake is either neglected or a near wake is modeled with a rigid vortex sheet that is merged with the tip filament after a certain wake age. An exception to this is the full-span, constant vorticity contour method. However, one still needs to implement vortex core models for every curved filament used in this model. The disadvantage of not modeling inboard wake or modeling it with rigid wake becomes important when an inboard active device, such as a flap, is present on the blade and its effect on the near wake needs to be taken into account. Since on-blade control using active devices is becoming increasingly attractive for various end goals including aerodynamic performance enhancement, vibration alleviation, and acoustic noise mitigation, the accurate prediction of wake distortion due to any inboard device becomes an important modeling requirement.

The free-wake method discussed in this thesis, being singularity-free and not really requiring any tunable parameters, such as the vortex core size, yields an improvement both computationally and in the accuracy of the results, over current free-wake methods being used for rotor aerodynamic analysis.

With this background, the objectives of this thesis are:

1. To describe the fundamental ideas underlying the new free-wake method.

2. To discuss the development of this method for rotorcraft analysis.

3. To apply the free-wake method to the rotor aerodynamic analysis in both hover and forward flight under various operating conditions and compare the results with experimental data as well as with predictions from other existing analysis methods.

4. To present a preliminary discussion on the capability of the new free-wake method in capturing the effect of on-blade, partial span devices.

5. To suggest ideas for further improvement of the method.

Chapter 2
Numerical Model

In this study, the flowfield is modeled with a potential flow method using distributed sheets of vorticity. The concept of using singularity elements having distributed vorticity is based on the multiple-lifting-line method originally developed by Horstmann [13]. A brief description of this method is presented in the following section.

2.1 Horstmann's Multiple-Lifting-line Model

The method of Horstmann [13] is a fixed-wake, higher-order method based on multiple lifting lines. The lifting surface is defined by the zero-lift lines of the airfoil sections that make up the wing. This surface is divided, spanwise and streamwise, into an array of sub-elements as shown in Figure 2.1, where each of the elements has a bound vortex filament at its quarter chord location, and has quadratic circulation distribution, which results in a trailing vorticity sheet possessing a linear distribution. The fixed wake is shed from each elementary bound vortex directly into the freestream direction so that when multiple lifting lines are used to model the wing, multiple parallel wake sheets emanate from the wing. The collocation or control points are positioned at the midspan of the three quarter chord line of each of the wing sub-elements. In this method, circulation

strength is determined by imposing flow tangency at the collocation points, along with continuity of circulation and vorticity at the edges of neighboring elements. Horstmann derived the exact analytical expressions for the velocity induced by the bound filament with quadratic circulation distribution and the semi-infinite sheet with linearly varying vorticity distribution. The induced velocity at any point is determined by adding the analytical solutions of the velocity induced by all the vortex filaments and the semi-infinite vorticity sheets.

The principal advantage of this higher-order model is that due to the use of a continuous circulation distribution on the lifting lines, greater accuracy is achieved with a significantly fewer elements than would be required by a lifting line method using piecewise constant circulation in the spanwise direction, which trails vortex filaments into the wake or even vortex lattice method that employs horseshoe vortex elements. The need for a relatively fewer elements, along with the use of analytical solutions for the element induced velocities, makes this method numerically efficient.

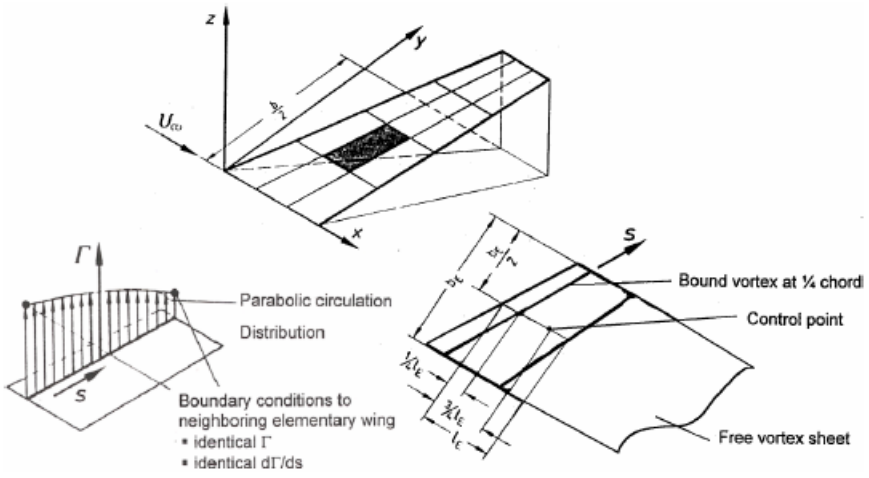

Figure 2.1. Model for Horstmann's multiple lifting-line method [13].

In this section, a background and the basic ideas underlying the free-wake model are discussed.

2.2 Distributed Vorticity Model

Bramesfeld [14] and Bramesfeld and Maughmer [79] developed a higher-order, free-wake method using sheets of distributed vorticity, with the analytical solutions of the induced velocities originally derived by Horstmann, but with the additional capability of modeling wakes that can be relaxed. An elemental model of a distributed vorticity sheet consists of a continuous vortex sheet bounded by two vortex filaments of opposite circulation along its leading and trailing edges. It can be viewed as being constructed by taking two semi-infinite, continuous vortex sheets, with filaments of opposite strengths running along their leading edges, and overlaying one on top of the other with a certain chord wise separation between the two filaments. Since the vortex sheets aft of the filaments are of equal magnitude but of opposite strengths, they cancel one another. A schematic of the construction of such an elemental sheet of distributed vorticity is shown in Figure 2.2.

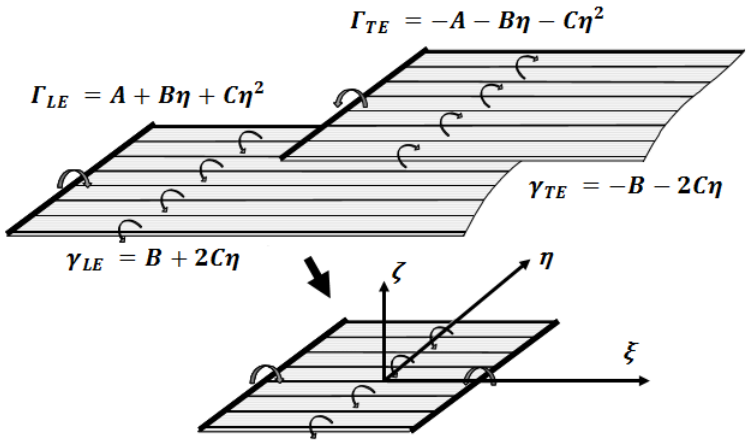

Figure 2.2. Construction of an elemental sheet of distributed vorticity [14].

A filament with quadratic circulation distribution results in trailing vortex sheets with linear vorticity distribution in accordance with Helmholtz's vortex theorem. The bound circulation strength along the filament, Γ, and vorticity sheet strength, γ, are specified as functions of the spanwise coordinate, η, with constant

coefficients A, B and C as

$$\begin{aligned} \Gamma_{LE} &= A + B\eta + C\eta^2 \qquad \gamma_{LE} = B + 2C\eta \\ \Gamma_{TE} &= A + B\eta + C\eta^2 \qquad \gamma_{TE} = B + 2C\eta \end{aligned} \tag{2.1}$$

The positive subscripts indicate the fore system and the negative subscripts indicate the aft system of filament-sheet combination with equal and opposite strengths. The vorticity of the sheet is aligned with the local flow direction (along the ξ axis). The sheet lies in the ξ-η plane, and thus the ζ-axis is normal to the plane of the vorticity element.

2.2.1 Induced Velocity

In discussing the derivation of the velocities induced by such a distributed vorticity element, a local coordinate system attached to the element needs to be specified. A distributed vorticity element has a trapezoidal shape in general, with its left and right edges parallel to each other. The local element-fixed reference frame is defined by the Cartesian axes ξ, η and ζ as shown in Figure 2.3. The ξ-axis points downstream along the chord of the element, η-axis points outward along the element span, and ζ-axis is normal to the element. As it is depicted in Figure 2.3, ζ-axis points out of the page. $\vec{x_o}$, the origin of the ξ- η - ζ system, is the control point of the element.

The η-coordinate along the right side edge of the element is η_i, and the η-coordinate along the left edge is $-\eta_i$, where the subscript i is the index of the element being considered in an array of such elements constituting a blade. The span of the element, defined as the perpendicular distance between the side edges, is $2\eta_i$. The ξ-coordinates of the midspan points of the element's leading and trailing edges are $-\xi_i$ and ξ_i respectively so that the midchord is $2\xi_i$. Since the leading and trailing edges are not constrained to be parallel in general, the chord of the element varies along its span. The "sweep" of a line in the plane of the element is defined

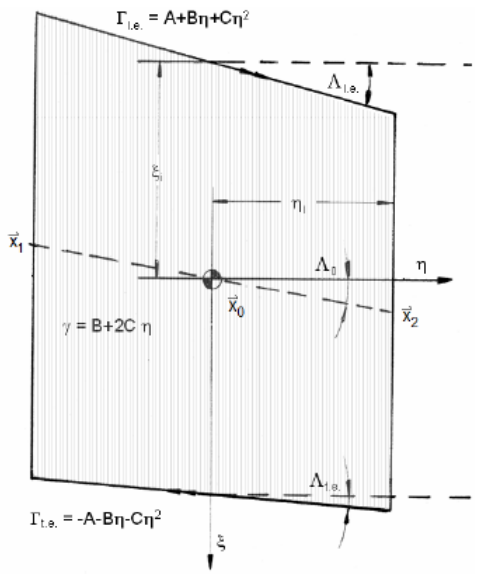

Figure 2.3. Element-fixed coordinate system of the distributed vorticity element [13].

as the angle it makes with the η-axis. Positive sweep corresponds to a positive increase in the ξ-coordinate of the line for a given increment in the η-coordinate. The element leading edge sweep, Λ_{LE}, midchord sweep, Λ_o, and trailing edge sweep, Λ_{TE} are related to each other geometrically as

$$\tan \Lambda_o = \frac{1}{2}(\tan \Lambda_{LE} + \tan \Lambda_{TE}) \tag{2.2}$$

The chord of the element, c_i can be expressed as a function of the element's η-coordinate as

$$c_i(\eta) = 2\xi_i + \eta(\tan \Lambda_{TE} - \tan \Lambda_{LE}) \tag{2.3}$$

The left and right side midchord points, indicated as $\vec{x_1}$ and $\vec{x_2}$ in Figure 2.3, have the local coordinates

$$\vec{x_1} = \begin{Bmatrix} -\eta_i \tan\Lambda_o \\ -\eta_i \\ 0 \end{Bmatrix} \quad \vec{x_2} = \begin{Bmatrix} \eta_i \tan\Lambda_o \\ \eta_i \\ 0 \end{Bmatrix} \tag{2.4}$$

The velocity induced by the distributed vorticity element with a known strength at an arbitrary point in an incompressible flow can be derived using the Biot-Savart law. According to this law, a section of a vortex filament with a differential vector length $d\vec{s_1}$ and circulation Γ located at $\vec{r_1}^*$ induces on point P_A located at $\vec{r_A}$ the differential velocity given by

$$d\vec{w_1} = \frac{\Gamma}{4\pi} \frac{d\vec{s_1} \times (\vec{r_A} - \vec{r_1}^*)}{|\vec{r_A} - \vec{r_1}^*|} \tag{2.5}$$

A section of the vortex sheet with differential vector length $d\vec{s_2}$, width $d\eta$, and circulation strength of $\gamma d\eta$ located at $\vec{r_2}^*$ induces at point P_A a differential velocity given by

$$d\vec{w_2} = \frac{\gamma d\eta}{4\pi} \frac{d\vec{s_2} \times (\vec{r_A} - \vec{r_2}^*)}{|\vec{r_A} - \vec{r_2}^*|} \tag{2.6}$$

To derive the expressions for the induced velocity due to a vortex filament and its shed vorticity, a locally attached reference frame similar to that shown in Figure 2.3, but with the origin at the center of the vortex filament, is used. The geometrical parameters for the derivation are shown in Figures 2.4 and 2.5. The vectors from $d\vec{s_1}$ and $d\vec{s_2}$ to P_A, and their magnitudes can be expressed as

$$\vec{r_1} = \vec{r_A} - \vec{r_1}^*; \quad \vec{r_2} = \vec{r_A} - \vec{r_2}^*; \quad \vec{r_1} = |\vec{r_1}|\,; \quad \vec{r_2} = |\vec{r_2}| \tag{2.7}$$

The expressions for the remaining parameters in terms of the geometrical parameters shown in Figure 2.4 and 2.5 are

$$\vec{r_A} = \begin{Bmatrix} \xi_A \\ \eta_A \\ \zeta_A \end{Bmatrix}; \quad \vec{r_1}^* = \begin{Bmatrix} \eta \tan\Lambda \\ \eta \\ 0 \end{Bmatrix}; \quad \vec{r_2}^* = \begin{Bmatrix} \xi \\ \eta \\ 0 \end{Bmatrix}; \quad \vec{ds_1} = \begin{Bmatrix} d\eta \tan\Lambda \\ \eta \\ 0 \end{Bmatrix}; \quad \vec{ds_2} = \begin{Bmatrix} -d\xi \\ 0 \\ 0 \end{Bmatrix} \tag{2.8}$$

In order to be consistent with the positive direction of the wake vorticity, the sign of $d\vec{s_2}$ is the opposite of the direction shown in Figure 2.5.

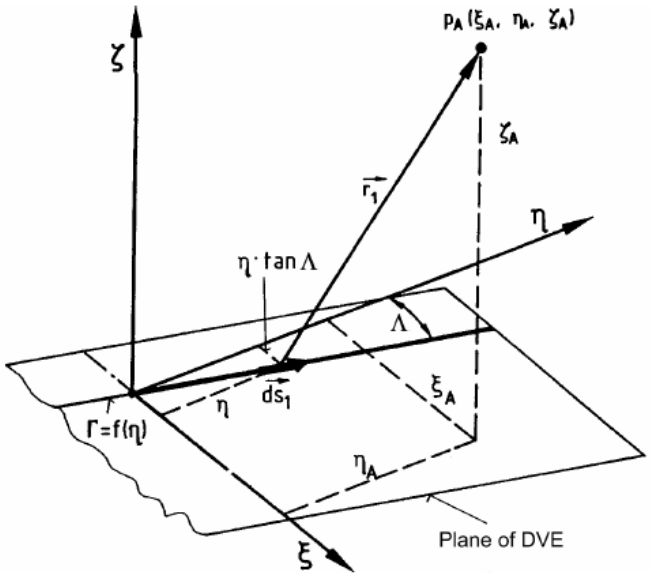

Figure 2.4. Geometry for the derivation of vortex filament induced velocity [13].

The velocity induced by the entire length of the vortex filament is evaluated by integrating Eq. (2.4) from $-\eta_i$ to η_i, with the substitutions from Eqs. (2.11) and (2.8), to obtain

$$\vec{w_1}(\xi_o, \eta_o, \zeta_o) = \int_{-\eta_i}^{\eta_i} \frac{A + B\eta + C\eta^2}{4\pi r_1^2} \begin{Bmatrix} -\zeta_o \\ \zeta_o \tan\Lambda \\ \xi_o - \eta_o \tan\Lambda \end{Bmatrix} d\eta \tag{2.9}$$

The velocity induced by the semi-infinite vortex sheet can be obtained by first integrating Eq. (2.5) in the ξ -direction from 0 to ∞, and then in the spanwise

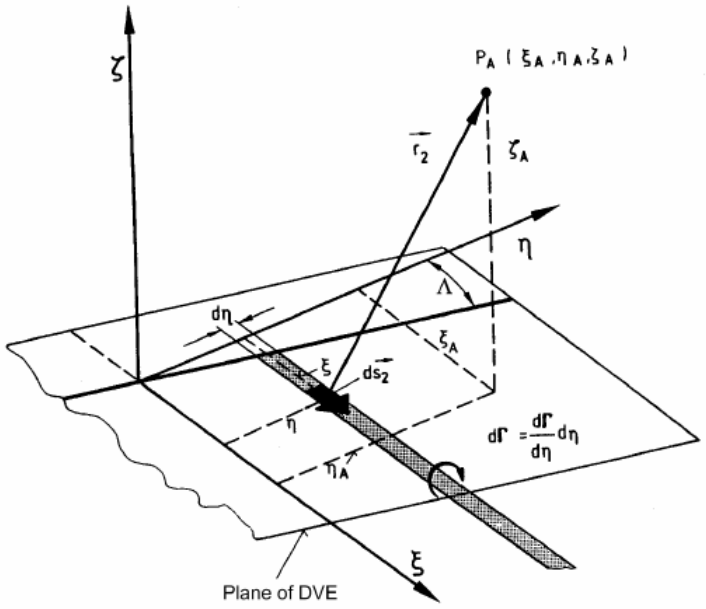

Figure 2.5. Geometry for the derivation of vortex sheet induced velocity [13].

direction from $-\eta_i$ to η_i as

$$\vec{w_2}(\xi_o, \eta_o, \zeta_o) = \int_{-\eta_i}^{\eta_i} \frac{B + 2\eta C}{4\pi((\eta_o - \eta)^2 + \zeta_o^2)} \left(\frac{\xi_o - \eta \tan\Lambda}{r_1} - 1 \right) \begin{Bmatrix} 0 \\ -\zeta_o \\ \eta_o - \eta \end{Bmatrix} d\eta \quad (2.10)$$

where $r_i = \sqrt{(\xi_o - \eta \tan\Lambda)^2 + (\eta_o - \eta)^2 + \zeta_o^2}$. It should be observed that the vortex sheet does not induce any velocity in the ξ-direction, as this is the direction of the sheet's vorticity. The expressions in Eqs. (2.9) and (2.10) are identical to the expressions found in Ref. [13], except that their signs are opposite because Ref. [13] uses a left-hand vortex rotation convention while right hand convention has been used in this work. Eqs. (2.9) and (2.10) can be integrated analytically as explained in Ref. [13] and the results can be found in Ref. [15].

The total velocity induced by the distributed vorticity element at point P_A is obtained by adding the velocities induced by the individual components of the

element, which consists of the leading and trailing edge vortex filaments and their corresponding semi-infinite vortex sheets

$$\vec{w} = \vec{w}_{1LE} + \vec{w}_{2LE} + \vec{w}_{1TE} + \vec{w}_{2TE} \tag{2.11}$$

The total induced velocity at an arbitrary point P_A is evaluated by adding the velocity contributions from all the distributed vorticity elements used to model the wing or blade surfaces and the wake.

2.2.2 Treatment of the Singularities

The tangentially induced velocity approaches infinity as one moves towards the core of a vortex filament, which is generally not an issue in this analysis. While directly on a straight filament, the Biot-Savart integration is improper and the integral admits a Cauchy principal value of zero that is used in the numerical implementation. Hence, no special handling is needed when induced forces are computed along the filament using the Kutta-Joukowski theorem. There may be velocity spikes near the juncture of two non-aligned straight segments, but these can be dealt with by taking quadrature points for the induced force integrations sufficiently inboard. If needed, local geometry smoothing may be implemented as well.

As one approaches the planer vortex sheet away from its edges, the induced velocity remains finite, with a discontinuity in tangential velocity across the sheet. On the sheet itself, a finite Cauchy principal value of Biot-Savart integration defines the induced velocity. However, at the side edges of the sheet, or at a point on the swept leading edge, the sheet's induced velocities can attain infinite values as a logarithmic singularity exists there. Hence a special treatment is necessary for numerical implementation of the method.

A continuous spanwise vorticity distribution is shown in Figure 2.6 for a vortex

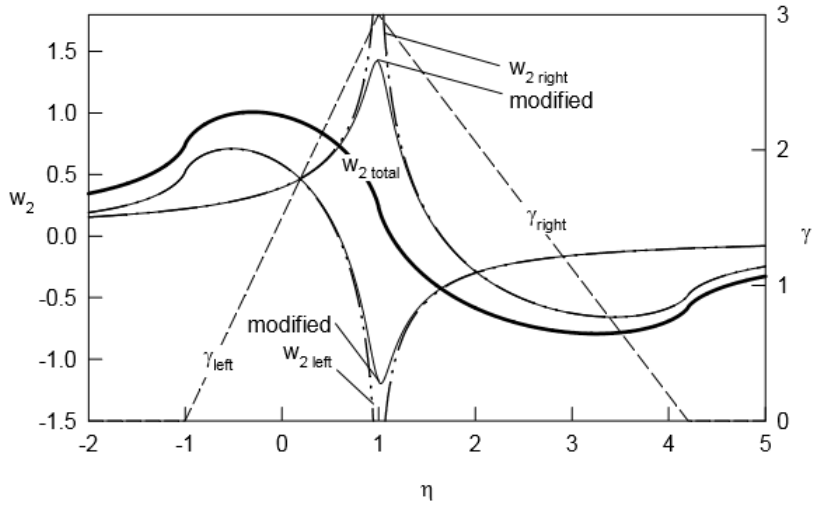

Figure 2.6. Spanwise distribution of normal velocity induced in the plane of two semi-infinite vortex sheets. The left sheet spans from $\eta = -1$ to 1 and the right sheet spans from $\eta = 1$ to 4.2. Spanwise vorticity distribution is denoted by the dashed lines and the total induced velocity is denoted by the solid line [14].

sheet having a triangular circulation distribution which goes to zero at $\eta = -1$ and 4.2. The resulting induced normal velocity w_{2total} is finite in the plane of the sheet and shown by the heavy lines in the figure. When this sheet is discretized with two separate sheets having linear vorticity distributions γ_{left} and γ_{right}, the overall induced velocity should remain unchanged. The individual velocity contributions of each discrete vortex-sheet element, w_{2left} and w_{2right}, depend partly on logarithmic terms of the form

$$w_2(\eta) \sim \ln \left[\frac{(\eta - \eta_i)^2}{(\eta + \eta_i)^2} \right] \tag{2.12}$$

where, again, η is the local span coordinate of the point at which the induced velocity is being calculated, and η_i is the half span of the semi-infinite sheet element. The numerator of the logarithmic expression of one of the vortex-sheet elements becomes zero as the common boundary of the two neighboring elements is approached at $\eta = 1$. At the same time, the denominator of the other element approaches zero at the same rate. Now, if the vorticity at the common edge are of equal strengths, the

resulting singularities in w_{2left} and w_{2right} are of the same magnitude but opposite sign and, hence, cancel one another. As a result, the total induced velocity w_{2total} remains finite and unchanged from the original case of the vortex sheet with the continuous triangular vorticity distribution.

For numerical implementation, however, the logarithmic term in Eq. (2.12) requires special treatment. Bramesfeld [14] introduces additional singularities to the side edges of each individual vortex-sheet element that cancels the original singularities and each element becomes numerically well-behaved, as indicated by the modified induced velocity distribution in Figure 2.6. The combined induced velocity remains unaffected as the added singularities of the two neighboring elements cancel one another. The additional singularities to each side edge of the vortex sheet element is done by adding a positive constant k to both the numerator and denominator of the logarithmic term of Eq. (2.12), such that

$$w_2(\eta) \sim \ln\left[\frac{k+(\eta-\eta_i)^2}{k+(\eta+\eta_i)^2}\right] \tag{2.13}$$

With this numerical treatment, the combined velocity w_{2total} will remain unchanged if the same constant k is used for two neighboring vortex sheet elements.

At the extreme edges of the wake sheet where there is no neighboring element, such as at the blade tip and root, introducing such a canceling singularity has a potential to change the solution. The velocity induced at the wake edge will depend on the magnitude of the added singularity, which will in turn affect the shape of the relaxed wake. Ref. [14] uses 1% of the span of the smallest surface vorticity element as an appropriate value of k, which ensured that the velocities at the edges remained small enough so that the solution does not blow up, but not so small that the wake edge roll-up behavior is overly restricted. While this results in a well-behaved wake relaxation, it makes the solution dependent on the magnitude of the singularity k, which is the only real modeling parameter necessary in this free-wake method. Another approach, suggested by Basom [15] and Basom

and Maughmer [80], uses points for relaxation purposes slightly inboard from the extreme edge of the wake rather than points at the very edge of the wake. At these inboard points the velocity remains finite without requiring the introduction of the constant k described earlier. Although this eliminates the need for the constant k, it introduces a dependency on the inboard distance, which has to be chosen wisely. For example, if the point is too far inboard, the direction of the induced velocity reverses. To make sure this does not occur, at each timestep the velocity reversal points are determined on each side of the wake at the midchord of the wake row immediately behind the blade surface. The edge displacement points are then set inboard by a certain fraction of the distance to the velocity reversal points. For the wake rows further aft, which have stretched in the course of the relaxation, the velocity reversal points tend to move farther inboard as a fraction of the edge element, so that using the same span ratio as for the most upstream row keeps all the edge relaxation points on the proper side of the velocity reversal points. This approach results in a smooth relaxation and is found to be better then the k approach.

Another problem related to the side edge singularity is the inexact canceling that occurs between two non-coplanar neighboring elements. This is quite a common occurrence in the free-wake analysis because the highly non-planer physical wake is represented/modeled by a number of planer elements. This problem is demonstrated by referring to Figure 2.7. The left schematic shows the edge view of two coplanar distributed vorticity elements, dve1 and dve2, viewed along the general ξ-axis of the local element coordinate system. The velocities induced by the dve1 and dve2 are denoted by $\vec{w_1}$ and $\vec{w_2}$ respectively, with their net resultant vector denoted by $\vec{w_R}$. The induced velocities $\vec{w_1}$ and $\vec{w_2}$ are computed using the singularity canceling term k discussed earlier, so that they remain numerically finite. However, their individual magnitudes are relatively large. The velocities induced by the two elements are in the opposite directions, resulting in a resultant vector that is much smaller than

either of the two components. The right schematic in Figure 2.7 shows the two elements when they are not co-planar and meeting at an angle of ν. The induced velocities $\vec{w_1}$ and $\vec{w_2}$ are no longer in opposing directions but meet at the angle ν. This causes the resultant velocity to become larger as the magnitude of the angle ν gets smaller. The increase in $\vec{w_R}$ can be substantial if the magnitudes of $\vec{w_1}$ and $\vec{w_2}$ are large enough. This is a result of the planar elements meeting at a sharp corner and should be considered an error.

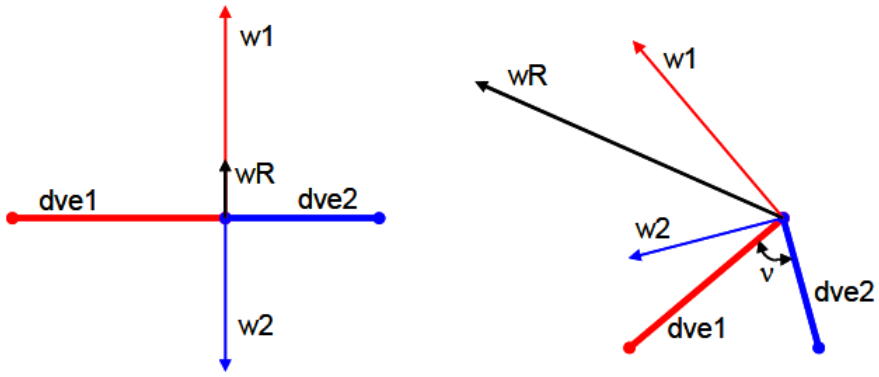

Figure 2.7. False velocity spike at the juncture of non-coplanar neighboring elements (right) compared to the velocity cancellation of coplanar elements (left). $\vec{w_1}$ and $\vec{w_2}$ are velocities induced by dve1 and dve2 respectively at the shared junction, and $\vec{w_R}$ is their resultant. [15]

In a tightly rolled-up tip region, the angle between the elements can exceed forty-five degrees unless the wake is very finely paneled. The technique of introducing the singularity term k as discussed earlier helps make the induced velocity well-behaved, but there are still cases when the velocity peaks can adversely affect the wake relaxation. Basom [15] came up with a technique to improve this situation. He temporarily split each of the elements adjacent to the common edge into two new elements when computing their influence on the induced velocity at the junction.These new elements are given a small span and made coplanar, while the elements exterior to these constitute much of the original spans and remain close to the orientations of the original two elements. This facilitates the cancellation of the

side-edge singularities and also removes the wake gap at the junction. Figure 2.8 shows the procedure just explained, where the configuration on the left is replaced by the one on the right when computing their influence on the induced velocity at their shared junction.

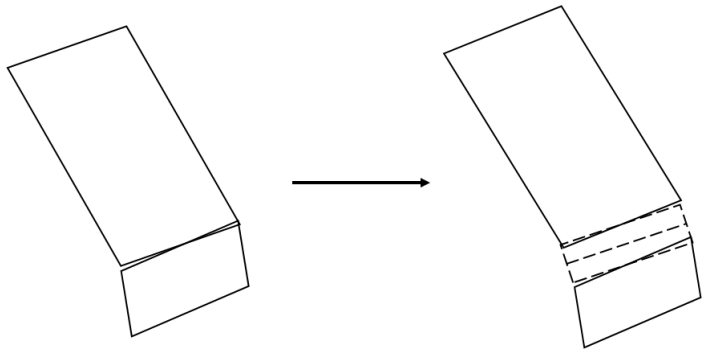

Figure 2.8. Schematic of the element splitting for the computation of the induced velocity at the junction of two non-coplanar wake elements.

The vorticity coefficients of the new elements are set to maintain continuity of vortex filament and sheet strength between elements, while ensuring that the circulation around each old element is equal to the sum of that around its two replacements, even though there is a slight net increase in span. Figure 2.9 shows the relaxed wakes calculated with and without the element splitting technique for a single wind turbine blade operating at tip speed ratio of 6. The wake in the tip region gets jumbled if the splitting technique is not implemented.

For more detailed exposition on the basic model, one is referred to the Refs. [13, 14].

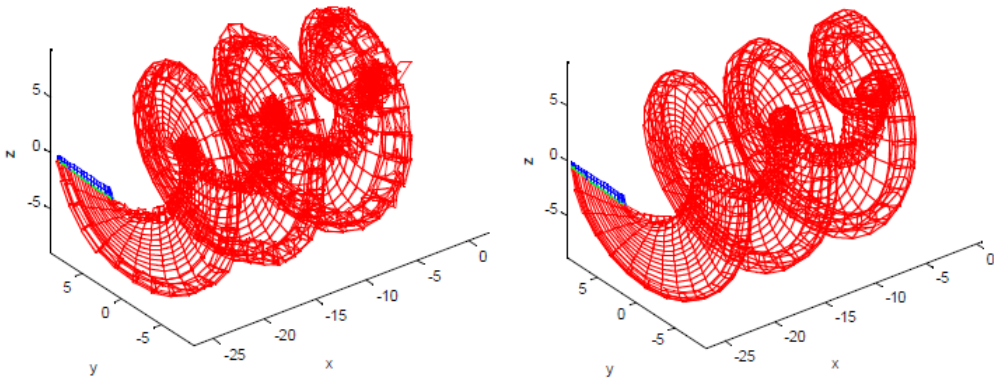

Figure 2.9. Free wake without(left) and with (right) the element splitting method. [15]

2.3 Blade Modeling

The blade is modeled with an array of m chordwise and n spanwise distributed vorticity elements, introduced in section 2.2. The paneling is done in such a way that leading edge of the foremost row of surface elements is located a distance $\frac{c}{4m}$ aft of the leading edge of the blade, while the trailing edge of the aft most row extends the same distance aft of the blade trailing edge, where c is the blade chord. In general, the surface elements are connected in the spanwise direction at their midchords and in the chordwise direction at their midspans, though a slightly different arrangement is used when computing the surface induced velocity on the lifting lines for force computation. An example of a blade paneling with $m = 2$ and $n = 18$ is shown in figure 2.10, while figure 2.11 shows a 3-bladed rotor modeled with elements of distributed vorticity. The blue lines represent the edges of the vorticity elements and the broken red line represents the trailing edge of the actual blade surface.

For a detailed description of the blade modeling used in the free-wake method, one is referred to the Refs. [15] and [16].

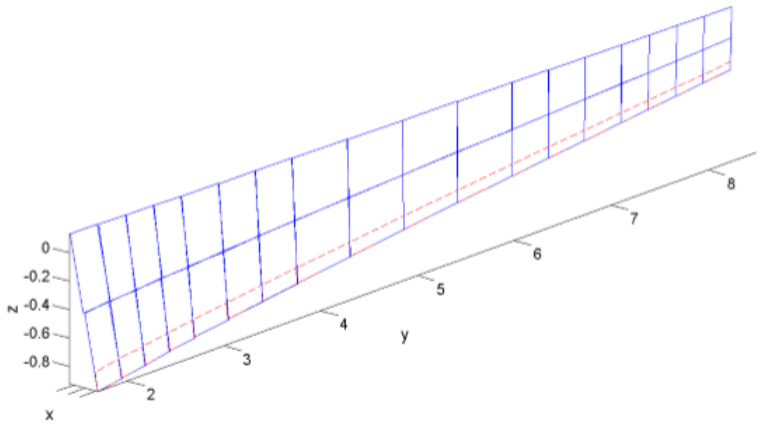

Figure 2.10. Blade surface paneling with distributed vorticity elements. [15]

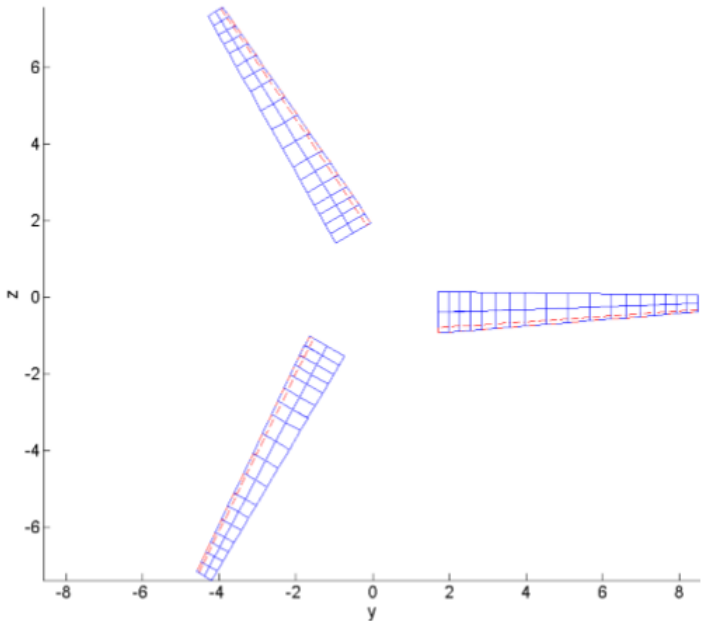

Figure 2.11. Blade paneling of a 3-bladed rotor with distributed vorticity elements. [15]

2.4 Wake Relaxation

Several options for the wake model and its evolution were developed for wind-turbine application by Basom [15] and Basom and Maughmer [80], such as a fixed wake, a fully-relaxed wake, and a 'semi-relaxed' wake. However, since this work is focused on the development of a 'free-wake' method for rotorcraft application, only

a fully-relaxed wake is discussed. A time-stepping or a time-marching methodology is used for wake relaxation. In this methodology, as the blade rotates each time step, a spanwise row of wake elements is generated which represents the vorticity shed by the blade during that particular time step. Each row of the wake contains one element of distributed vorticity for each spanwise element located at the trailing edge of the blade. These wake elements are connected spanwise at their midchord and streamwise at their midspan. During each time step, induced velocities are computed at the side edge midpoints of each wake element. These velocities are then used to compute the displacement for each of the wake points based on the time step size. As these points are displaced, the wake system is reconfigured or re-paneled to represent the new side-edge midpoints. During this process, each element continues to be planar and its side edges remain parallel. These elements can, can however, stretch and deform.

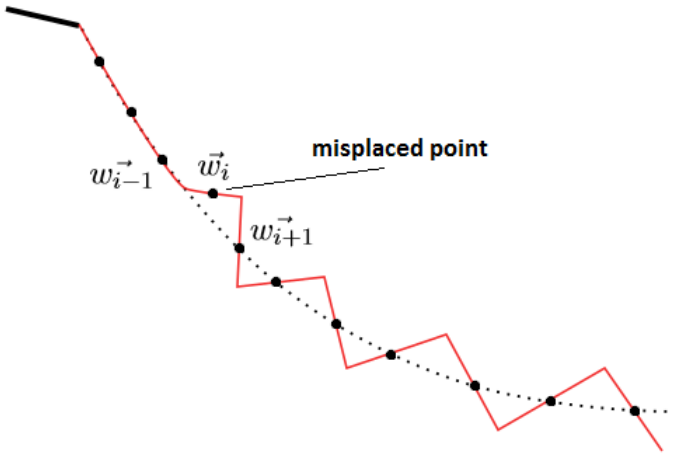

Figure 2.12. Crinkling of wake on re-paneling as a result of a single misplaced relaxation point.

Basom [15] discusses a problem in which, if one of the displacements of a relaxation point is slightly off, this can lead to a 'crinkling' of the re-paneled wake downstream of this point. This scenario is shown in Figure 2.12, where the blade cross section is shown at the left and the trajectory of the force-free wake shed from

the blade as a dotted line. The discretized representation of the wake is shown as solid line segments with the dots as the midchord relaxation points. To avoid this situation, a velocity smoothing technique was implemented by Basom based on the work by Bramesfeld [14]. The technique involves using an averaged induced velocity at the 'outlier' relaxation point. If $\vec{w_i}$, $\vec{w_{i-1}}$, and $\vec{w_{i+1}}$ are the induced velocities at the point and at its upstream and downstream neighbors, the smoothed velocity at the 'outlier' point is obtained as

$$\vec{w_{i_{smoothed}}} = \frac{\vec{w_{i+1}} + 2\vec{w_i} + \vec{w_{i-1}}}{4} \tag{2.14}$$

If a point in the wake is shed from the blade at time t_o, position $\vec{x_o}$, and is moving with induced velocity $\vec{w(t)}$, its position at some later time t, in general, is given by

$$\vec{x(t)} = \vec{x_o} + \int_{t_o}^{t} \vec{w(\tau)} d\tau \tag{2.15}$$

As in standard relaxation schemes, the induced velocity $\vec{w(t)}$ in Eq. (2.15) is the induced velocity that is computed at the point during each time step. The relaxation point is displaced each time step using the displacement

$$\Delta\vec{x} = \vec{x(t_{i+1})} - \vec{x_i} = \int_{t_i}^{t_{i+1}} \vec{w(\tau)} d\tau \tag{2.16}$$

where t_i and t_{i+1} are consecutive time steps. Basom [15] developed an alternative scheme called 'steady relaxation technique', which is applicable only for a steady loading case. In this technique, the velocity history of the point is replaced by the current values of the induced velocities computed at upstream points. The steady relaxation method can speed up the convergence time of a solution, but it does not apply to unsteady wake cases. The implications of using the steady relaxation vs standard relaxation technique are explained in the Ref. [15].

The wake relaxation process is computationally expensive. Consider that there

are B blades and N spanwise wake elements per wake row for each blade. Since induced velocities need to be computed at the side-edge mid-points of each wake element, the number of floating point operations required for N_t time steps turns out to be $50B^2(N^2+N)(2{N_t}^3+3{N_t}^2+N_t)$. In order to reduce the computational time, for a geometrically symmetric rotor an assumption can be made that the wakes generated from the blades are also symmetric. This necessitates the computation of induced velocities on the wake shed from only one blade using the symmetry condition. This numerical artifice reduces the number of operations to $50B(N^2+N)(2{N_t}^3+3{N_t}^2+N_t)$, a reduction by a factor of B.

Further techniques to reduce the cost of the relaxation process were developed by Basom [15] for his wind turbine code. The first technique involves the use of variable time step size which allows the time step size in the early part of the simulation to be large and, as the simulation progresses, the time step size can be decreased. The idea behind this technique is that large time step size can be used initially to convect the wake downstream. This helps save some computational expense since the computational time is proportional to the third power of the total number of wake rows. Nevertheless, sufficient paneling density can be maintained near the rotor towards the end of the simulation. The second method to speed up the simulation is to allow the wake to be extrapolated once it reaches some user-specified distance downstream of the rotor. Both these speed-up techniques, originally developed for the wind-turbine code, are retained for application in this work.

During the relaxation, the wake elements can stretch in the spanwise direction. While doing so, the circulation content of the element must be conserved in accordance with the relation

$$\frac{1}{2\eta_i}\int_{-\eta_i}^{\eta_i}\Gamma d\eta = A_i + \frac{1}{3}C{\eta_i}^2 = K \tag{2.17}$$

In the numerical formulation, this condition is used along with the continuity of

circulation and vorticity between the spanwise wake elements.

2.5 Equation System Solution

The blade or the lifting surface is represented by an array of distributed vorticity elements. The circulation strength of the array is determined by solving a system of linear equations obtained by applying boundary conditions between the elements and by imposing the kinematic flow condition (flow tangency) at the control points of the elements. The kinematic flow condition requires that the component of the sum of the freestream and the induced velocities that is normal to the control point of the element be zero.

Each of the the distributed vorticity element has a piecewise quadratic circulation distribution, whose strength is defined by three coefficients: A, B, and C as described in section 2.2. If N is the number of such elements representing the blade, the number of unknown parameters that completely defines the blade circulation distribution is $3N$. One, therefore, requires $3N$ equations to solve this system, which is accomplished by applying boundary conditions and kinematic flow conditions as described below.

Boundary conditions require that the circulation strengths, Γ, as well as the derivatives of the circulation, $\frac{d\Gamma}{dy}$, are continuous between the elements. For N number of elements, there are $N-1$ interior edges at which two adjacent elements are connected.

The continuity of circulation between an element i and its spanwise neighbor $i+1$ can be expressed as

$$A_i + B_i\eta_i + C_i{\eta_i}^2 = A_{i+1} - B_{i+1}\eta_{i+1} + C_{i+1}{\eta_{i+1}}^2 \tag{2.18}$$

And the continuity of slope of circulation or vorticity between an element i and its spanwise neighbor $i+1$ can be written as

$$B_i + 2C_i\eta_i = B_{i+1} - 2C_{i+1}\eta_{i+1} \tag{2.19}$$

Applying Eqs. (2.18) and (2.19) to all the interior junctions of the distributed vorticity element array yields $2(N-1)$ equations.

At the blade root and the tip, a zero circulation boundary condition is used such that

$$A_{root} - B_{root}\eta_{root} + C_{root}{\eta_{root}}^2 = 0 \tag{2.20}$$

$$A_{tip} + B_{tip}\eta_{tip} + C_{tip}{\eta_{tip}}^2 = 0 \tag{2.21}$$

Eqs (2.20) and (2.21) provide two more equations, resulting in a total of $2N$ equations so far. Still, N conditions are required before the problem can be solved. The remaining N equations are obtained by applying kinematic flow conditions.

The kinematic flow condition stipulates that the component of the flow normal to the control point of the surface distributed vorticity element must be zero, such that

$$(\vec{V_{Kin}} + \vec{w})_i \cdot \vec{n_i} = 0 \tag{2.22}$$

where the subscript i denotes the surface element at which the condition is being imposed, $\vec{n_i}$ is the local surface normal vector, $\vec{V_{Kin}}$ is the kinematic velocity vector composed of both the incoming wind and the rotational velocity, and $\vec{w}$ is the total induced velocity at the control point due to the influence of all the blades and the associated wake.

The induced velocity vector $\vec{w}$ can be decomposed into contributions from the surface elements, $\vec{w}_{surface}$ and contributions from the wake elements, $\vec{w}_{wake}$. With this decomposition, Eq. (2.22) can be rewritten as

$$(\vec{V_{Kin}} + \vec{w}_{surface} + \vec{w}_{wake})_i \cdot \vec{n}_i = 0 \tag{2.23}$$

The induced velocity due to the surface elements can be written as

$$(\vec{w}_{surface} \cdot \vec{n})_i = \sum_{j=1}^{N} (a_{ij} A_j + b_{ij} B_j + c_{ij} C_j) \tag{2.24}$$

Here, the coefficients a_{ij}, b_{ij}, and c_{ij} provide the influence of surface element j onto the control point of the surface element i. A_j, B_j, and C_j are the circulation coefficients of the surface element j.

The induced velocity due to the wake elements can be written as

$$(\vec{w}_{wake} \cdot \vec{n})_i = \sum_{j=1}^{N} \left\{ B_j \sum_{k=1}^{N_w} \left[b_{ijk} \left(\frac{B_{jk}}{B_j} \right) \right] + C_j \sum_{k=1}^{N_w} \left[c_{ijk} \left(\frac{C_{jk}}{C_j} \right) \right] \right\} \tag{2.25}$$

where j is the spanwise index along the blade trailing edge, and k is the streamwise index along the wake element rows. The coefficients b_{ijk} and c_{ijk} provide the influence of the wake element at the spanwise position j and the streamwise position k onto the control point of the surface element with index i. B_{ijk} and C_{ijk} are the vorticity coefficients of the wake element. The expression in Eq. (2.25) assumes that there are no spanwise vortex filaments in the wake, which is true in steady case. In the unsteady case, the spanwise filaments represent the shed vorticity. In the steady case, the vorticity coefficients of a wake element jk are related to the coefficients of the corresponding trailing edge surface element with index j, in accordance with the Helmholtz's circulation conservation theorem. But since the wake element may have a different span than the corresponding surface element, the coefficients are not exactly the same numerically. A good approximation for the change in the coefficients, assuming even stretching, can be obtained using

$$\frac{B_{jk}}{B_j} \approx \frac{\eta_j}{\eta_{jk}}; \qquad \frac{C_{jk}}{C_j} \approx \left(\frac{\eta_j}{\eta_{jk}}\right)^2 \tag{2.26}$$

where η_j and η_{jk} are the half-spans of the elements j and jk.

In a steady-flow case, the wake induced velocity can be retained on the left hand side along with the surface self-induced velocity while the incoming wind velocity is a known quantity at every time step and can be moved to the right hand side of Eq. (2.23) such that

$$(\vec{w}_{surface} + \vec{w}_{wake})_i \cdot \vec{n_i} = -(\vec{V_{Kin}})_i \cdot \vec{n_i} \tag{2.27}$$

In an unsteady case, the induced velocity contribution of the wake is taken from the previous time step, which makes this part a known quantity at every time step. Hence, along with the incoming wind velocity, the wake-induced velocity contribution is moved to the right hand side of Eq. (2.23) giving

$$(\vec{w}_{surface})_i \cdot \vec{n_i} = -(\vec{V}_{Kin} + \vec{w}_{wake})_i \cdot \vec{n_i} \tag{2.28}$$

Writing Eq. (2.27) or (2.28) for all of the control points of the elements on the blade yields the remaining N equations. The system of $3N$ equations is organized in a matrix form as

$$\Big[D\Big]\{A\} = \{R\} \tag{2.29}$$

The unknown surface circulation coefficients (A_i, B_i, and C_i) are represented by the vector $\{A\}$. The influence coefficients resulting from application of boundary and kinematic flow conditions are assembled in the matrix $\Big[D\Big]$ having a size of $3N \times 3N$. The vector {R} contains the known quantities at each time step.

In the time-stepping methodology, if the steady assumption is used, the left

hand side of Eq. (2.29) is updated at each time step to include the wake-induced velocity influence. If the unsteady option is used, the left hand side of Eq. (2.29) only contains the surface self-induced velocity influence along with the boundary conditions, which remains fixed for a given problem. The right hand side is updated at each time step to include the influence of the wake.

Chapter 3
Implementation of the Free-Wake Method

In this chapter the implementation of the free-wake method for both hover and forward flight are described. The description of the methodology for forward flight will also cover the need for a trim routine, and hence the coupling of the free-wake method with RCAS, a comprehensive helicopter program.

3.1 Free-Wake Methodology in Hover

The hover analysis presented in this thesis was performed using a modified wind turbine code that was originally developed by Basom [15], and Basom and Maughmer [80], and later extended by Maniaci [16], and Maniaci and Maughmer [81] to include profile drag and a stall model. The following sections describe the key aspects of the modified code.

3.1.1 Coordinate System

The free-wake analysis in hover uses a global stationary coordinate system x, y, and z, with x-axis aligned with the rotor shaft and pointing away from the earth's surface. The direction of rotation is counter-clockwise as viewed from the top.

When a vertical wind velocity with a direction shown in Figure 3.1 is imposed to simulate axial climb, the rotor system moves up along the positive x-direction. In a hovering flight, as the wind velocity is zero, the rotor system stays fixed with respect to the global stationary frame. This frame is equivalent to a frame centered and fixed with respect to the hub.

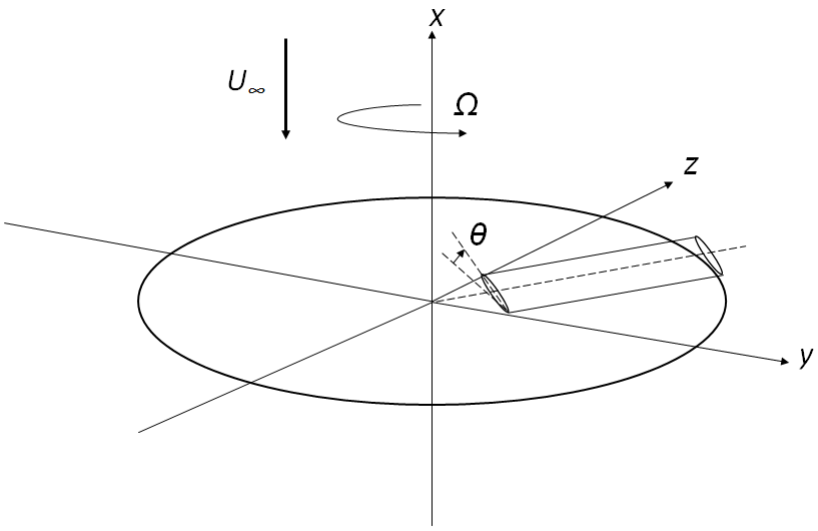

Figure 3.1. Coordinate system for hover analysis.

3.1.2 Profile Forces and Stall Effects

The basic methodology used to compute the section profile forces (lift and drag) based on airfoil tables is unchanged from that implemented by Maniaci [16] for wind turbine analysis. When configuring the wind-turbine program for helicopter hover analysis it was recognized that the wind hits the lower or the pressure side of the wind turbine blade, with the blade pitched into the wind. The blade section aerodynamic angles used in the wind turbine code are shown in Figure 3.2. The airfoil has a positive camber which, in the wind-turbine code, has a negative value of $\alpha_{\varnothing L}$ or airfoil zero lift angle of attack. In the potential flow model used in this work, the distributed vorticity elements are placed along the zero lift line of the

airfoil whose angle with respect to the rotor plane is represented by Θ_{ZLL} (positive as shown). The blade twist with respect to the chordline of the airfoil is given by

$$\Theta = \Theta_{ZLL} + \alpha_{\varnothing L} \tag{3.1}$$

The resultant velocity $\vec{V}_{rel}$ is that part of the total velocity that is in the plane parallel to the blade section. If $\vec{V}_{total}$ can be written as

$$\vec{V}_{total} = \vec{V}_{Kin} + \vec{w}_{ind} \tag{3.2}$$

where $\vec{V}_{Kin} = \vec{U}_{\infty} + \Omega r$ and $\vec{w}_{ind}$ is the induced velocity at that section, then

$$\vec{V}_{rel} = \vec{V}_{total} \cdot \hat{e}_{chord} + \vec{V}_{total} \cdot \hat{e}_{normal} \tag{3.3}$$

where $\hat{e}_{chord}$ and $\hat{e}_{normal}$ are unit vectors tangential and normal to the blade section respectively. If there is no local spanwise flow, the total and relative velocities are equivalent.

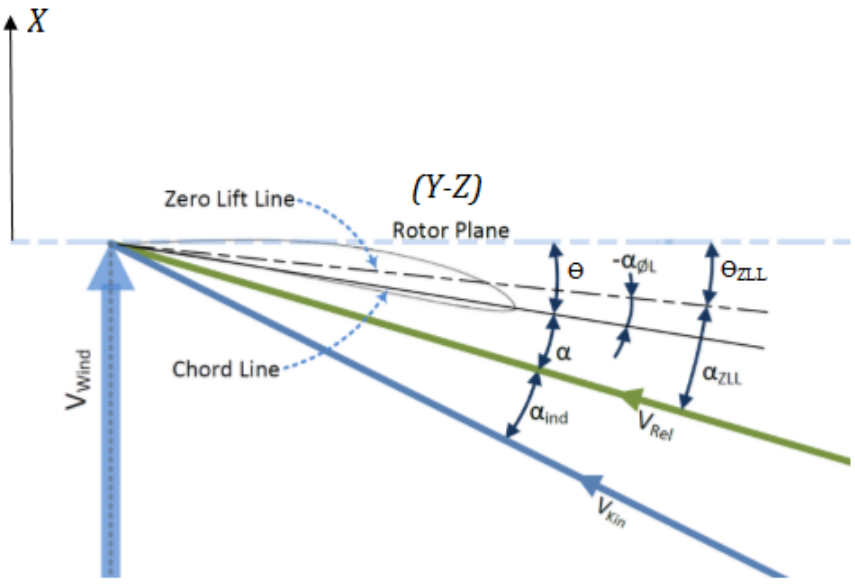

Figure 3.2. Blade section angles used in the wind turbine code. [16]

When modeling a hovering helicopter rotor, the following points must be noted:

1. The wind velocity U_∞ or V_{Wind} is zero. For an axial climb, however, this velocity vector is pointing downward, that is, in the negative X-direction. When there is a finite wind velocity, the rotor is moved or translated in the positive X-direction, against the wind.

2. In the hover analysis, when a positive local blade twist is specified, the blade section must be pitched up with its leading edge above the rotor plane. This change could be easily implemented in the wind turbine program by changing the sign of the blade twist distribution. Also, a positive collective pitch, θ_o, in hover can be achieved by changing the sign of the collective pitch in the wind-turbine program, where a positive collective pitch uniformly increments both Θ and Θ_{ZLL}, resulting in a further pitch-down orientation with respect to the rotor plane.

3. In the wind-turbine program, the angle between zero-lift line and the chordline, $\alpha_{\varnothing L}$, has a negative value for a positively cambered airfoil as shown in Figure 3.2. This convention will still be used for a hovering rotor case so that the effective angle of attack calculation, which will be discussed later, will have the correct sign.

The code has been modified such that the operating conditions, and rotor and blade geometrical properties can be entered in the input file as it would be done for a helicopter rotor. The various aerodynamic angles relevant to the blade section used in the helicopter hover analysis are shown in Figure 3.3.

The profile forces on the blade section are computed with respect to the relative velocity, $\vec{V}_{rel}$, described earlier where the profile drag is along the relative velocity vector and the profile lift is normal to it. The airfoil section profile lift and drag coefficients are found from the airfoil profile data tables based on the angle of attack. The determination of the profile force coefficients of an airfoil is important

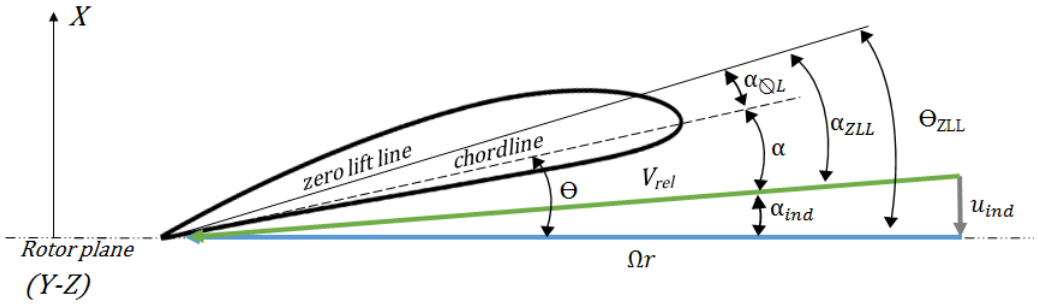

Figure 3.3. Blade section angles used in hover analysis.

for cases where the blade section is stalled, or when the lift-curve slope of an airfoil is not exactly the thin-airfoil result of 2π. In Ref. [16], two methods for computing local angle of attack are discussed. The first method computes the local angle of attack based on the lift coefficient solved from the application of Kutta-Joukowsky law using the bound circulation that is obtained from the equation system solution ($c_{l_{Pot}}$), while the second method calculates the angle of attack directly from the flowfield velocities. The work discussed in Ref. [16] adopts the first method based on comparison with experimental results of the sectional normal force coefficient of the NREL UAE Phase VI wind turbine. This method is similar to that adopted in other free-wake codes.

The method computes an effective angle of attack based on the local spanwise force distribution. First, the potential resultant force is computed using the equation system solution of the surface circulation distribution with the kinematic flow condition discussed in section 2.5. The lift coefficient $c_{l_{Pot}}$ is computed from the potential resultant force as

$$c_{l_{Pot}} = \frac{\frac{\|\vec{F}_{Res\_Pot}\|}{\rho}}{\frac{1}{2}\|\vec{V}_{rel}\|^2 S_{Ref}} \tag{3.4}$$

where $\vec{F}_{Res\_Pot}$ is the integrated force on a spanwise panel, S_{Ref} is the area of the blade panel, and $c_{l_{Pot}}$ is the average lift coefficient of the panel. An effective angle of attack, which will be represented by $\alpha_{ZLL-Pot}$, is calculated using the lift coefficient

found from Eq. (3.4). Remembering that this angle of attack is referenced to the zero-lift line and, by using the thin airfoil theory lift-curve slope of 2π, allows us to write

$$\alpha_{ZLL\_Pot} = \frac{c_{l_{Pot}}}{2\pi} \tag{3.5}$$

The angle of attack in the airfoil tables, which will be represented by α_{cl_Pot}, are typically referenced to the chordline which can be computed by using the zero-lift angle of attack $\alpha_{\varnothing L}$ and the relationship

$$\alpha_{cl\_Pot} = \alpha_{ZLL\_Pot} + \alpha_{\varnothing L} \tag{3.6}$$

The zero-lift angle of attack is taken as negative for a positively cambered airfoil. Using α_{cl_Pot} along with the local Reynolds number (R_e), one can retrieve the airfoil lift and drag coefficients from the tables as

$$\begin{aligned} c_{l\_profile} &= \text{Table Look-up}(\alpha_{cl\_Pot}, R_e) \\ c_{d\_profile} &= \text{Table Look-up}(\alpha_{cl\_Pot}, R_e) \end{aligned} \tag{3.7}$$

The process of obtaining this angle of attack is shown in Figure 3.4, where α_{cl_Pot} lift curve, represented by the broken red line, is shifted to the left by the zero-lift angle.

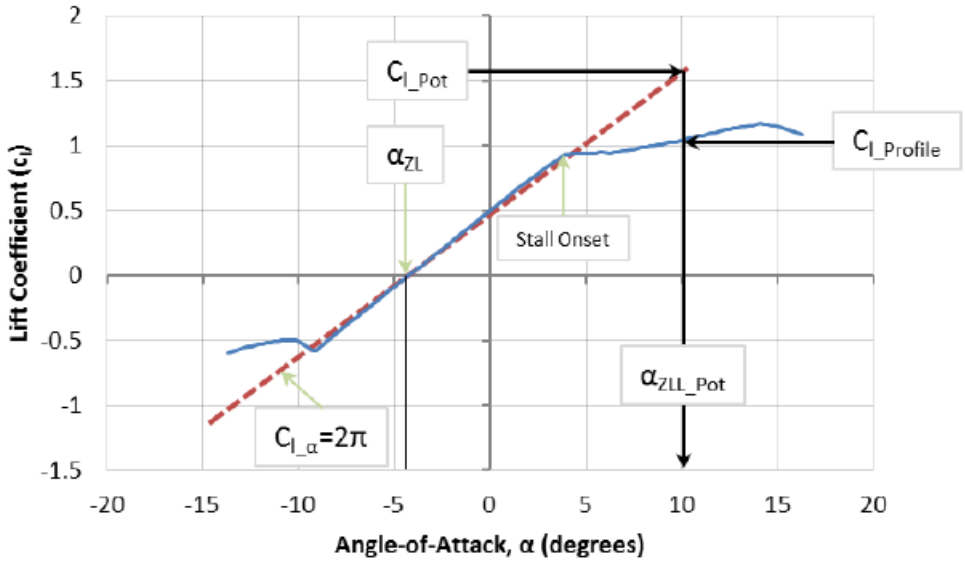

Figure 3.4. Method of computing angle of attack from the lift coefficient predicted with the potential flow solution. [16]

3.1.3 Downward Wake Convection

When the rotor is in hovering flight, the wind velocity is zero and, hence, the only velocity that convects the wake vorticity downward is the induced velocity field. However, since the current method is based on a time-stepping scheme and the calculation starts without the presence of an initial wake vortex helix that would serve as a sort of "far-wake condition," the induced velocity field at the beginning is very weak. This results in the wake vortex sheets piling up close to and under the rotor. In addition, due to the low velocity around the rotor hub, the wake sheets there tend to move up. As more layers of wake sheets are generated, the inboard edges of the blade-root wake elements are further stretched, exacerbating the situation and resulting in an unrealistic-looking wake configuration near the center of the rotor. Ref. [82] explains that the impulsive rotation method of free-wake calculation causes nonphysical strong instability of the initial wake and suggests starting the rotor at a low speed and then gradually increasing the speed

up to the operating speed of the rotor. This technique did not work in the current method, the reason for which is worth investigating. Alternatively, a finite wake convection velocity was applied for the initial few revolutions in all the analysis cases presented in this work. A provision was made which allowed the magnitude of this artificial convection velocity to gradually decrease linearly or according to a function with respect to simulation time step.

3.2 Free-Wake Methodology in Forward Flight

Free-wake methodology in forward flight is more complicated than that for the fairly simple case of a hovering flight. For a rotor in hover, or more generally, in axial flight, the kinematic velocity field around the rotor is axisymmetric. From the point of view of numerical implementation, this allows for a simplification such that the influence of any number of blades can be obtained by using the solution of one modeled blade along with its associated wake using symmetry/image techniques.

In contrast, the dynamics and aerodynamics of a rotor in forward flight presents a number of complexities. First of all, the velocity distribution around the rotor is non-uniform. This is a result of the vector addition of the rotational velocity and the uni-directional relative wind velocity the rotor experiences as it moves edgewise. For instance, the rotational velocity adds up with the oncoming relative wind velocity at the tip of the advancing blade, while the relative wind velocity gets subtracted from the rotational velocity at the retreating blade tip. This is illustrated by the schematic in Figure 3.5. Performing such vector additions at points throughout the rotor disk results in a highly non-uniform velocity field. It also results in a region of reverse flow at high relative flight speeds.

The non-uniform velocity distribution results in a non-uniform aerodynamics or airloads distribution around the rotor. Due to the asymmetry of lift on the advancing and retreating sides, and taking into account the 90^o force-displacement

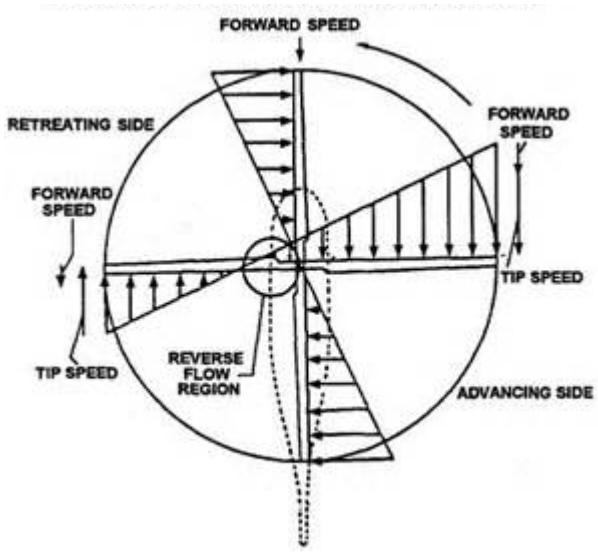

Figure 3.5. Velocity distribution in forward flight. Schematic:www.marinegouge.com

lag, the rotor blades will have a tendency to flap up as they approach the front of the rotor and flap down as they approach the rear. In addition to the natural tendency of the disk to tilt back, the rotor also has a tendency to tilt laterally to the right, or starboard, side. This effect is caused by the coning of the rotor disk, which is an outcome of the balance of aerodynamic and centrifugal forces about the blade "flapping hinge". Coning causes an increase in blade angle of attack at the front of the rotor and a decrease at the rear, which leads to the disk tilting to the right, as viewed from the back of the rotor.

Clearly, if no action is taken, unwanted moments on the rotor disk will structurally and dynamically render the helicopter unflyable. In order to redistribute the asymmetric lift on the rotor disk and to achieve a means of controlling the direction, magnitude, and the line of action of the thrust vector, a blade feathering mechanism is used whereby the pitch angle of the blades is changed, either collectively or cyclically. On conventional helicopters, this is commonly accomplished via the use of a swashplate mechanism.

Unlike the simple blade motions used in wind turbine and hovering rotor applications, the free-wake methodology in forward flight requires the blades to

have both feathering and flapping degrees of freedom. Moreover, due to the non-uniform aerodynamic environment across the rotor, a simple symmetry condition, such as that used in the wind turbine and hovering rotor codes, to include the influence of more than one blades cannot be used. And finally, a validation of the wake model with experimental or flight test data requires the rotor to be "trimmed" which fixes the control settings that satisfy the vehicle equilibrium equations. Modifications to the inviscid wind turbine program developed by Basom [15] to introduce the aforementioned capabilities are discussed in the following sections.

3.2.1 Coordinate System

The free-wake program uses a hub-fixed, non-rotating coordinate system that is represented by a right-handed Cartesian coordinate axes x, y, and z. The x-axis is directed along the rotor's axis of rotation, with positive direction pointing up. The y-axis is directed along the relative wind velocity, with positive direction pointing to the rear of the rotor. The z-axis points to the right or starboard side of the rotor. The $y-z$-plane is perpendicular to the rotor shaft. The blades rotate in the anticlockwise sense. In contrast to the wind-turbine code of Basom, the rotor remains fixed with respect to the ground and the wakes generated from the blades are convected downstream by the relative wind, which basically makes this set-up similar to a rotor being tested in a wind tunnel. This change was made due to the advantage of being able to process some of the output data with more ease. Figure 3.6 shows the coordinate system used in the modified, forward-flight, free-wake program.

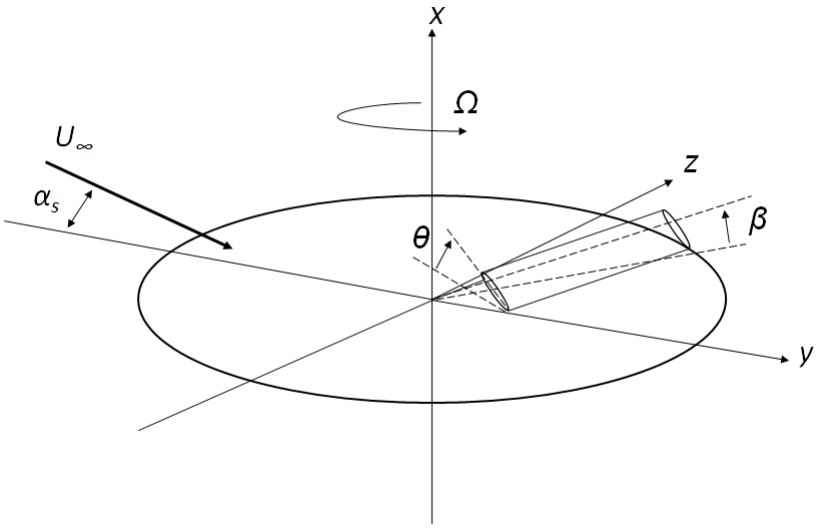

Figure 3.6. Rotor hub-fixed coordinate system.

3.2.2 Blade Motion

As described earlier, the blades of a rotor in forward flight not only flap but also feather continuously as they rotate. Mathematically, the blade flapping angle is represented as an infinite Fourier series

$$\beta(\psi) = \beta_o + \beta_{1c}\cos\psi + \beta_{1s}\sin\psi + \beta_{2c}\cos 2\psi + \beta_{2s}\sin 2\psi + ... \qquad (3.8)$$

where $\beta(\psi)$ is the flapping angle at azimuthal location ψ, and is measured with respect to the rotating coordinate system with its origin at the rotor hub. The coefficient β_o represents the mean blade flapping or coning angle; β_{1c}, called the longitudinal flapping coefficient, represents the longitudinal tilt of the disk (positive when tilted forward); and β_{1s}, called the lateral flapping coefficient, represents the lateral disk tilt (positive when tilted to the right). The coefficients β_{2c}, β_{2s}, and so on, represent the higher harmonics of blade motion, which manifest as a slight warping or wobbling of the rotor tip path plane. For trim and performance analysis it is considered an acceptable practice to omit all the harmonics above the first [2].

In the free-wake code, only the first harmonics of blade motion are considered.

The flapping motion can be introduced by specifying the coefficients β_o, β_{1s}, and β_{1c} via an input file. For simplicity, the blade hinge is assumed to be at the center of the rotor.

The blade pitch motion can also be described using a Fourier series as

$$\theta(\psi) = \theta_o + \theta_{1c}\cos\psi + \theta_{1s}\sin\psi \tag{3.9}$$

where $\theta(\psi)$ is the blade pitch at azimuth ψ, measured with respect to the hub plane (or the plane perpendicular to the rotor shaft). θ_o is called the collective pitch and controls the average blade pitch angle and, hence, the blade lift and average total thrust of the rotor. θ_{1s} is called the longitudinal cyclic and θ_{1c} is called the lateral cyclic, and they control the orientation of the rotor disk and, hence, the direction of the total thrust vector. Because the blade pitch is manually changed by the pilot to control the forces and moments on the rotor, is it also referred to as pilot input or control input. The control input is supplied to the free-wake program via an input file by specifying the constants θ_o, θ_{1c}, and θ_{1s}.

3.2.3 Accounting for Multiple Blades

Multiple blades can be simulated in the free-wake program by using an algorithm similar to what RCAS refers to as "single blade analysis". When this option is used in RCAS, instead of analyzing all the blades, a single blade is analyzed and its results mapped onto other blades [22]. Using this technique, however, is predicated on the following assumptions:

1. All the blades are geometrically identical.

2. The aerodynamic environment, such as the velocity distribution, is periodic around the rotor.

3. The blade motion, including feathering, flapping and lead-lag, is also periodic

in the azimuthal direction.

These assumptions restrict the technique to the analysis of rotors in steady trimmed flight. Nonetheless, the advantage of this method is that, instead of computing the blade and wake geometries associated with all the blades of the rotor, the solution is obtained for only one of the blades and its wake which reduces the computation time by the order of the number of blades.

In the framework of the free-wake program, this method of accounting for multiple blades is called "multiple blade phasing." In this technique, the geometrical model for a single blade rather than all the blades in the rotor system is specified in the input file. The calculation is performed for the single blade and the effects of the remaining blades are included by using the history of the modeled blade from the corresponding azimuthal locations. To illustrate this idea, consider the schematic in Figure 3.7 for simulating a 2-bladed rotor with 8 time steps per revolution.

In accordance with the time-stepping methodology used in this work, the blade starts off at time step $t = 0$, which corresponds to the azimuthal position $\psi = 0^o$. A variable associated with this blade at this time step can be saved using an array `blade1_var` with the corresponding time step as an index. This variable can represent, for example, one of the coefficients of the circulation strength of an element of distributed vorticity at a particular spanwise location or that of one of the wake elements generated by this blade. If it is assumed that, `blade1_var[0] = a`, and at time step $t = 2$ this variable has the value `blade1_var[2] = b`. When the blade reaches $t = 6$, the effect of the "second" blade and its associated wake, which is not solved seperately, can be included in the global solution by using the variable of the first blade when it was at $t = 2$. This is to say that the variable associated with second blade at the current time step has the same numerical value as that associated with the first blade at time step $t = 2$, i.e., `blade2_var[6] = blade1_var[2] = b`.

For an 2-bladed rotor, the correct index of the variable associated with the first blade that is used to simulate the second blade is given as

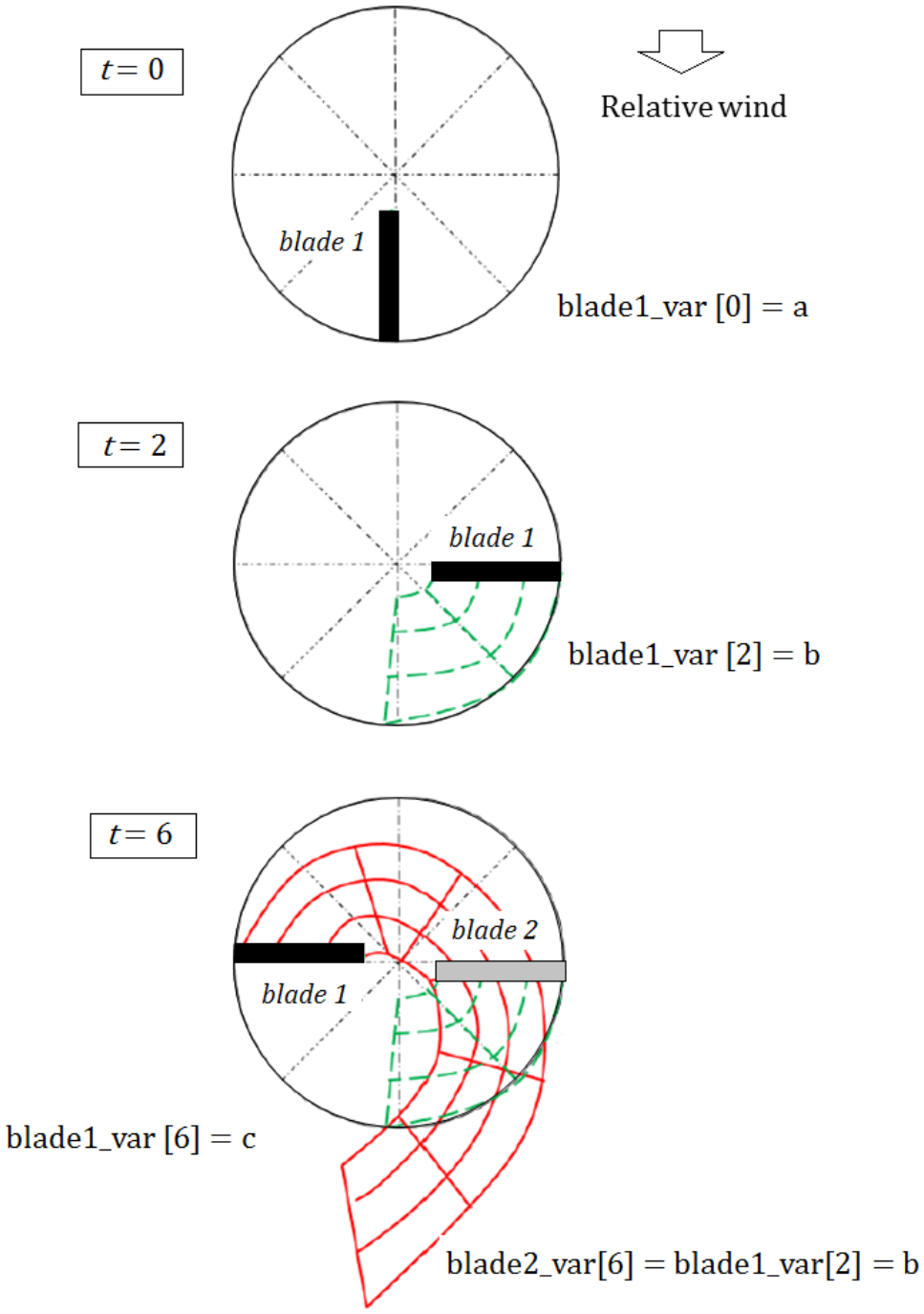

Figure 3.7. Illustration of a method to account for multiple blades.

$$\tau = t - \frac{M}{2} \tag{3.10}$$

where t is the current time step and M is the number of time steps in a revolution.

Generalizing this for a P-bladed rotor, the "phased" index for the nth blade can be written as

$$\tau_n = \tau_{n-1} - \frac{M}{P}, \quad 2 \leq n \leq P \tag{3.11}$$

where the blade number, denoted by the subscript n, is counted backwards from the current blade which is considered as the first blade (with $n = 1$). It must be noted that $\tau_1 = t$.

Having explained the idea behind multiple blade phasing, it should be noted that the effect of "all" the remaining blades cannot be "pulled out" from the history of the current blade until the current (or the first blade) has completed a certain number of time steps which is related to the number of blades the rotor system has. A 2-bladed rotor, for example, needs to complete $\frac{M}{2}$ time steps (half a revolution) before data for the second blade are available. A 4-bladed rotor needs to complete M time steps (a full revolution) before data for all the remaining blades are available. In the program, the time step after which "multiple blade phasing" is to be turned on can be specified in the input file as an integral value representing the number of revolutions.

Solution convergence will initially suffer but, given a sufficient number of revolutions, the starting mismatch or asymmetry in the induced velocity field will die out as the initial wake vortex sheets get convected far downstream of the rotor. Convergence in this program is determined based on the L_2-norm of the induced velocity field around the rotor. As it will be seen later in the thesis, this norm decreases quite rapidly.

3.2.4 Convergence Criterion

The forward-flight free-wake program is coupled with RCAS where the coupling methodology involves RCAS calling free-wake for induced velocity after every coupling iteration. Since the airloads are provided by RCAS at every coupling iteration, a stopping criterion must be used in the free-wake part of the coupled solution. For this work, the induced downwash velocity at the blade sections is taken as the variable for the imposition of stopping criterion. L_2 norm of the difference between the induced downwash velocities at two consecutive revolutions at all the velocity computational points is calculated at the end of each revolution by

$$\|\Delta v\|^n = \frac{1}{MN}\sqrt{\sum_{\psi:i=1}^{M}\sum_{r:j=1}^{N}(v_{i,j}^n - v_{i,j}^{n-1})^2} \tag{3.12}$$

where M is the number of azimuthal steps in a revolution and N the number of spanwise velocity computation points. When this quantity falls below a constant such that

$$\|\Delta v\|^n \ < \epsilon \tag{3.13}$$

where ϵ is specified by the user, and is less than 1, the simulation stops and writes the final induced velocities into a file to be used by RCAS in the next coupling iteration.

3.2.5 Free-Wake-RCAS Coupling

Comparison of numerical predictions with experimental or test data requires the rotor to be trimmed. To achieve this, the higher-order, free-wake method is coupled with RCAS, a comprehensive helicopter analysis code, to take advantage of its robust trim algorithm. A brief introduction to trim procedure used in RCAS is

given in Appendix B. The details of the coupling will be presented in the following sections.

3.2.5.1 Coupling Methodology

RCAS has a functionality that allows an external wake program to interface with it. Selecting the "external vortex wake" option under the "inflow" screen in RCAS activates this functionality. The interaction between RCAS and wake program is based on what is called a "loose-coupling methodology," in which data is exchanged between the two modules at every coupling iteration until a convergence of some sort is reached. The data that RCAS sends to the external wake module are the blade motion and bound circulation for one revolution, while the data that the wake module sends to RCAS is the converged inflow distribution for one rotor revolution. A flowchart of the coupling procedure is shown in Figure 3.8.

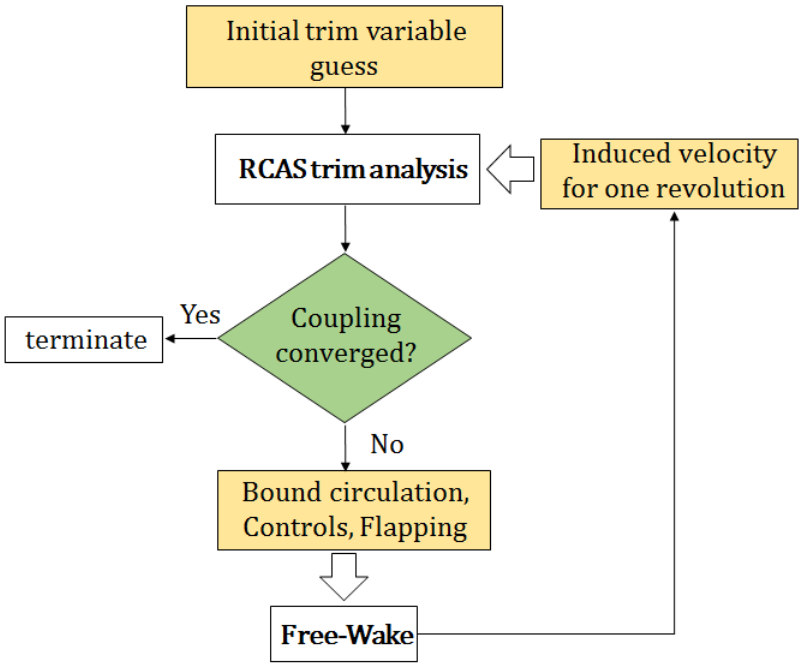

Figure 3.8. Flow diagram of RCAS-free-wake coupling solution.

For extracting blade motion and the airloads data from RCAS and sending wake

induced inflow to RCAS during the solution process, a special C library called SDX is provided by ART that uses the UNIX semaphore and *mmap* shared memory primitives to enable a "lock-step" style synchronization and data communication between interacting UNIX/LINUX processes. SDX channel serves as the exchange medium between the producer and consumer. On one end of the channel, it blocks processes from writing until the channel becomes empty, at which point a producer calling `sdxput()` function is allowed to update the data and signal that the channel is currently full. At the other end of the channel, any (waiting) consumer calling the `sdxget()` function is also blocked and must wait until the channel is full, upon which one consumer is allowed to read the data, and signal that the channel is empty. In this way, these two processes complete one cycle of data exchange and are ready for the next cycle.

The coupling framework used in this work involves three components that interact with one another through a combination of SDX library functions and input/output file system. The three components are RCAS, the free-wake module and an intermediary program. This programmatic structure was adopted to keep both RCAS and the free-wake program modular in implementation. The function of the intermediary program, which is written in FORTRAN, is to facilitate interaction between RCAS and the free-wake module. This program uses the function `sdxget()` to extract blade motion and bound circulation data from RCAS at the end of each trim iteration and writes them into a file to be used by the free-wake program. When RCAS completes a trim iteration and the relevant data has been extracted, RCAS waits for induced velocity from the wake module. The intermediary program then signals the wake program to proceed using the input data that was previously written to a file based on the output from RCAS. The wake module then writes the converged inflow distribution to a file which is read by the intermediary program and sent to RCAS using the `sdxput()` function. This cycle will proceed until the relative induced velocity difference between successive coupling iterations falls

below a user-specified tolerance.

A sample of RCAS-free-wake coupling script and the contents of the intermediary program are given in Appendix C.

3.2.5.2 Circulation Matching Procedure

Johnson provides quite a detailed explanation of separating the general free-wake analysis into an "inner" and an "outer" problem in his text *Rotorcraft Aeromechanics* [43]. The calculation of the aerodynamic loading on the blade is considered an inner problem while the computation of the wake that is generated as a result of the distribution of blade load is considered an outer problem. The inner and the outer problem solutions can be considered as two separate, but mutually dependent, processes. The dependency arises from the fact that wake solution needs the blade loading (bound circulation) to determine its strength, while the calculation of the aerodynamic loading on the blade needs the induced velocity which is an effect of the distorted vortex wake. The two solution domains must be coupled though a matching procedure.

In traditional single tip-filament-based, free-wake methods, for example, the matching process is quite straightforward. The user generally specifies where the trailing vortex filament is connected to the blade radial location and its initial strength is set equal to the maximum bound circulation on the blade or the total circulation outboard of the peak value at that "azimuthal time step".

The matching procedure turns out to be more complicated in the case of the current higher-order, full-span, free-wake method. In RCAS, the spanwise aerodynamic loading is determined using a lifting-line assumption in which the blade is discretized into a number of segments and the aerodynamic loading is computed at the middle of these segments, which are called aerodynamic computation points, or ACPs. This solution model results in a constant loading on each of the segments. In the higher-order free-wake method, the blades are still discretized into segments,

or panels, but the loading (bound circulation) on each of these segments is piecewise second-order rather than piecewise constant. The problem then is to take the piecewise constant bound circulation from RCAS and fit the piecewise quadratic distribution of the free-wake blade model. This is accomplished through what is referred to as integrated circulation method as formulated by Bramesfeld [14]. This procedure is already being used to update the circulation distribution in a wake row as the elements are stretched and compressed in the spanwise direction due to the relaxation process. This method is discussed next followed by an explanation of how it is used to accomplish the matching procedure in the RCAS-free-wake coupling.

3.2.5.3 Integrated Circulation Method

The integrated value of the quadratic circulation distribution for a given element of distributed vorticity element (with span index i) can be expressed as

$$\Gamma_{i\_total} = \int_{-\eta}^{\eta} \Gamma(\eta) d\eta = \int_{-\eta}^{\eta} (A_i + B_i(\eta_i) + C_i(\eta_i)^2) d\eta \tag{3.14}$$

which results in

$$\Gamma_{i\_total} = 2A_i\eta_i + \frac{2}{3}C_i\eta_i^3 \tag{3.15}$$

To obtain the average circulation across the element, Eq. (3.15) should be divided by $2\eta_i$, the span length of the element, as

$$\Gamma_{i\_average} = A_i + \frac{1}{3}C_i\eta_i^2 = K_i \tag{3.16}$$

The constant K_i in Eq. (3.16) is the same as what was introduced as the constant K in Eq. (2.17).

In the time-stepping methodology used in the current free-wake analysis, K is computed for each of the spanwise distributed vorticity elements on the blade. In a

steady case, K remains unchanged for all the streamwise wake elements emanating from a particular blade spanwise location. In an unsteady case, although the elements in the newest wake row have the same value of K as that for the spanwise blade vorticity elements from which they are created at that particular time step, all the the streamwise elements corresponding to that spanwise location have different values of K.

In either case, during the relaxation process, the wake elements are either compressed or stretched in the spanwise direction. The new geometrical configuration of the elements necessitates the recalculation of the circulation distribution, which basically means recalculating the A, B and C coefficients. In doing so, the integrated circulation, or the parameter K, must remain constant for a given element before and after the relaxation. In the free-wake analysis, this condition is applied to all the elements in a wake row along with the condition of continuity of circulation and vorticity (or the derivative of circulation) between the elements.

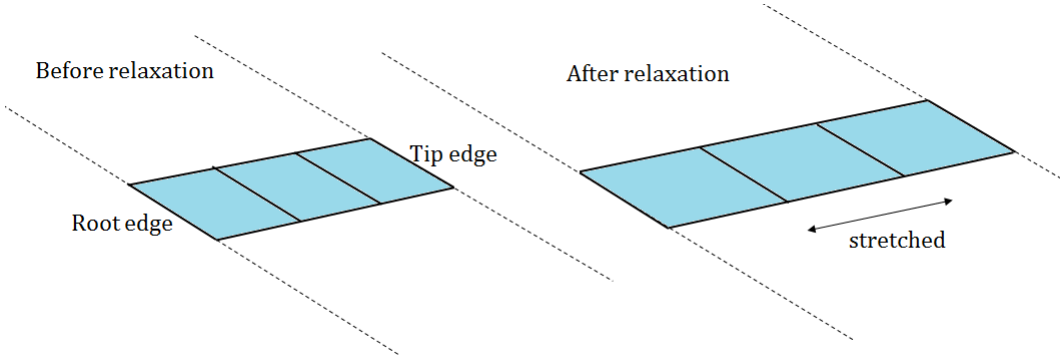

Figure 3.9. Wake row before and after relaxation.

For a blade with three spanwise elements, shown in Figure 3.9, one can write four equations for continuity of circulation and vorticity between the elements, and two equations for prescribing zero circulation at the blade root and tip edges. From these six equations, the A_i coefficients can be eliminated by using Eq. (3.16). The resulting six equations can be expressed in matrix form as

$$\begin{bmatrix} \eta_o & -\frac{2}{3}{\eta_o}^2 & 0 & 0 & 0 & 0 \\ 1 & 2\eta_o & -1 & 2\eta_1 & 0 & 0 \\ \eta_o & \frac{2}{3}{\eta_o}^2 & \eta_1 & -\frac{2}{3}{\eta_1}^2 & 0 & 0 \\ 0 & 0 & 1 & 2\eta_1 & -1 & 2\eta_2 \\ 0 & 0 & \eta_1 & \frac{2}{3}{\eta_1}^2 & \eta_2 & -\frac{2}{3}{\eta_2}^2 \\ 0 & 0 & 0 & 0 & \eta_2 & \frac{2}{3}{\eta_2}^2 \end{bmatrix} \begin{Bmatrix} B_o \\ C_o \\ B_1 \\ C_1 \\ B_2 \\ C_2 \end{Bmatrix} = \begin{Bmatrix} K_o \\ 0 \\ K_1 - K_o \\ 0 \\ K_2 - K_1 \\ -K_2 \end{Bmatrix} \tag{3.17}$$

This matrix equation can be easily solved using a linear algebraic method such as Gaussian elimination. Once the B_i and C_i coefficients are determined, the A_i coefficients can be computed by again using Eq. (3.16).

The same idea can be used to accomplish the matching between RCAS (inner problem) and free-wake method (outer problem) in the coupling framework. The basic idea of the matching procedure adopted in this work is to take the piecewise-constant bound circulation distribution provided by RCAS, shown in Fig. 3.10, and fit a piecewise-quadratic distribution in the blade model in the free-wake analysis. To accomplish this, the integrated circulation method described above is applied at each time step by using the constant bound circulation values Γ_i from RCAS in place of the parameter K_i.

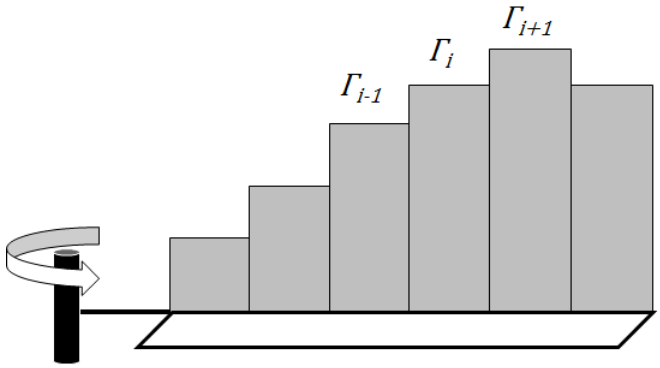

Figure 3.10. Piecewise constant bound circulation distribution in RCAS lifting-line model.

RCAS bound circulation distribution, along with the corresponding matched piecewise quadratic bound circulation distribution in the free-wake model is shown

in Figure 3.11. The markers represent the RCAS piecewise constant values at the mid points of the aerodynamic segments. The curves represent the continuous distributions in the free-wake model. This matching procedure is used for the coupled RCAS-free-wake calcualtions presented in this thesis.

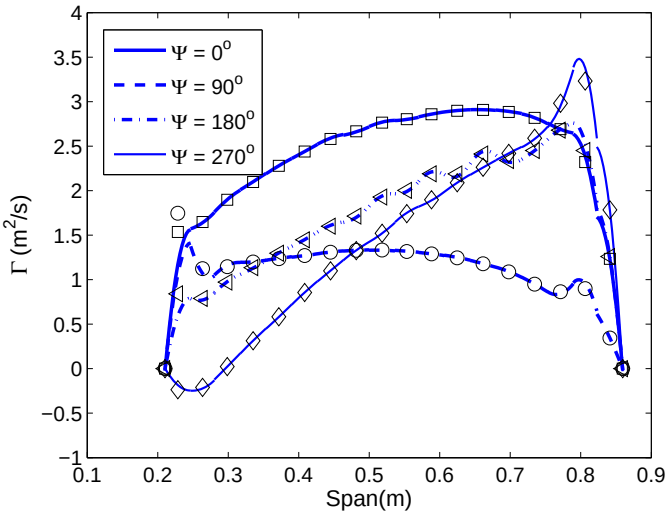

Figure 3.11. Matching bound circulation. Markers represent RCAS piecewise constant values at the mid points of the segments and the curves represent the matched distribution in the free-wake solution. ($\mu = 0.23$ and $C_T = 0.0064$).

3.2.5.4 Convergence of the Coupled Analysis

The convergence of the coupled RCAS-free-wake analysis is based on the relative difference in induced velocity between successive iterations. A parameter to facilitate this is defined as

$$\sigma(v)^n = \frac{\Sigma_i^M \Sigma_j^N (v_{ij}^n - v_{ij}^{n-1})}{\Sigma_i^M \Sigma_j^N v_{ij}^n} \tag{3.18}$$

where $\Sigma_i^M \Sigma_j^N (v_{ij}^n - v_{ij}^{n-1})$ is the sum of the difference between the induced velocities between the current (n) and previous $(n-1)$ iteration for each aerodynamic segment and azimuth on the rotor. $\Sigma_i^M \Sigma_j^N v_{ij}^n$ is the total induced velocity for the current iteration.

Two more parameters tracked in the coupled solution are

$$\Delta(\Gamma)^n = \Sigma_i^M \Sigma_j^N (\Gamma_{ij}^n - \Gamma_{ij}^{n-1}) \tag{3.19}$$

and

$$\Delta(v)^n = \Sigma_i^M \Sigma_j^N (v_{ij}^n - v_{ij}^{n-1}) \tag{3.20}$$

where $\Delta(\Gamma)^n$ is the sum of the difference between the current and the previous iteration bound circulation for each aerodynamic segment and each azimuth on the rotor, and $\Delta(v)^n$ is the sum of the difference between the current and previous iteration induced velocity for each aerodynamic segment and each azimuth.

In order to improve convergence, under-relaxation might be used for both bound circulation and induced velocity data. Using an under-relaxation factors, bound circulation and induced velocity for the current iteration can be written as

$$\Gamma^n = URF_\Gamma \cdot \Gamma^n + (1 - URF_\Gamma) \cdot \Gamma^{n-1} \tag{3.21}$$

and

$$v^n = URF_v \cdot v^n + (1 - URF_v) \cdot v^{n-1} \tag{3.22}$$

An under-relaxation factor of 1 implies there is no under-relaxation, while a factor less than 1 inducates that part of the solution from the previous iteration is used.

Chapter 4
Validation and Results

In this chapter, the predictions of the free-wake method are compared with experimental data as well as with results from other current analysis methods for both hover and forward flight. A preliminary discussion of the capability of the method in capturing the effect of on-blade, partial-span devices is also presented.

4.1 Analysis of Hovering Rotors

For validation, results from the free-wake calculations are compared with three sets of experimental data reported and documented by Caradonna and Tung [17], Knight and Hefner [18], and Boatwright [19]. Comparisons with the first set of data are made to see how well the free-wake method predicts the distributed loading on the blade. The second second set of data provides validation cases for predicting the figure of merit, a time-averaged quantity. The last set of data are used to validate the free-wake method in predicting induced downwash distribution.

4.1.1 Sectional Loading Distribution

The Caradonna-Tung model rotor has two untwisted, untapered, rectangular blades with an NACA 0012 airfoil. The details of the rotor are summarized in Table 4.1. The experimental set up is shown in Fig. 4.1. For the correlation study presented

in this paper, the experimental cases with the collective pitch angles of 5^o, 8^o, and 12^o at an RPM of 1250 were used.

Blade planform	Rectangular
Blade twist	Untwisted
Airfoil	NACA 0012
Number of blades	2
Rotor radius, R	1.143 m
Blade aspect ratio, AR	6.0
Root cut-out, e/R	0.1905 m

Table 4.1. Caradonna-Tung rotor details.

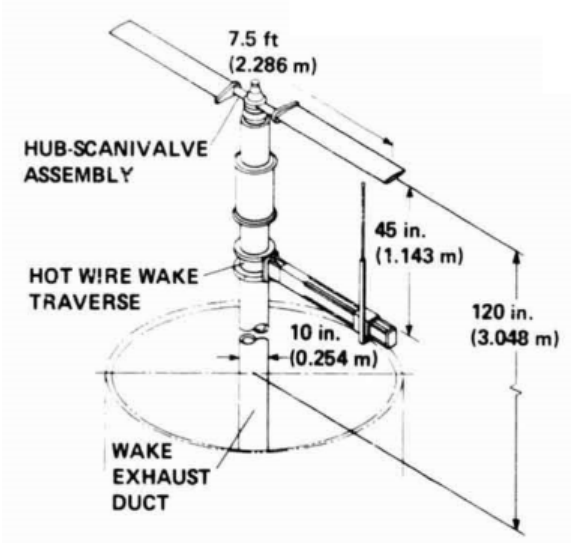

Figure 4.1. The model rotor of Caradonna-Tung experiment [17].

In the calculations, the blade span was modeled with one row of 22 distributed vorticity elements. All of the simulations were performed for a total of 10 revolutions to achieve steady-state results. The azimuthal time step size was 15^o for the first 6 revolutions, and was transitioned smoothly to 9^o for the rest of the simulation. A far wake velocity of 6 m/s (for the wake only) was applied for the first few revolutions for the downward convection of the initial wake vortex sheets. Without this prescription, the wake elements tend to pile up under the rotor, which makes

sense because, since the free-wake method is based on an impulsively started time-stepping approach, there is no velocity field to move the wake elements downwards initially. Moreover, the wake sheets near the center of the rotor tend to shoot up significantly as the simulation progresses due to the induced upwash velocity. It must be pointed out that a certain amount of root-wake shoot-up is indeed observed in actual steady-state operations, and is predicted by computational fluid dynamics.

Figure 4.2 shows that the wake vortex sheet trailing from the blade quickly rolls up at the tip. The outer portion of the wake vortex sheet inboard of the rolled-up tip moves down faster than the inner portion of the sheet due to the strong downwash from the tip roll-up. This has been observed experimentally and reported by Gray [83]. Results from the free-wake simulations look quite promising, as shown in Figure 4.3, in that the method apparently captures the wake contraction without using any empirical correction or special numerical artifice.

The sectional lift coefficients at the collective pitch angles of 5^o, 8^o and 12^o are plotted against the experimental data in Figures 4.4-4.6. The results from the free-wake simulations are seen to correlate well with experimental data. The time-averaged thrust coefficients as a function of collective pitch are plotted in Figure 4.7. Averaged thrust coefficients computed with the free-wake method are within 2% of the measured data.

Since the vortex wake model in this method consists of full-span vortex sheet of distributed vorticity elements, the tip vortex is not a single well-defined filament whose trajectory can be exactly specified by the "Lagrangian markers" moving through space, which is the case in filament-based, free-wake methods. In fact, the vortex sheet originating near the blade tip region rolling up with wake age essentially represents the tip vortex in this method. Although a more exact and accurate method is being developed to compute the equivalent tip vortex trajectory, at this time, an approximate method has been used to quantify the tip vortex

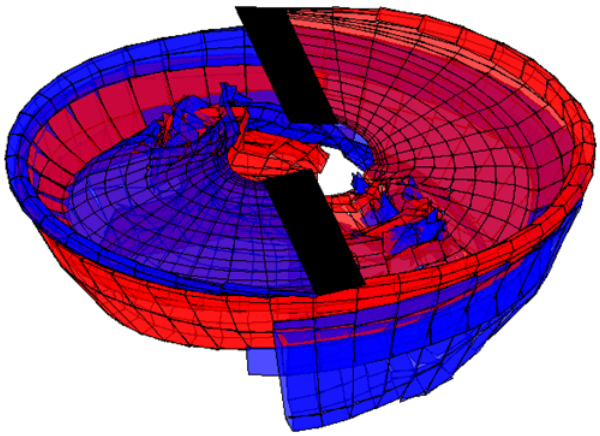

Figure 4.2. Close-up view of the vortex sheet rolling up at the tip.

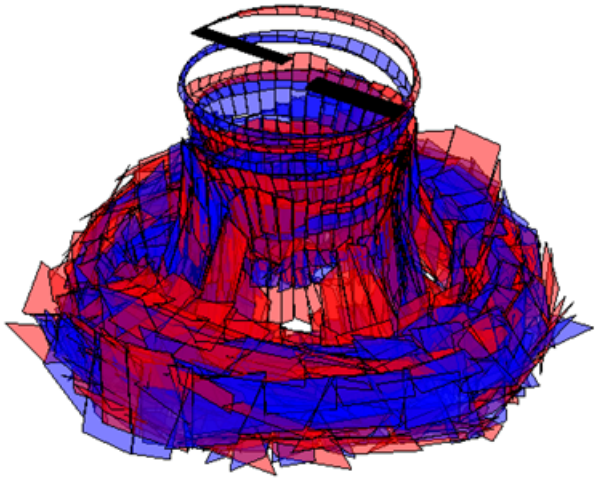

Figure 4.3. Wake geometry (only two tip wake elements shown for clarity).

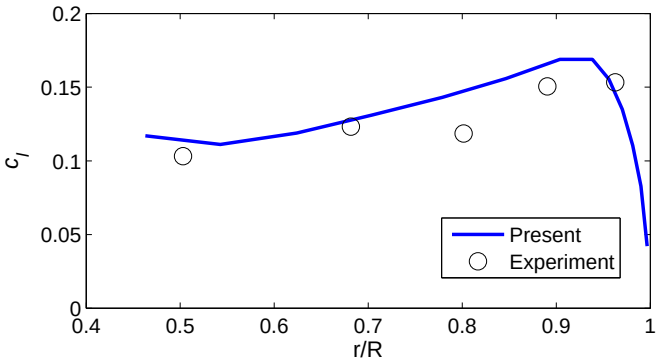

Figure 4.4. Sectional lift coefficient ($\theta_o = 5^o$).

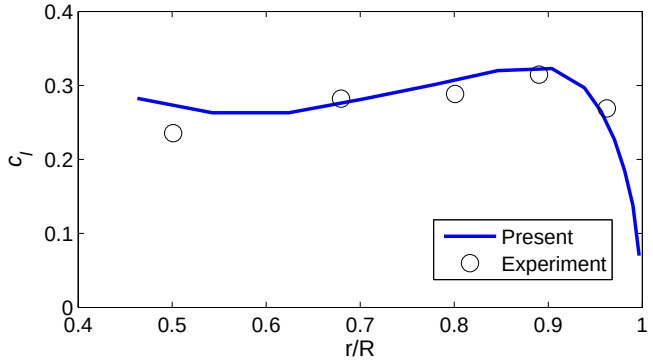

Figure 4.5. Sectional lift coefficient (θ_o =8^o).

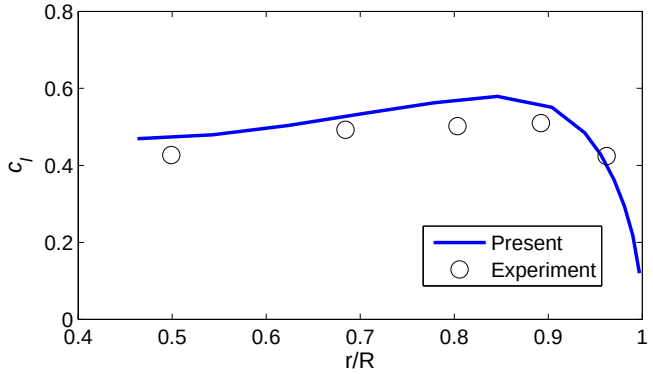

Figure 4.6. Sectional lift coefficient (θ_o =12^o).

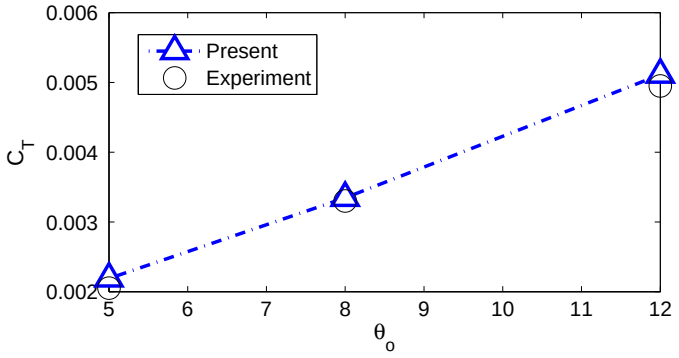

Figure 4.7. Averaged thrust coefficient as a function of collective pitch.

position for comparison with the experimentally measured values. The approximate method involves plotting the top and sides views of the wake geometry up to a wake age of 360^o and measuring the centroid of the vortex sheet that has rolled up at the tip region. Figures 4.8 and 4.9 show the tip vortex position in both the

radial direction (r/R) and axial direction (-z/R) as a function of the wake age. It can be observed that the radial contraction of the wake under the rotor disk plane agrees well with measured values with some deviations beyond the wake age of 300^o. The axial convection of the tip vortex not only agrees well with the measured values, but also captures the change in slope that occurs at 180^o, which is when the following blade passes over the tip vortex generated by the leading or preceding blade.

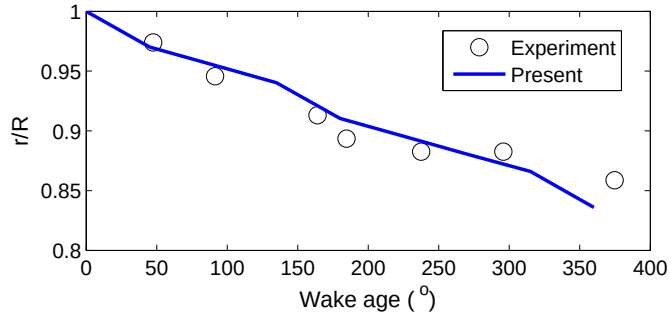

Figure 4.8. Wake contraction below the rotor disk.

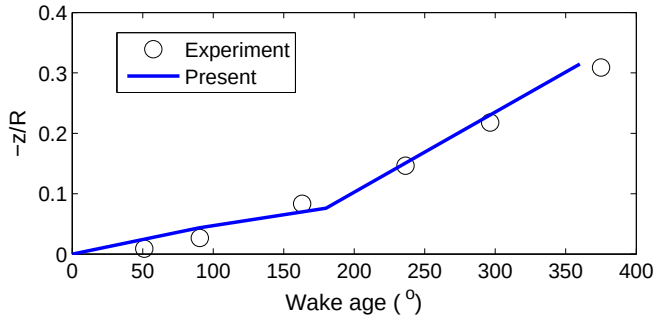

Figure 4.9. Axial wake convection.

4.1.2 Figure of Merit

The figure of merit (FM) is defined as the ratio of ideal power for a hovering rotor obtained from momentum theory and the actual power used by the rotor. This quantity is often used as a measure of how efficient a given rotor is in terms of

generating thrust for a given power. It can be expressed as a function of the total thrust coefficient (C_T) and the power coefficient (C_P) as

$$FM = \frac{1}{\sqrt{2}} \frac{{C_T}^{3/2}}{C_P} \tag{4.1}$$

A model rotor experiment conducted by Knight and Hefner [18] was chosen to validate the free-wake method in predicting the figure of merit. The experimental model rotor has untwisted, untapered, rectangular blades that employ an NACA 0015 airfoil. The rotor is spun at an RPM of 960. The details of the rotor are summarized in Table 4.2.The set up for this experiment is shown in Figure 4.10.

Blade planform	Rectangular
Blade twist	Untwisted
Airfoil	NACA 0015
Number of blades	2, 3 and 4
Rotor diameter, D	1.524 m

Table 4.2. Details of the Knight and hefner experimental rotor.

Figure of merit as a function of thrust coefficient for 2, 3 and 4-bladed rotors were computed with the free-wake model and compared with experimental data, as shown in Figures 4.11-4.13. The calculated results are slightly over-predicted, but the correlation is quite good given the level of fidelity of the analysis. The trends are predicted well as the blade number or the solidity of the rotor is increased. The slight discrepancy may be attributed to the fact that the data for the NACA 0015 airfoil used in the free-wake calculations, which are taken from the U.S. Army C81 tables, are slightly different from what were measured for the blade sections in 2-D wind-tunnel tests that were conducted as part of the experimental study.

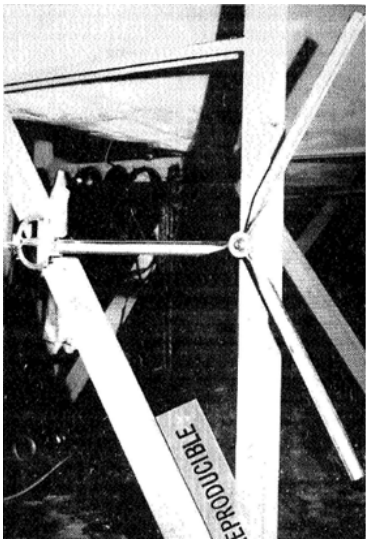

Figure 4.10. The model rotor experiment of Knight and Hefner [18].

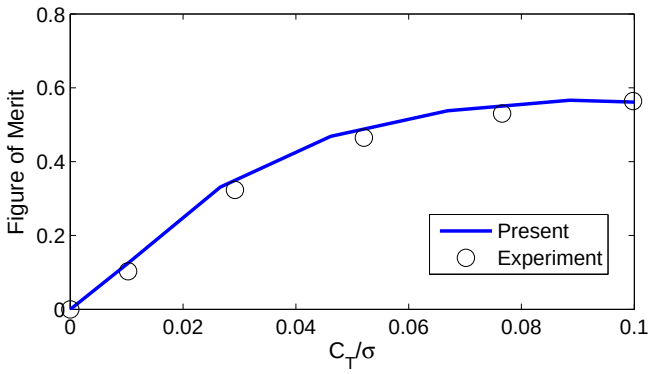

Figure 4.11. Figure of merit vs C_T/σ for a 2-bladed rotor.

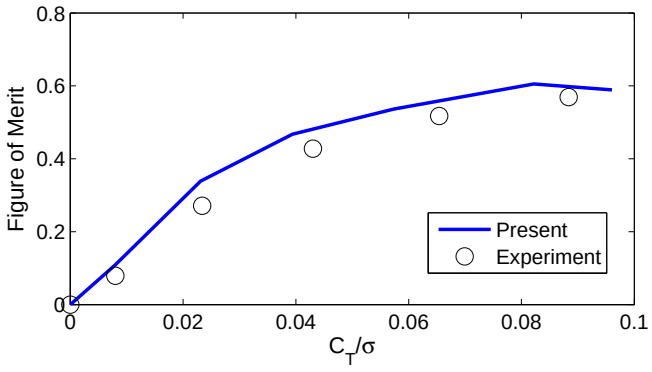

Figure 4.12. Figure of merit vs C_T/σ for a 3-bladed rotor.

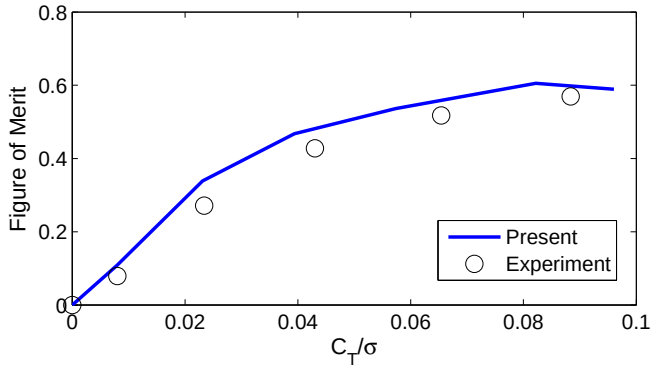

Figure 4.13. Figure of merit vs C_T/σ for a 4-bladed rotor.

4.1.3 Downwash Distribution

The free-wake method was also used to predict the wake-induced downwash for a two-bladed rotor in hover as shown in Figure 4.14. A series of measurements of the wake-induced downwash velocities below and downstream of the rotor was obtained by Boatwright [19]. The details of the rotor are organized in Table 4.3.

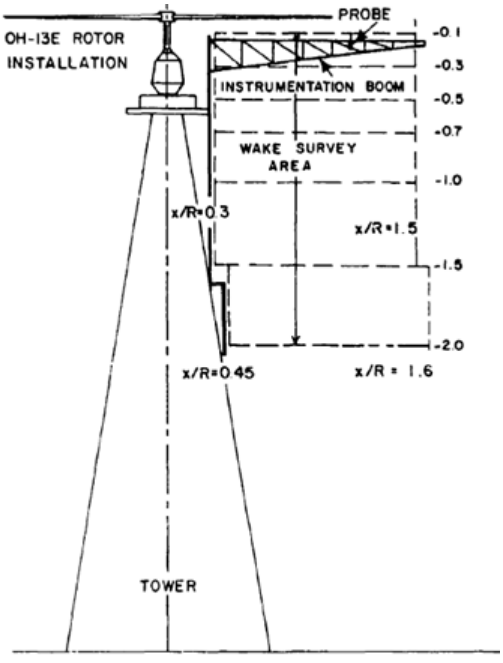

Figure 4.14. The full-scale rotor experiment of Boatwright [19].

Number of blades	2
Airfoil	NACA 0015
Blade twist	Linear twist of -4^o
Rotor diameter	10.71 m
Root cut-out, e/R	0.53 m
Blade area, A	1.64 m^2
Blade root chord, c_{root}	0.36 m
Blade tip chord, c_{tip}	0.26 m

Table 4.3. Boatwright's full-scale rotor details.

In the experiment, the rotor was mounted on a 60 ft rotor test tower. The three components of the wake-induced velocity were measured with a split-film, total-vector anemometer. The data were taken at blade azimuth angles of 0^o, 45^o, 90^o and 135^o for each revolution. The induced velocities were processed to generate time-averaged values for each station at various distances below the rotor disk plane. Figures 4.15 -4.18 show the comparisons of the computed time-averaged downwash with the measured data at $\psi = 0^o$ at four different vertical stations below the rotor disk, specifically at z/R = -0.1, -0.3, -0.5 and -0.7. In the experiment, the rotor operated at a tip speed of 450 ft/s with $C_T = 0.004$. The simulation was run at the same tip speed, but trimmed to $C_T = 0.0039$, with an error of 2.5%. The data presented in each of the plots in Figures 4.15-4.18 represent the variations of time-averaged downwash along the radial stations at different vertical distances below the rotor disk. It can be seen that the correlation is quite good closer to the disk plane. The experimentally measured downwash profile shows that the rotor wake rapidly contracts around r/R = 0.8 after it leaves the disk plane. This contraction of the wake is captured somewhat accurately by the free-wake method , as shown by what could be seen as good correlations at z/R = -0.1, -0.3 and, -0.5. For comparison, predictions using the viscous vortex particle method (VVPM) are also included for z/R = -0.1 and z/R = -0.5. The VVPM results are taken from Ref. [11]. At z/R = -0.7, the free-wake method predicts a slightly over-contracted

wake when compared to the measured profile. This could be due to the influence of the strong rolled-up initial wake vortex sheets, which is not cut off or whose vorticity does not diffuse. It should be noted that, in reality, the vorticity far downstream of the rotor disk undergoes diffusion due to the effect of fluid viscosity.

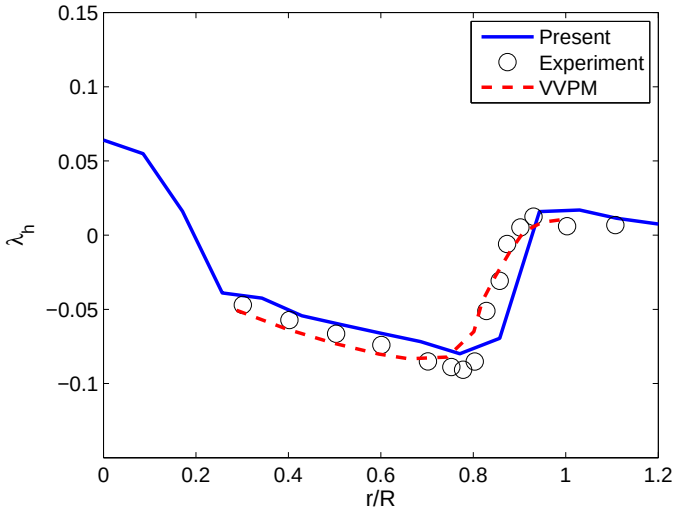

Figure 4.15. Downwash distribution (z/R = - 0.10)

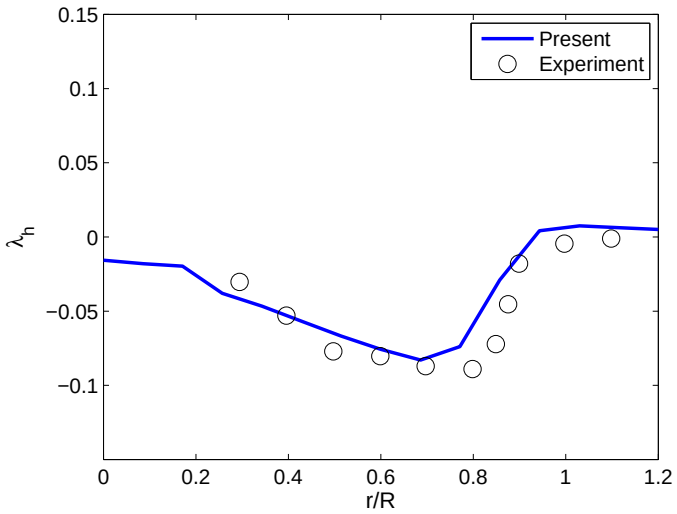

Figure 4.16. Downwash distribution (z/R = - 0.30)

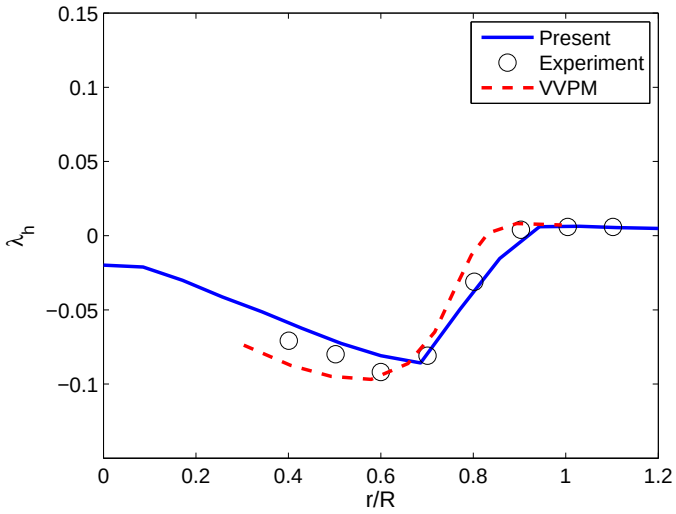

Figure 4.17. Downwash distribution (z/R = - 0.50)

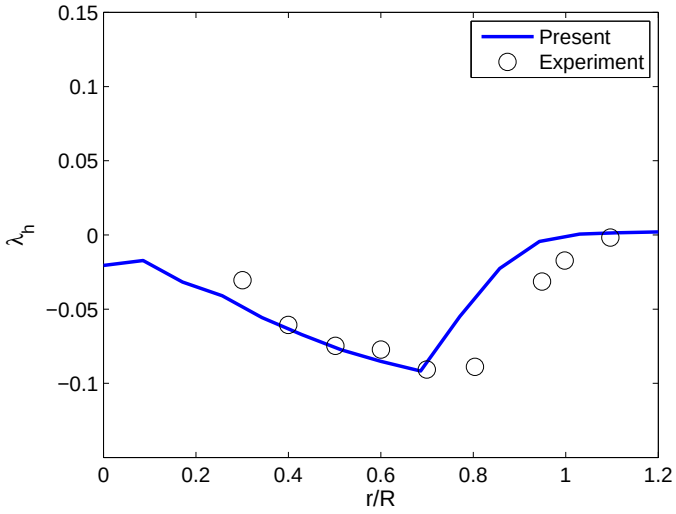

Figure 4.18. Downwash distribution (z/R = - 0.70)

4.2 Analysis of Rotors in Forward Flight

As a validation of the current free-wake model, the results of trimmed free-wake solution are compared with test data for several flight conditions. The predictions of the current method are also compared with other computational models. Lastly, discussion of a preliminary application of the current method in modeling an on-blade device is presented.

4.2.1 Wake Geometry

Three views of a wake geometry obtained from a free-wake calcualtion are shown in Figures 4.19, 4.20 and 4.21. The color fills in the pictures represent the wake vortex sheets emanating from individual blades and do not indicate the vorticity strengths. Figure 4.22 provides a closer look at the wake near the blades. It should be observed how the wake sheets roll up along their outer edges not long after being shed from the generating blades (indicated by the darker shades along the wake edges), constituting what would be essentially the tip vortices. Capturing or resolving these vortices is critical for certain rotor operating conditions, specifically at lower advance ratios, due to the fact that the following blades pass close to the vortices which are generated either by the same blade during the previous revolution, or by the other blades constituting the rotor. Such an encounter is called blade-vortex interaction (BVI), which is a source of undesirable unsteady airloads that results in vibration and noise. Figure 4.22 shows some of the possible locations where the tip vortices tend to interact with the blades. In traditional filament-based free-wake methods, tip vortices are explicitly modeled using vortex filaments with a user-specified core size to prevent numerical instability. In contrast, the higher-order, free-wake method discussed herein uses continuous vortex sheets that naturally roll up along their edges and does not require explicit modeling of tip vortices, which removes one important parameter that needs "tweaking"

when using traditional, filament-based free-wake analyses. The wake relaxation and roll-up behavior captured by the current method are observed to be very stable, and consequently, because the singularity issues have been eliminated, it is possible to extend the wake considerably downstream than is typically possible with filament-based methods.

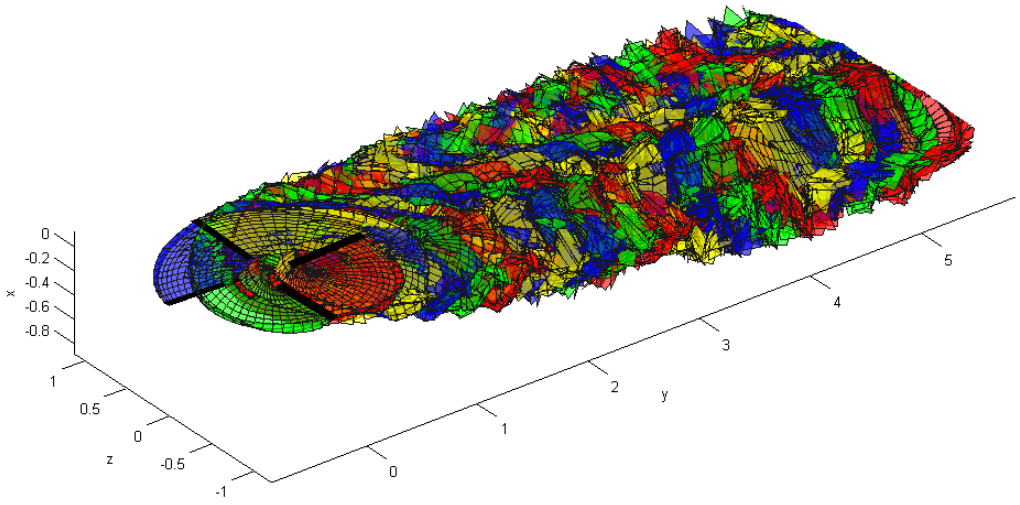

Figure 4.19. Wake geometry. $\mu = 0.23$, $\alpha_{TPP} = -3^o$ and $C_T = 0.008$.

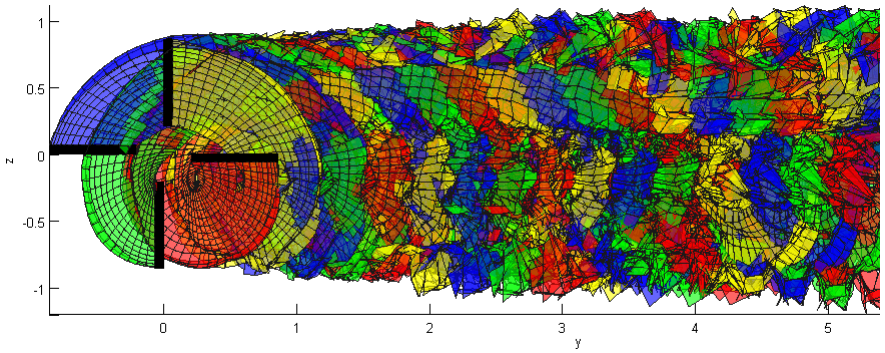

Figure 4.20. Top view of the wake geometry ($\mu = 0.23$, $\alpha_{TPP} = -3^o$ and $C_T = 0.008$).

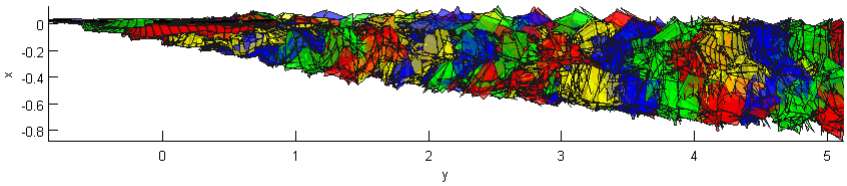

Figure 4.21. Side view of the wake geometr ($\mu = 0.23$, $\alpha_{TPP} = -3^o$ and $C_T = 0.008$).

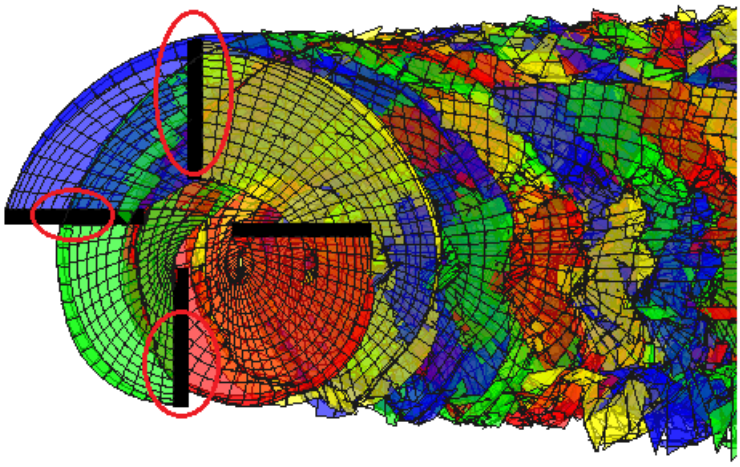

Figure 4.22. CLose-up schematic of the wake geometry showing the possible locations of blade vortex interactions ($\mu = 0.23$, $\alpha_{TPP} = -3^o$ and $C_T = 0.008$).

4.2.2 Rotor Induced Inflow

The comparison of the induced inflow predicted by the free-wake model with the experimental data is discussed in this section. The test cases used for the current validation effort are attributed to Elliot et al. [84–86]. The experimental setup is shown in Figures 4.23, in which inflow was measured through a series of rotors with different planforms, under various operating conditions, in the the presence of the ROtorBodyInteraction (ROBIN) fuselage. In the tests, a laser-Doppler velocimetry (LDV) system was used to measure the induced velocity components normal and parallel to the rotor tip path plane (TPP). These measurements were made at a number of azimuthal locations on planes located above the TPP (on the order of

the blade chord).

During the tests the rotor TPP was maintained at -3^o relative to the freestream by zeroing the blade flapping relative to the shaft and setting the shaft angle to -3^o. The operating speed of the rotor was held to 2113 RPM for all the test cases discussed in this study. The data collection procedure consisted of placing the sample volume at the location to be measured and acquiring data for a period of about two minutes, or until about 4096 velocity measurements were made for either the inplane and the velocity component that is normal to the rotor plane.

The four-bladed rotor hub is fully articulated with lead-lag, feathering, and flapping degrees of freedom. The rotor blades used in the tests were chosen to be very stiff in order to reduce any aerodynamic uncertainty that might be caused by blade flexing. In all the calculations presented in this work, the blades are modeled as being rigid and the lead-lag degree of freedom is neglected. Also, the computations do not account for the presence of the fuselage. The rotor/blade parameters used in this study are detailed in Table 4.4.

Airfoil section	NACA 0012
Blade chord, c (in)	2.7
Rotor rotation	CCW from above
Hinge offset, e/R	0.06
Blade flapping inertia, I_β(slug/ft^2)	0.046
Linear twist	-8^o
Blade mass, $M_B(lb)$	0.572
Number of blades, N_B	4
Blade planform	rectangular
Rotor radius, R (in)	33.88
Root cutout, r_c/R	0.24
Solidity, σ	0.0064

Table 4.4. Rotor parameters used in the simulations

In all the calculations presented in this section, the blade is modeled with one row of 18 equal-span distributed vorticity elements as shown in Figure 4.24. The

Figure 4.23. Wind-tunnel model used for the current validation cases. [20]

reason for using a uniform paneling is described in the appendix A of this thesis.

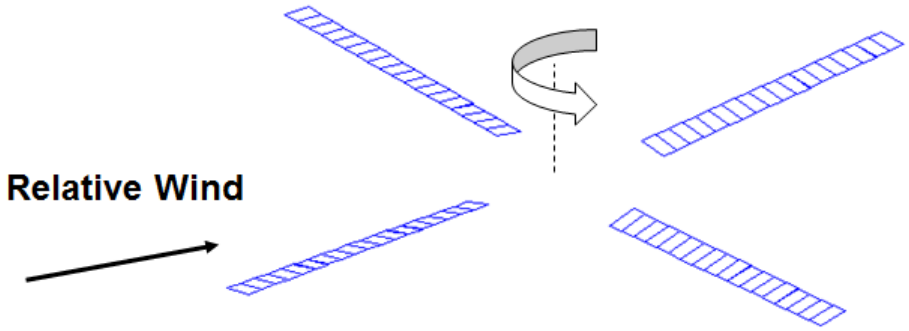

Figure 4.24. Rotor model used in the free-wake analysis.

The validation cases along with the associated operating conditions presented in this section are tabulated in Table 4.5.

Case	μ	α_{TPP}	C_T
I.	0.23	-3^o	0.0064
II.	0.15	-3^o	0.0064
III.	0.30	-4^o	0.0065
IV.	0.23	-3^o	0.0080

Table 4.5. Summary of validation cases presented in this section.

4.2.2.1 Case I.

The first validation case presented here is for a moderate advance ratio of 0.23 and $C_T = 0.0064$. The induced velocity is sampled at a height of $1.15c$ above the tip path plane of the rotor in both the lateral and the longitudinal planes passing through the center of the rotor. The predicted values are then compared with the measured inflow distribution. The lateral inflow comparison is shown in Figure 4.25 with the vertical bars indicating standard deviations of the data. The experimental data for this validation are taken from Ref. [85]. The qualitative correlation is very good with the predicted inflow distribution closely following the general shape of the measured data. Part of the reason for the slight over-prediction of downwash may be attributed to the fact that the sampling plane in the simulation is slightly closer to the rotor than in the test. The slight difference in the height of the sampling planes arises from the fact that the coning angle in the free-wake simulation is slightly lower than that measured in the test. The predicted distribution, which is obtained by time-averaging over one rotor revolution, is approximately within one standard deviation of the measured data. The longitudinal inflow comparison is shown in Figure 4.26 where it can be observed that the measured data displays a strong upwash on the front part of the rotor disk and a strong downwash on the rear part of the rotor disk. The free-wake method captures these phenomena qualitatively well with a slight over-prediction over the front half of the rotor extending from about 0.5R to 0.95R. Again, this can partly be attributed to the difference in height of the sampling planes in the simulation and the test. The

comparison of control inputs and the rotor response parameters are detailed in Table 4.6.

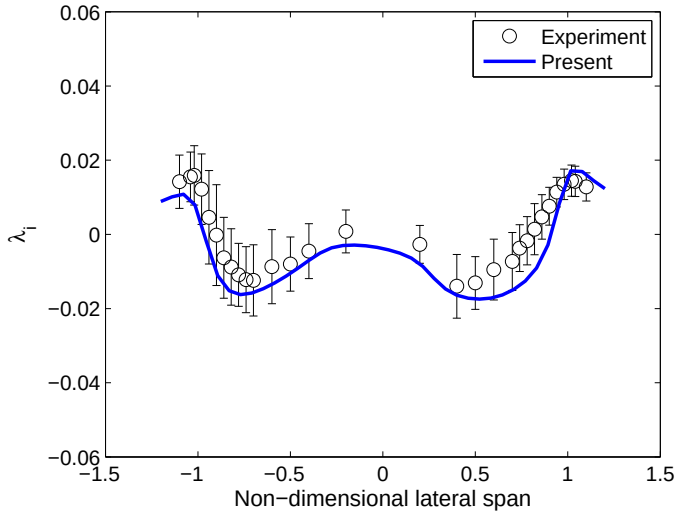

Figure 4.25. Lateral inflow distribution at $1.15c$ above the TPP ($\mu = 0.23$, $\alpha_{TPP} = -3^o$ and $C_T = 0.0064$).

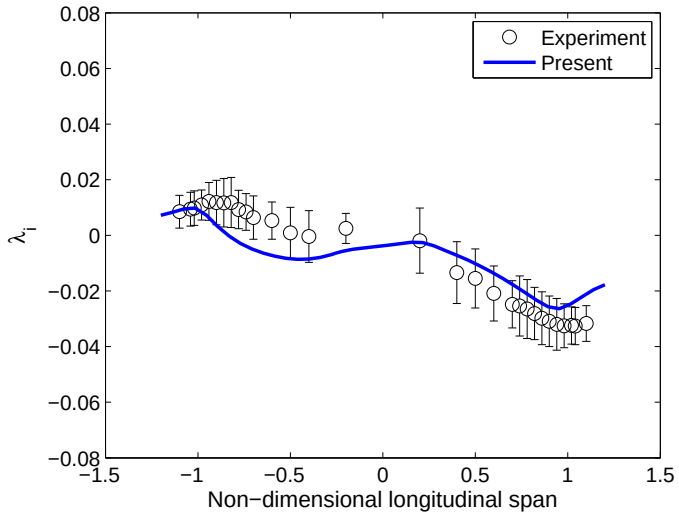

Figure 4.26. Longitudinal inflow distribution at 1.15c above the TPP ($\mu = 0.23$, $\alpha_{TPP} = -3^o$ and $C_T = 0.0064$).

Figure 4.27 shows the variation of bound circulation around the azimuth for this case. It can be observed that the rotor is more loaded at the rear than at the

	μ	C_T	θ_0	θ_{1c}	θ_{1s}	β_0	β_{1c}	β_{1s}
Experiment [85]	0.23	0.0064	8.16^o	1.52^o	-4.13^o	1.8^o	0.00^o	0.00^o
Present	0.23	0.0064	7.52^o	1.55^o	-3.26^o	1.5^o	0.00^o	0.00^o

Table 4.6. Comparison between experiment and prediction for case I.

front, generating a pitch-down moment that counteracts the natural tendency of the rotor TPP to tilt back, which was necessary in the experiment to get rid of the longitudinal tilt with respect to the rotor shaft. The cancellation of the lateral tilt of the rotor with respect to the shaft is not immediately apparent from the bound circulation distribution, which appears to be loaded more on the retreating side. However, it must be recognized that the actual loading is proportional to $\rho_\infty V_\infty \Gamma_\infty$, instead of just Γ_∞. The product of the much higher velocity on the advancing side and the lower bound circulation there actually results in a net rolling moment that counteracts the natural tendency of the rotor TPP to tilt to the right. It should also be observed that in this flight condition, there exists a pocket of negative loading near the center of the rotor on the advancing side that approximately extends from $\psi = 225^o$ to $\psi = 315^o$.

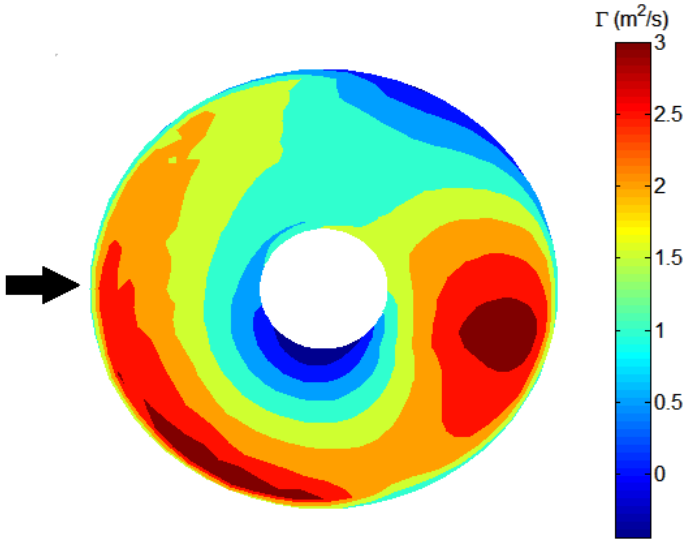

Figure 4.27. Variation of bound circulation with azimuth ($\mu = 0.23$ and $C_T = 0.0064$).

Figures 4.28 and 4.29 show the convergence of the trim variables, which in the current simulation are the rotor thrust coefficient, C_T, the longitudinal flapping coefficient, β_{1c}, and the lateral flapping coefficient, β_{1s}. The trim variables at the first iteration are those obtained after the first coupling iteration in which RCAS uses the inflow from the first run of the free-wake simulation and performs a periodic solution. It should be observed that the trim variables quickly converge to the target trim values specified in the RCAS input script. These trim target values are specified to match the conditions in the test. The control variables used to trim the rotor are the collective pitch, θ_o, the lateral cyclic pitch, θ_{1c}, and the longitudinal cyclic pitch, θ_{1s}. The convergence of the control variables are shown in Figure 4.30, where it can be seen that after the first coupling iteration, the controls quickly converge to a more or less steady values.

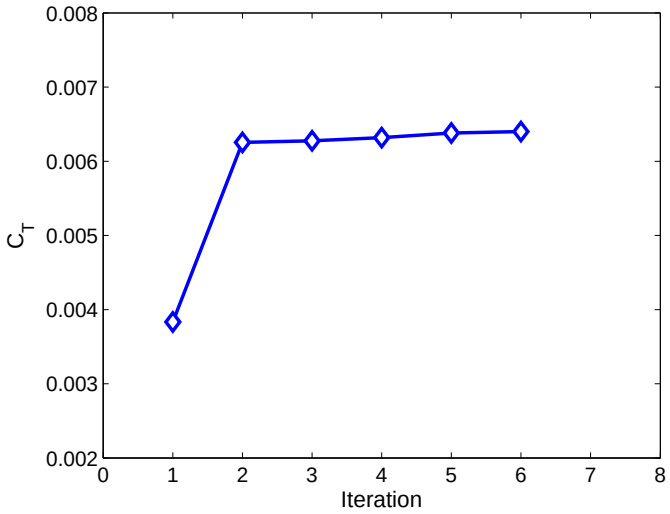

Figure 4.28. Convergence of thrust coefficient ($\mu = 0.23$, $\alpha_{TPP} = -3^o$ and $C_T = 0.0064$).

As discussed in section 3.2.5.4, convergence of the coupled RCAS-free-wake solution is determined by tracking the relative change in induced velocity field computed in two successive coupling iterations. It can be observed in Figure 4.31 that the relative difference in inflow is about 20% at the end of the second iteration, which decreases monotonically to about 2% at the end of sixth iteration. Since the

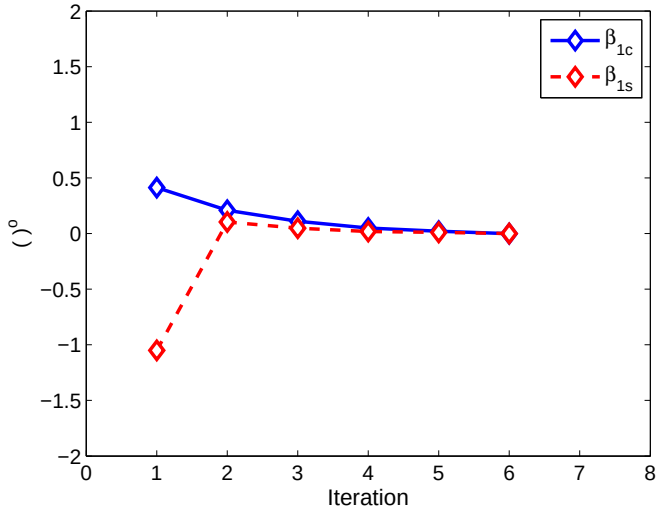

Figure 4.29. Convergence of blade flapping coefficients ($\mu = 0.23$, $\alpha_{TPP} = -3^o$ and $C_T = 0.0064$).

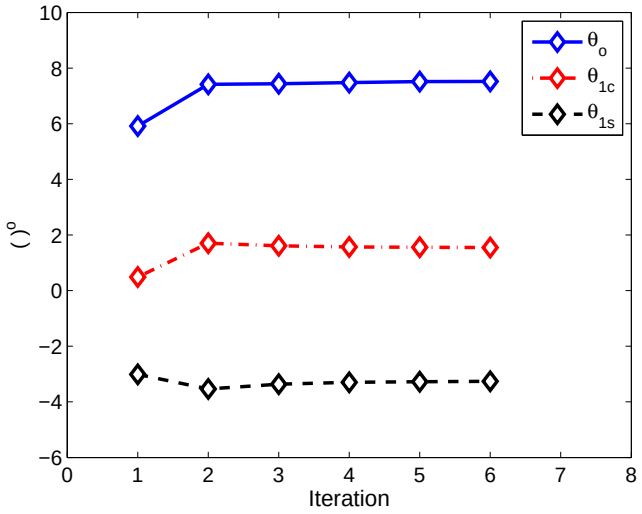

Figure 4.30. Convergence of the pitch control coefficients ($\mu = 0.23$, $\alpha_{TPP} = -3^o$ and $C_T = 0.0064$).

tolerance in relative inflow is chosen to be 3% in the current simulation, RCAS terminates the coupling at this point and considers the solution to be converged. The convergence behaviors of bound circulation and induced velocity are shown in Figure 4.32. The under-relaxation factors used were 0.4 and 0.8 for bound circulation and induced velocity respectively in all the solutions presented in this

thesis.

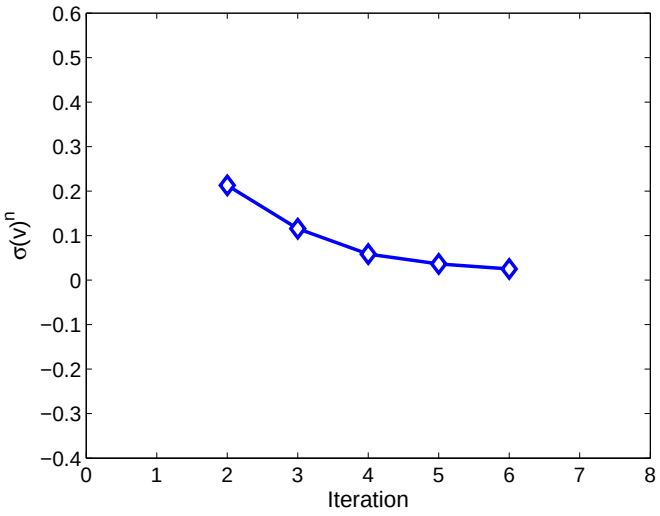

Figure 4.31. Convergence of relative difference in inflow ($\mu = 0.23$, $\alpha_{TPP} = -3^o$ and $C_T = 0.0064$).

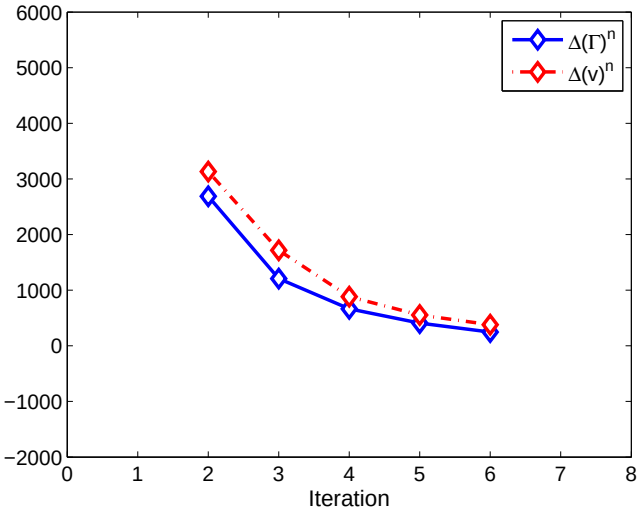

Figure 4.32. Convergence of bound circulation (ft^2/s) and induced velocity (ft/s) ($\mu = 0.23$, $\alpha_{TPP} = -3^o$ and $C_T = 0.0064$).

The convergence of the final free-wake run is shown in Figure 4.33. The convergence tolerance in all of the simulations presented in this thesis was specified to be $\epsilon = 0.03$, meaning that the solution is considered to be converged when the

change in induced velocity computed between two successive revolutions is less than 3%. Also, the "blade phasing" was activated when the blade has completed two revolutions to account for multiple blades. For this case, the L_2-norm decreased dramatically from approximately 13% to less than 3% at the end of third revolution.

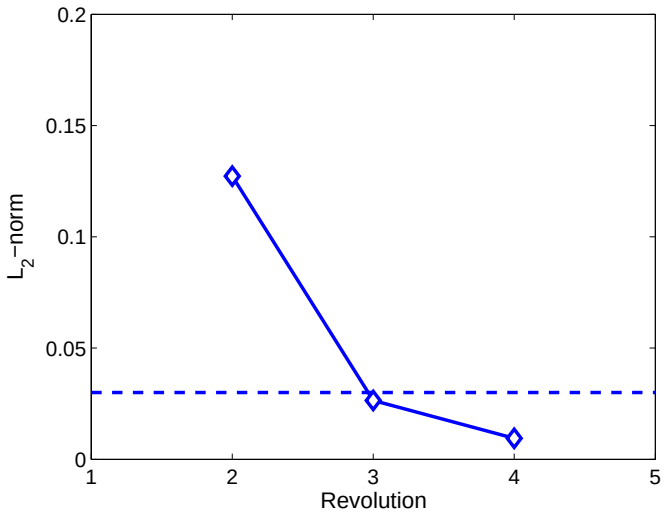

Figure 4.33. Convergence of L_2-norm of induced velocity in the free-wake program. Dashed line represents the user-specified tolerance ($\epsilon = 0.03$).($\mu = 0.23$, $\alpha_{TPP} = -3^o$ and $C_T = 0.0064$).

4.2.2.2 Case II.

The second validation case presented here is that for a lower advance ratio of 0.15. In the test, the rotational speed of the rotor was still maintained at 2113 RPM, but the freestream velocity was decreased from 143.90 ft/s to 92.82 ft/s. The controls were adjusted so that 1/rev lateral and longitudinal flapping with respect to the rotor shaft were zeroed, with the averaged thrust coefficient measured to be 0.0064. The rotor shaft was pitched nose-down at an angle of 3^o. The experimental data presented here are from Ref. [84]. Figures 4.34 and 4.35 show the comparison of predicted lateral and longitudinal time-averaged, inflow distributions with the test data. The vertical bars represent the standard deviations of the measured data. The correlations are seen to be excellent everywhere except at the rear half of the rotor

in the longitudinal plane, where the downwash is slightly under-predicted compared to the test data. The predicted variations are within 12% of the experimental mean values everywhere except at the rear half of the rotor, outboard of 0.2R, where the inflow is underpredicted by approximately 35%.

The bound circulation variation with respect to rotor azimuth is shown in Figure 4.36. Again, the rotor is more aft-loaded to cancel the natural longitudinal tilting back of the TPP. A pocket of negative loading is observed around $\psi = 85^o$. At this advance ratio, no negative loading is observed around the location where the computations predicted one for the case of $\mu = 0.23$.

The convergence history of the trim variables and the controls are shown in Figures 4.37, 4.38 and 4.39. It can be observed that after the second coupling iteration, these parameters exhibit steady convergence.

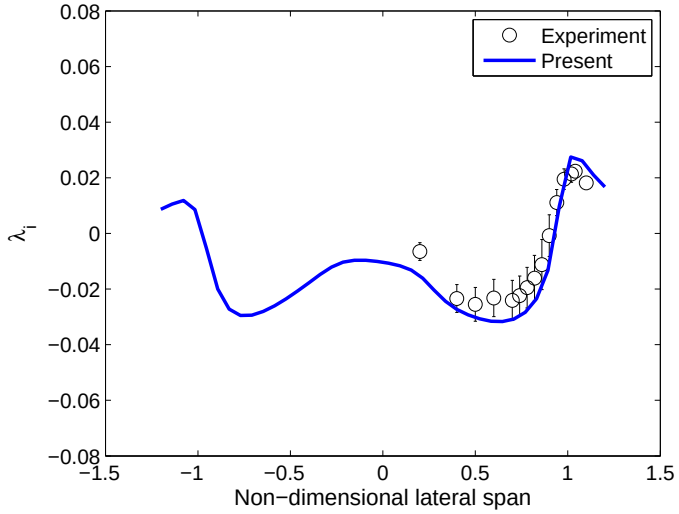

Figure 4.34. Lateral inflow distribution at 1.15c above the TPP ($\mu = 0.15$, $\alpha_{TPP} = -3^o$ and $C_T = 0.0064$).

The solution required a few more coupling iterations to converge for this case as shown in Figure 4.40, where the relative difference in induced velocity decreased from about 22% at the end of the second iteration to less than 3% at the end of the eighth iteration. The bound circulation and induced velocity histories show a

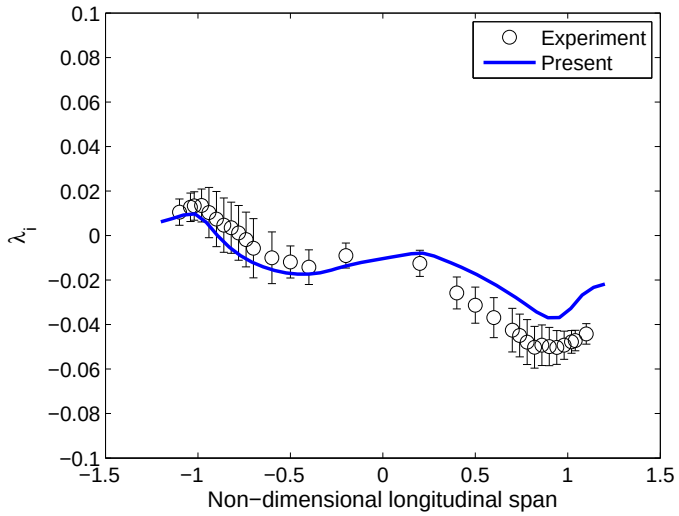

Figure 4.35. Longitudinal inflow distribution at 1.15c above the TPP ($\mu = 0.15$, $\alpha_{TPP} = -3^o$ and $C_T = 0.0064$).

	μ	C_T	θ_0	θ_{1c}	θ_{1s}	β_0	β_{1c}	β_{1s}
Experiment [84]	0.15	0.0064	9.4^o	1.1^o	-3.2^o	1.5^o	0.00^o	0.00^o
Present	0.15	0.0064	7.35^o	1.72^o	-1.92^o	1.5^o	0.00^o	0.00^o

Table 4.7. Comparison between experiment and prediction for case II.

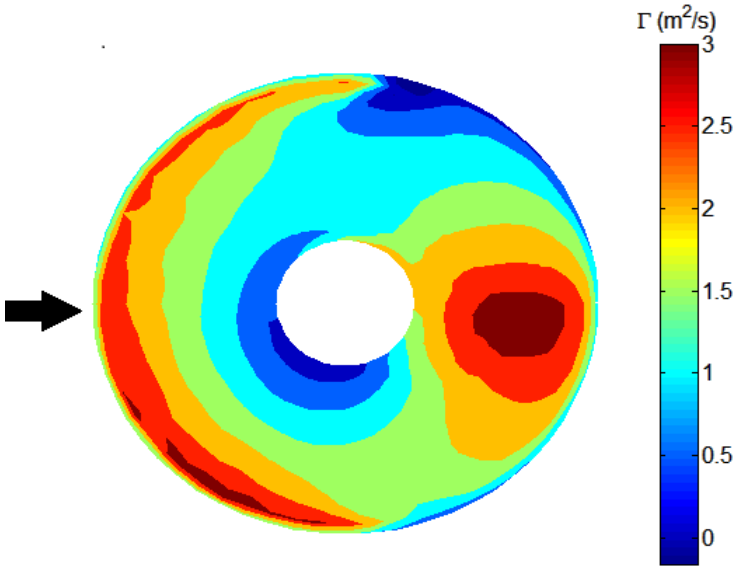

Figure 4.36. Variation of bound circulation with azimuth ($\mu = 0.15$ and $C_T = 0.0064$).

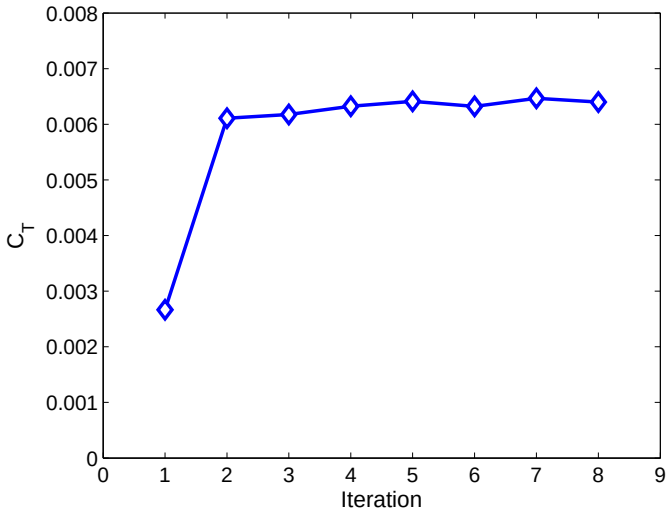

Figure 4.37. Convergence of thrust coefficient ($\mu = 0.15$, $\alpha_{TPP} = -3^o$ and $C_T = 0.0064$).

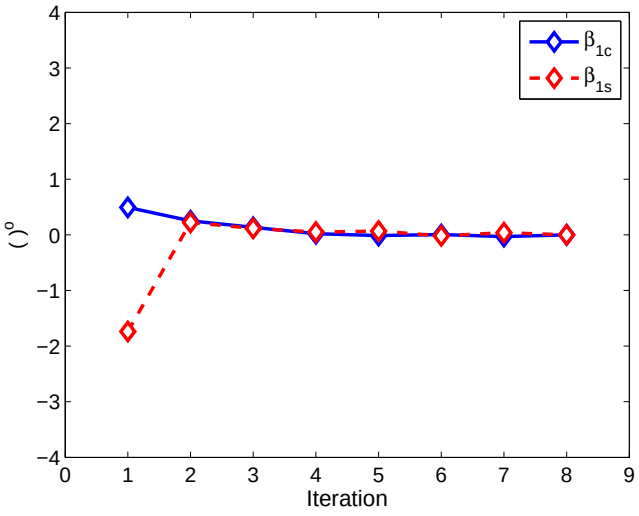

Figure 4.38. Convergence of blade flapping coefficients ($\mu = 0.15$, $\alpha_{TPP} = -3^o$ and $C_T = 0.0064$).

dramatic decrease from the second to the fourth iteration after which the quantities continued to decrease but at a lower rate as shown in Figure 4.41.

The convergence history of the last free-wake run is shown in Figure 4.42. It can be observed that the free-wake solution took longer to converge compared to the higher advance ratio discussed before. The L_2-norm is 17% at the end of the

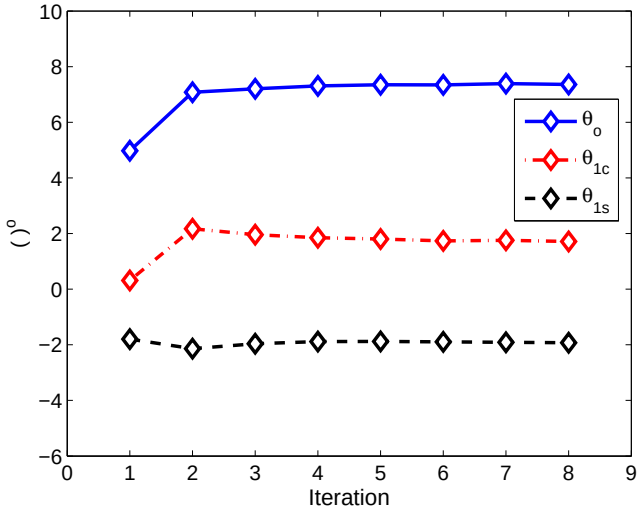

Figure 4.39. Convergence of the pitch control coefficients ($\mu = 0.15$, $\alpha_{TPP} = -3^o$ and $C_T = 0.0064$).

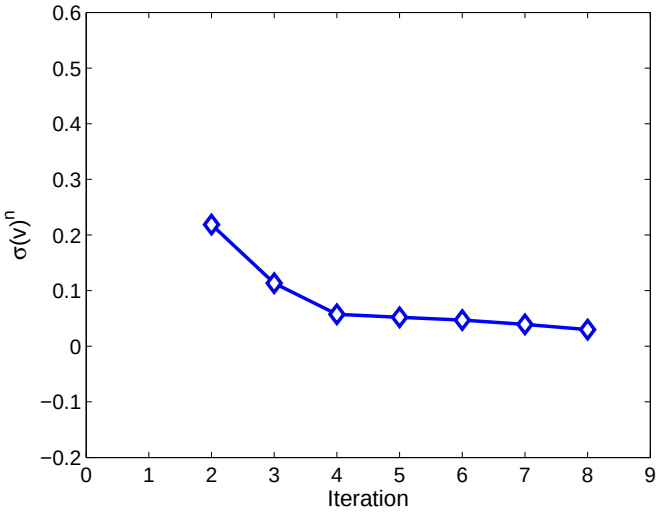

Figure 4.40. Convergence of relative difference in inflow ($\mu = 0.15$, $\alpha_{TPP} = -3^o$ and $C_T = 0.0064$).

second revolution, and it took four more revolutions to converge. This is to be expected because the generated wake system stays close to the rotor for a longer period of time compared to a situation with a higher advance ratio.

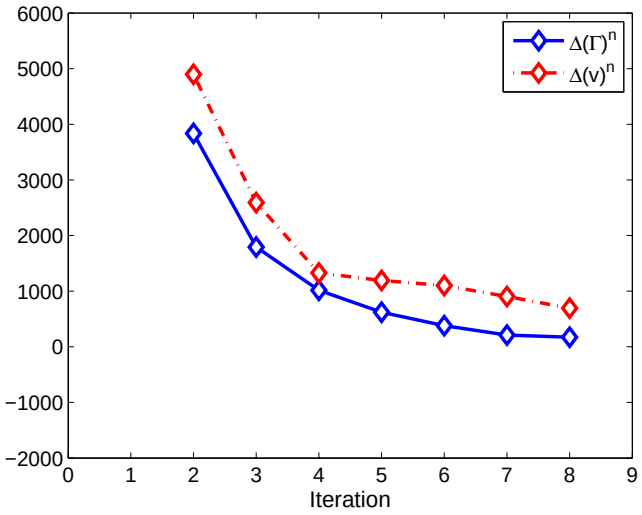

Figure 4.41. Convergence of bound circulation (ft^2/s) and induced velocity (ft/s) ($\mu = 0.15$, $\alpha_{TPP} = -3^o$ and $C_T = 0.0064$).

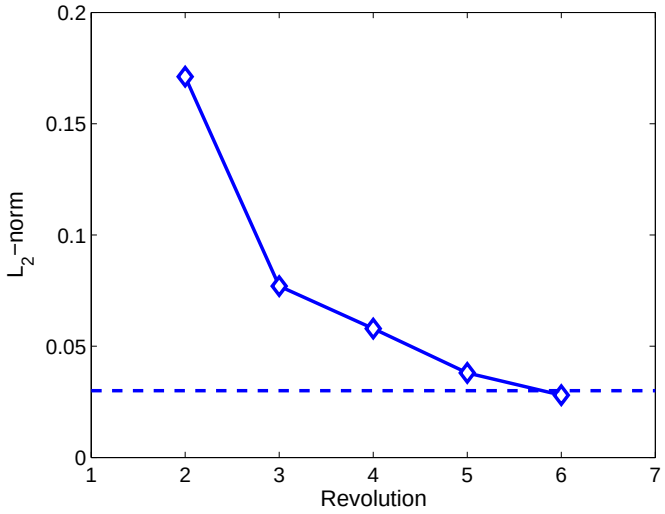

Figure 4.42. Convergence of L_2-norm of induced velocity in the free-wake program. Dashed line represents the user-specified tolerance ($\epsilon = 0.03$).($\mu = 0.15$, $\alpha_{TPP} = -3^o$ and $C_T = 0.0064$).

4.2.2.3 Case III.

The third validation case discussed here is for a higher advance ratio of 0.30. The speed of the rotor was still maintained at 2113 RPM in the test, but the freestream velocity was changed to 187.35 ft/s. Again, the controls were adjusted to eliminate

the 1/rev lateral and longitudinal cyclic flapping with respect to the rotor shaft. The averaged thrust coefficient was measured to be 0.0065. The rotor shaft was pitched nose-down at an angle of 4^o. The test data shown here are taken from Ref. [86]. Figures 4.43 and 4.44 show the comparison of predicted lateral and longitudinal time-averaged inflow with the experimental data with the vertical bars representing the standard deviation of the experimental data. The inflow in regions inboard of about 0.9R is consistently over-predicted by the free-wake calculation. Some or all of the observed discrepancies between the measurement and prediction may be due to the fact that the sampling planes in the simulation and experiment are slightly different, as can be seen in the slight difference in coning angles listed in Table 4.8. A prediction using the University of Maryland free-wake analysis (UMD-FW) is also plotted to put the prediction of the higher-order, free-wake analysis in perspective. The UMD-FW results are taken from Ref. [54]. UMD-FW also consistently over-predicts downwash, compared to which the present free-wake method does a much better job of capturing the trend of the measured data, especially between -0.75R to 0.5R.

Azimuthal variation of bound circulation computed by the present free-wake method for this case is shown in Figure 4.45. Compared to the case for $\mu = 0.23$, the negative loading at this advance ratio extends farther azimuthally ($\psi = 215^o$ to $\psi = 325^o$) as well as farther out radially. No negative loading is observed elsewhere on the rotor.

	μ	C_T	θ_0	θ_{1c}	θ_{1s}	β_0	β_{1c}	β_{1s}
Experiment [86]	0.30	0.0065	10.3^o	1.6^o	-5.9^o	2.1^o	0.00^o	0.00^o
Present	0.30	0.0065	8.60^o	1.46^o	-4.68^o	1.53^o	0.00^o	0.00^o

Table 4.8. Comparison between experiment and prediction for case III.

The convergence histories of the trim variables are shown in Figures 4.46 and 4.47. The thrust coefficient, and the lateral and longitudinal flapping coefficients

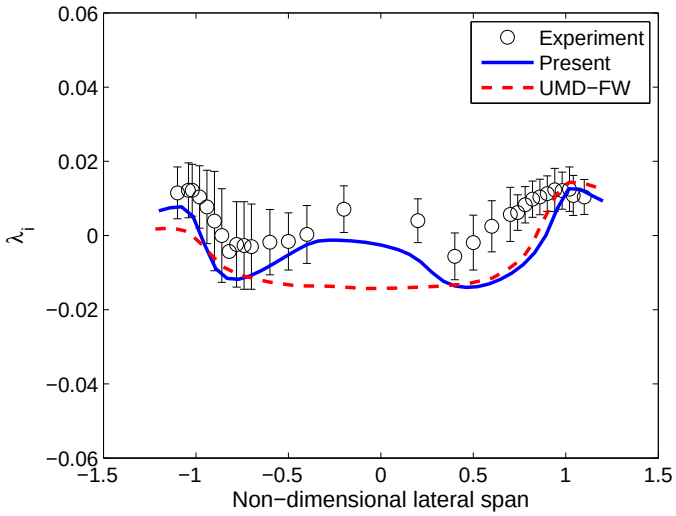

Figure 4.43. Lateral inflow distribution at 1.15c above the TPP ($\mu = 0.30$, $\alpha_{TPP} = -3^o$ and $C_T = 0.0065$).

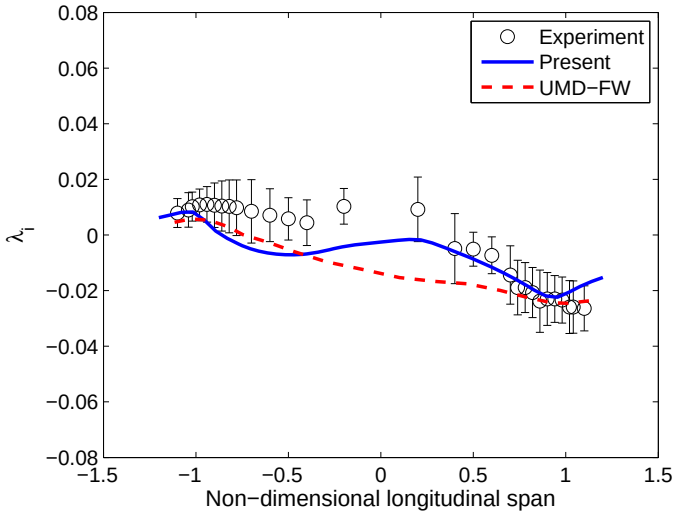

Figure 4.44. Longitudinal inflow distribution at 1.15c above the TPP ($\mu = 0.30$, $\alpha_{TPP} = -3^o$ and $C_T = 0.0065$).

change dramatically between the first and second iterations, after which they change at a slower rate as the coupling proceeds. The corresponding histories of pitch control parameters are shown in Figure 4.48.

The relative difference in induced velocity drops monotonically from about 21% to less than 3% in six coupling iterations as shown in Figure 4.49, with the

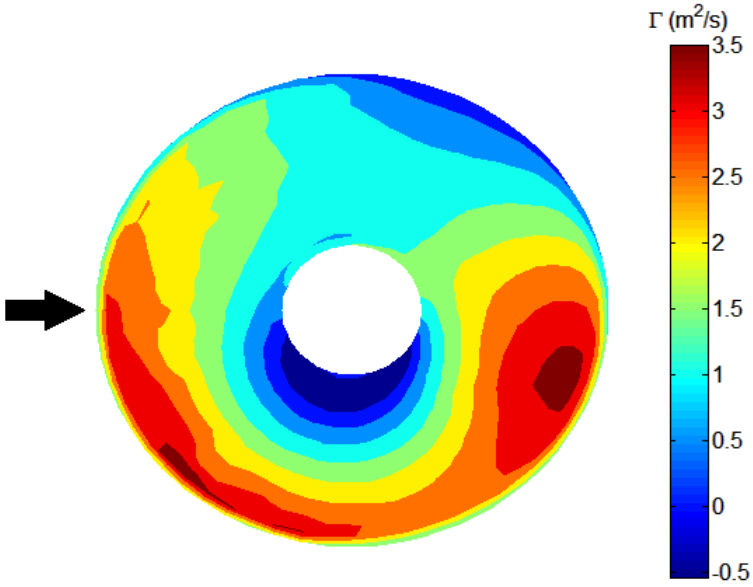

Figure 4.45. Variation of bound circulation with azimuth ($\mu = 0.30$ and $C_T = 0.0065$).

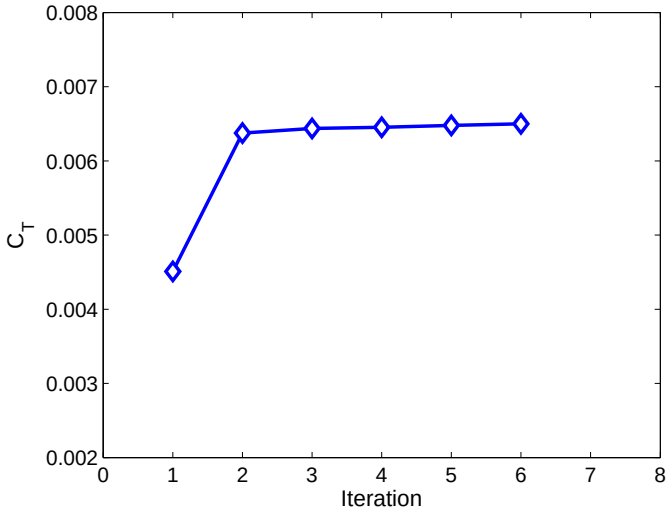

Figure 4.46. Convergence of thrust coefficient ($\mu = 0.30$, $\alpha_{TPP} = -4^o$ and $C_T = 0.0065$).

convergence histories of bound circulation and induced velocity depicted in Figure 4.50.

Figure 4.51 shows the convergence history of the free-wake program during its last run in the coupling solution. The convergence behavior is seen to be similar to the case with $\mu = 0.23$. The L_2-norm decreased from 12% to less than 3% in two

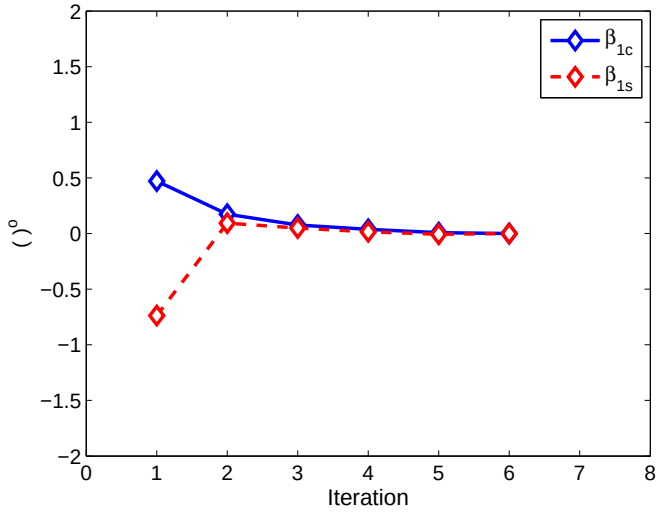

Figure 4.47. Convergence of blade flapping coefficients ($\mu = 0.30$, $\alpha_{TPP} = -4^o$ and $C_T = 0.0065$).

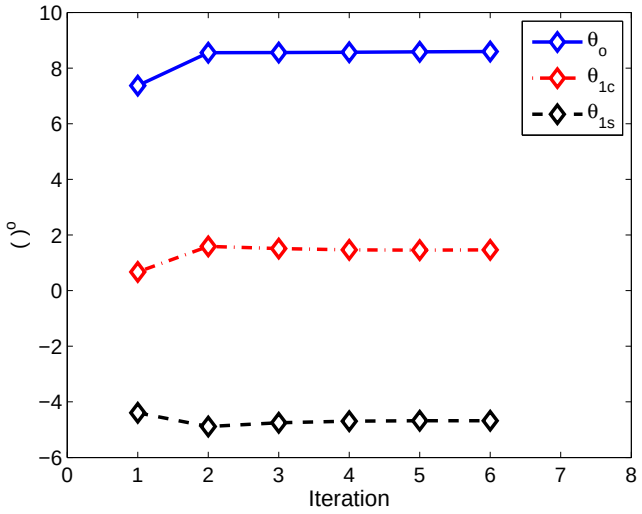

Figure 4.48. Convergence of the pitch control parameters ($\mu = 0.30$, $\alpha_{TPP} = -4^o$ and $C_T = 0.0065$).

rotor revolutions.

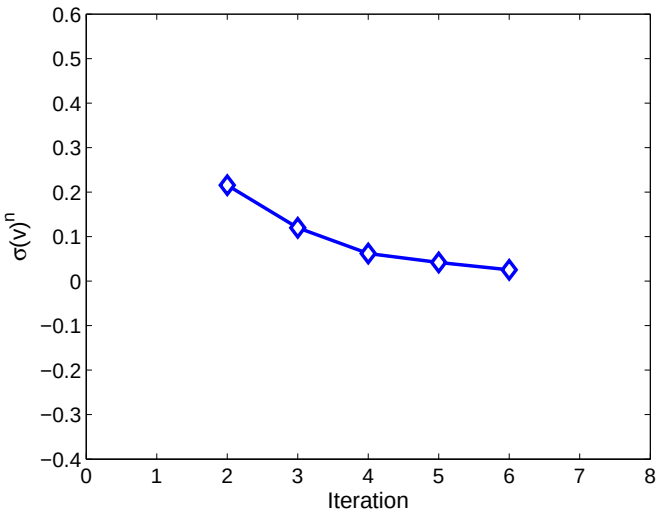

Figure 4.49. Convergence of relative difference in inflow ($\mu = 0.30$, $\alpha_{TPP} = -4^o$ and $C_T = 0.0065$).

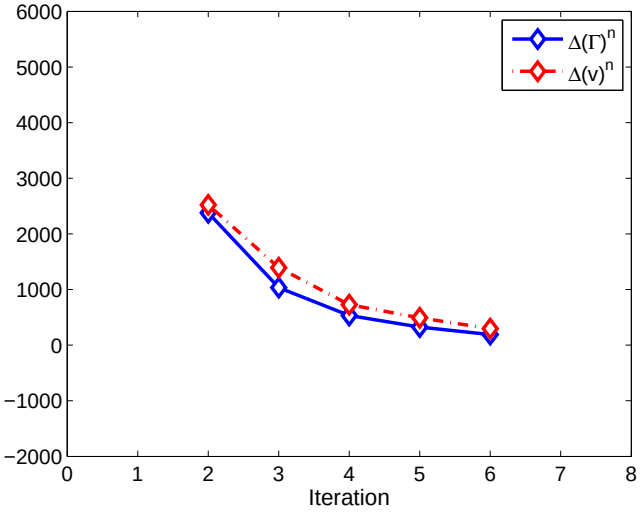

Figure 4.50. Convergence of bound circulation (ft^2/s) and induced velocity (ft/s) ($\mu = 0.30$, $\alpha_{TPP} = -4^o$ and $C_T = 0.0065$).

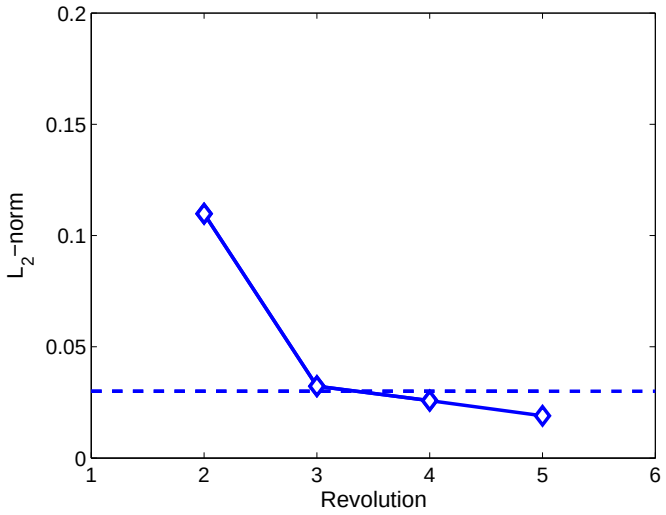

Figure 4.51. Convergence of L_2-norm of induced velocity in the free-wake program. Dashed line represents the user-specified tolerance ($\epsilon = 0.03$).($\mu = 0.30$, $\alpha_{TPP} = -4^o$ and $C_T = 0.0065$).

4.2.2.4 Case IV.

A coupled solution was also performed to validate the numerical calculation against measured data at a higher thrust coefficient. The simulation case with $\mu = 0.23$ discussed earlier was rerun for a $C_T = 0.008$ and the results are presented here. Predicted lateral and longitudinal time-averaged inflow variations are shown in Figures 4.52 and 4.53. The predicted distributions are also compared with test data as well as with predictions using UMD-FW analysis and uniform inflow. The UMD-FW results presented here are taken from Ref. [2]. A few important observations can be made from these results.

The first observation is that the predictions using the free-wake method is in very good agreement with measured data with the predicted results lying within 10% of the experimental mean for lateral inflow distribution over the extent of the rotor disk. Both the present method and UMD-FW over-predict the measured longitudinal inflow distribution between -0.8R and -0.45R. On the rear half of the disk, the present method under-predicts inflow by about 27%, while UMD-FW

over-predicts inflow by about 32%.

Also, compared with UMD-FW predictions, the present free-wake method is able to capture the non-uniform longitudinal and lateral variations of inflow much better inboard of about 70% of the rotor radius. In addition, the comparisons show that using a uniform inflow will lead to large discrepancies in numerical predictions and cannot be used if a high fidelity airloads calculation is desired.

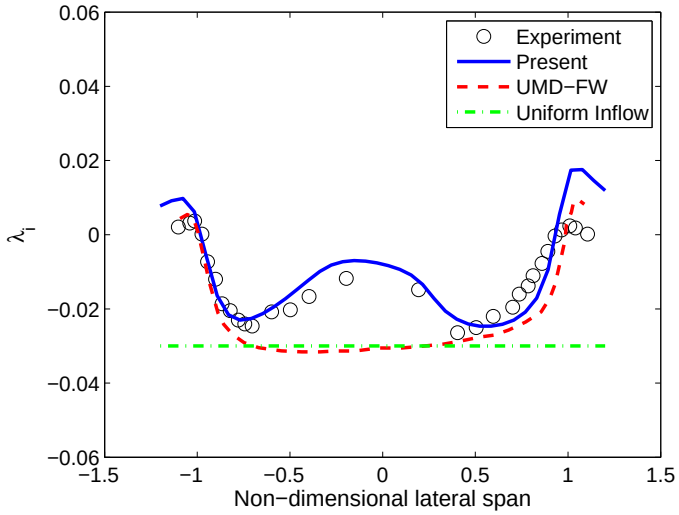

Figure 4.52. Lateral inflow distribution at 1.15c above the TPP ($\mu = 0.23$, $\alpha_{TPP} = -3^o$ and $C_T = 0.008$).

	μ	C_T	θ_0	θ_{1c}	θ_{1s}	β_0	β_{1c}	β_{1s}
Experiment [2]	0.23	0.008	-	-	-	-	0.00^o	0.00^o
Present	0.23	0.008	8.94^o	1.86^o	-3.86^o	1.90^o	0.00^o	0.00^o

Table 4.9. Comparison between experiment and prediction for case IV.

The predicted bound circulation variation is shown in Figure 4.54. The distribution is qualitatively similar to the case with $C_T = 0.0064$ shown in Figure 4.27, with the only significant difference being that the quantitative values are higher for the higher thrust case.

The convergence histories of the trim variables are shown in Figures 4.55 and

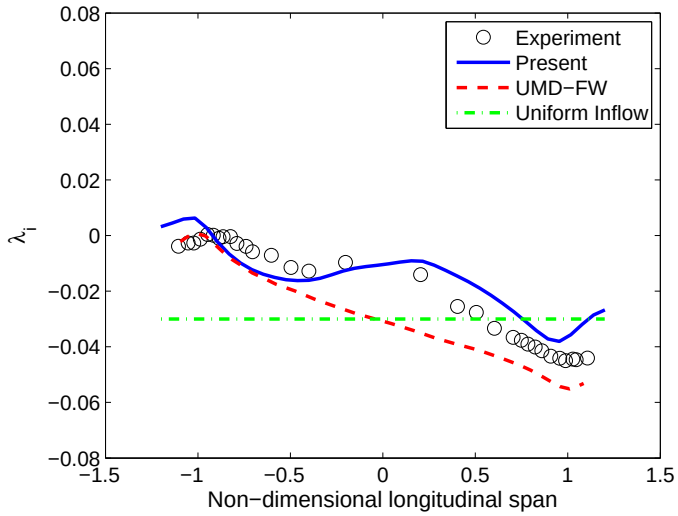

Figure 4.53. Longitudinal inflow distribution at 1.15c above the TPP ($\mu = 0.23$, $\alpha_{TPP} = -3^o$ and $C_T = 0.008$).

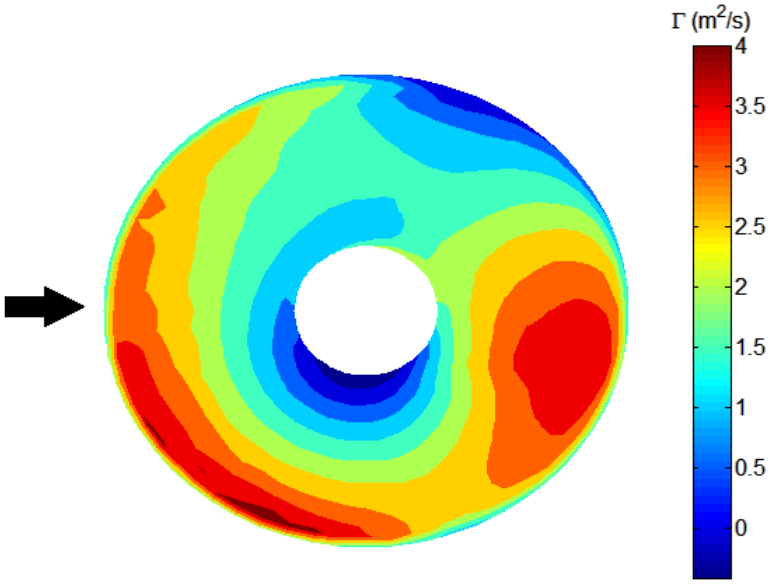

Figure 4.54. Variation of bound circulation with azimuth ($\mu = 0.23$ and $C_T = 0.008$).

4.56. The thrust coefficient, and the lateral and longitudinal flapping coefficients again change dramatically between the first and second iterations, after which they change at a slower rate as the coupled solution proceeds. The corresponding histories of pitch control parameters are shown in Figure 4.57.

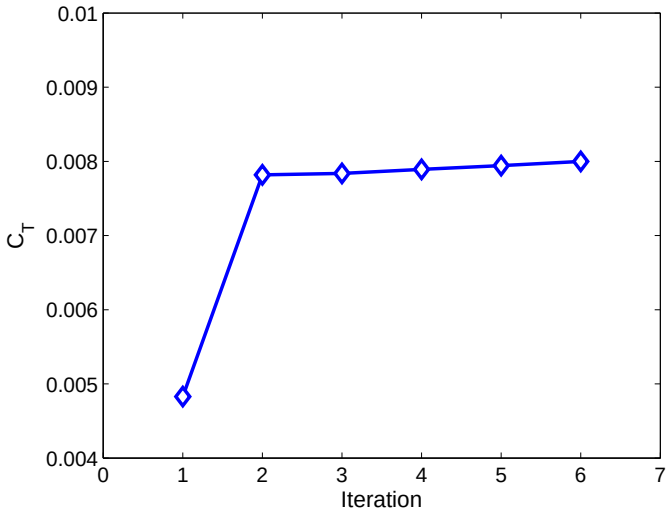

Figure 4.55. Convergence of thrust coefficient ($\mu = 0.23$, $\alpha_{TPP} = -3^o$ and $C_T = 0.008$).

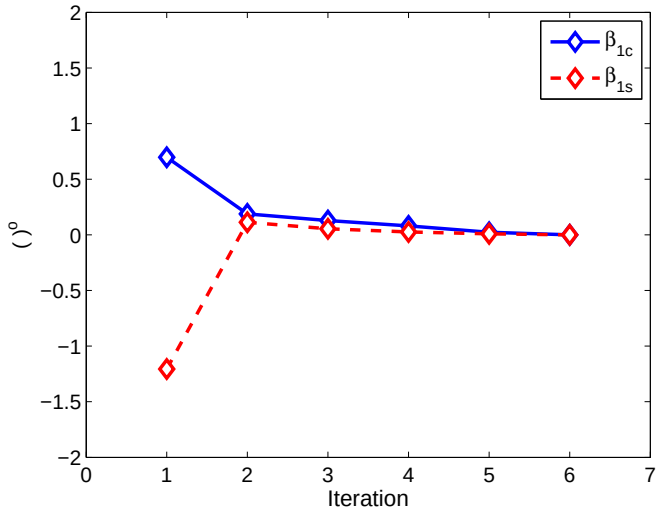

Figure 4.56. Convergence of blade flapping coefficients ($\mu = 0.23$, $\alpha_{TPP} = -3^o$ and $C_T = 0.008$).

The relative difference in induced velocity drops monotonically from about 19% to less than 3% in six coupling iterations as shown in Figure 4.58. The convergence histories of bound circulation and induced velocity are shown in Figure 4.59.

Figure 4.60 shows the convergence history of the final free-wake run for this higher thrust case. It can be observed from the plot that the L_2-norm, which is

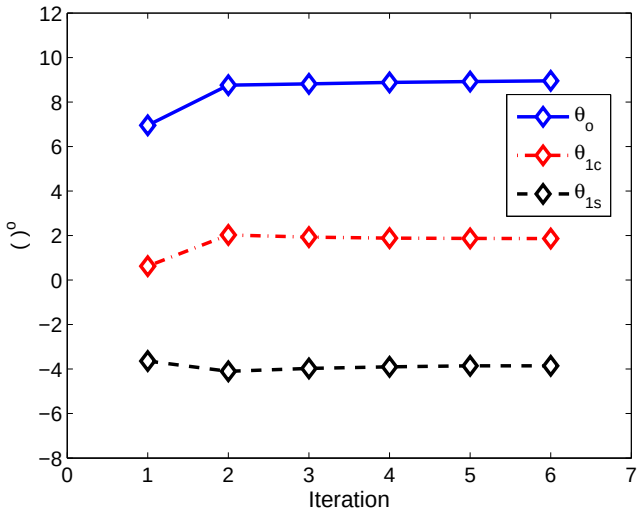

Figure 4.57. Convergence of the pitch control coefficients ($\mu = 0.23$, $\alpha_{TPP} = -3^o$ and $C_T = 0.008$).

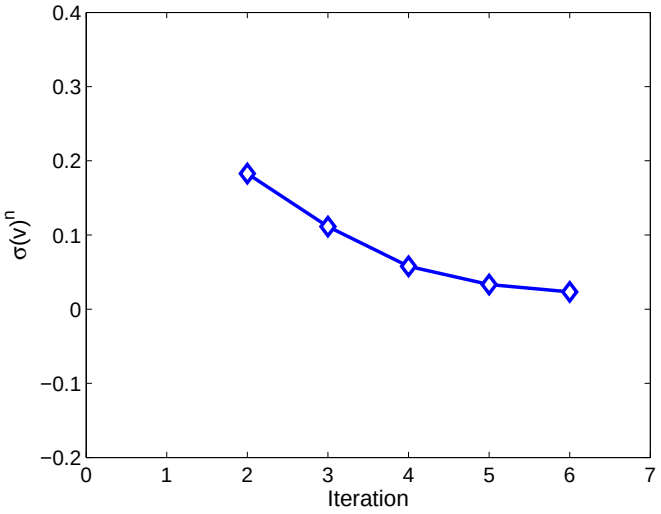

Figure 4.58. Convergence of relative difference in inflow ($\mu = 0.23$, $\alpha_{TPP} = -3^o$ and $C_T = 0.008$).

about 15% at the end of the second revolution, quickly decreases to less than 3% in the next two revolutions.

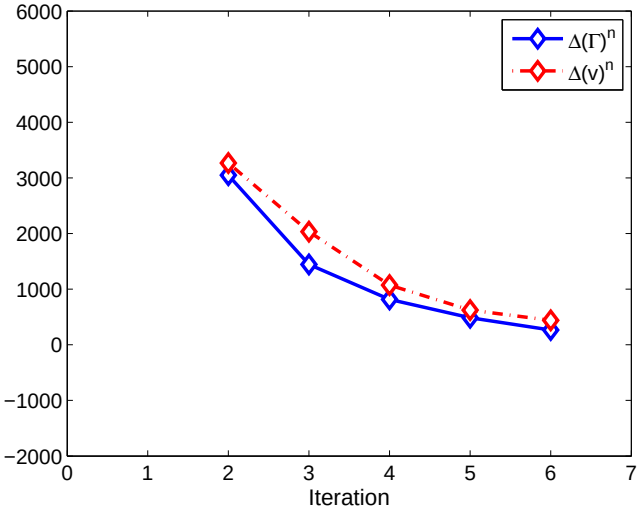

Figure 4.59. Convergence of bound circulation (ft^2/s) and induced velocity (ft/s) ($\mu = 0.23$, $\alpha_{TPP} = -3^o$ and $C_T = 0.008$).

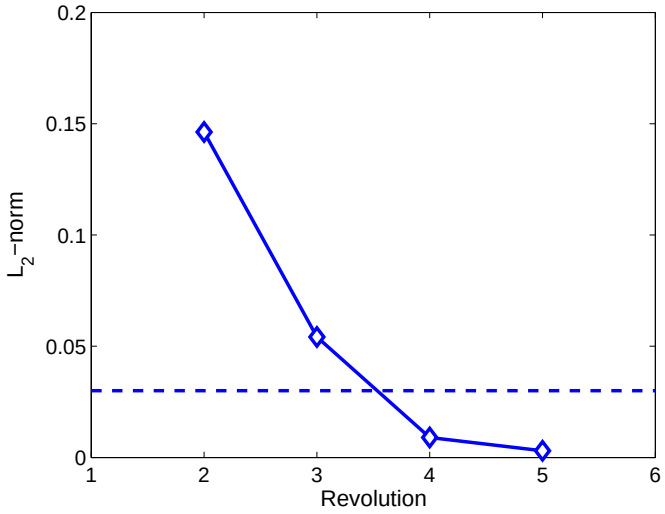

Figure 4.60. Convergence of L_2-norm of induced velocity in the free-wake program. Dashed line represents the user-specified tolerance ($\epsilon = 0.03$).($\mu = 0.23$, $\alpha_{TPP} = -3^o$ and $C_T = 0.008$).

4.2.3 Comparison with Other Analysis Methods

Comparison of the predictions from the a particular method with other existing analysis methods gives one a good idea about where this particular method stands

in terms of accuracy and predictive capability. The same results shown in the last section are again presented here but with predictions from two other currently used analysis methods superimposed on them. The two methods used for comparison are UMD-FW and VTM, the former based on a vortex filament approach with an explicit core model, and the latter based on the solution of the vorticity velocity form of Navier-Stokes equations on a Cartesian grid surrounding the rotor. The UMD-FW results are taken from Ref. [54] and those of VTM are taken from Ref. [87].

Looking at the inflow variations at $\mu = 0.15$, the present free-wake method does an excellent job of matching the lateral inflow distribution not only with the test data, but also with the VTM prediction, as shown in Figure 4.61. Looking at Figure 4.62, the longitudinal inflow distributions computed by the free-wake method and VTM both agree well with the measured data in general with slight under-prediction by both the methods at the rear half of the rotor.

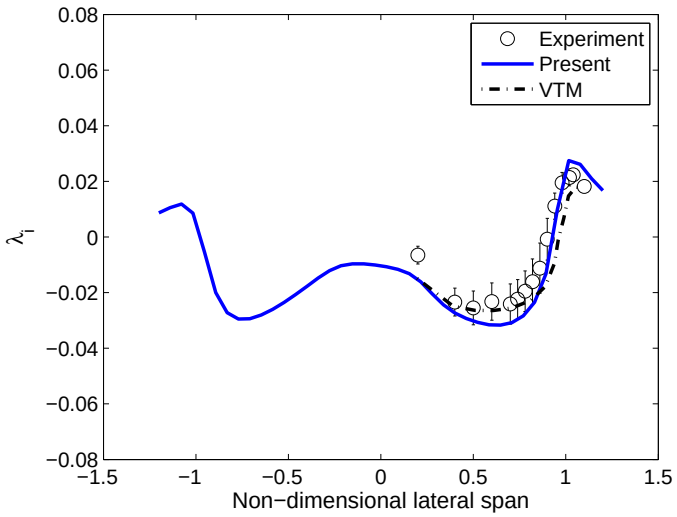

Figure 4.61. Lateral inflow distribution at 1.15c above the TPP ($\mu = 0.15$, $\alpha_{TPP} = -3^o$ and $C_T = 0.0064$).

At $\mu = 0.23$, the present free-wake method, UMD-FW and VTM all do a good job, in general, of agreeing with the measured data, but a few differences

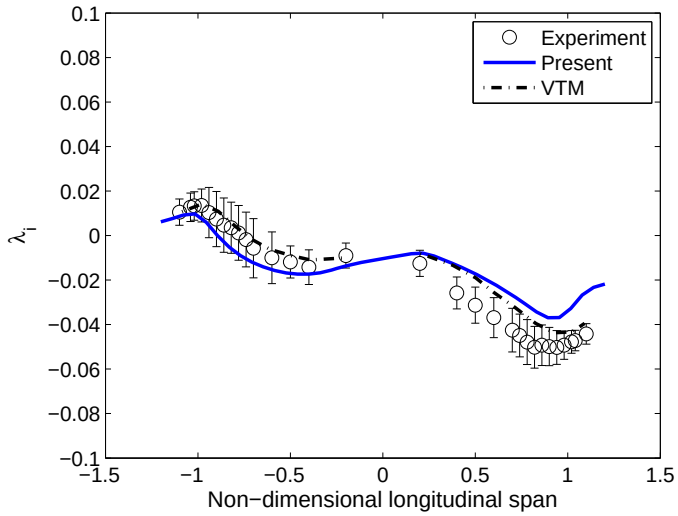

Figure 4.62. Longitudinal inflow distribution at 1.15c above the TPP ($\mu = 0.15$, $\alpha_{TPP} = -3^o$ and $C_T = 0.0064$).

must be noted. In Figure 4.63, VTM and the present free-wake method agree with one another better than either one of them do with UMD-FW. Also, VTM and the present method are able to capture the non-uniformity in inflow with better accuracy. VTM is in better agreement with experimental data compared to the present method and UMD-FW with respect to longitudinal inflow variation. However, the present method does a little better than UMD-FW in capturing the non-uniform variation of inflow.

With regard to comparison at a higher advance ratio of $\mu = 0.30$, all three methods over-predict induced inflow variation in the lateral plane, as shown in Figure 4.65. At least, a part of the reason for this over-prediction in the present analysis could be due to a small relative error between simulation and experiment in the location of the plane on which the inflow was sampled. Nevertheless, the present free-wake method and VTM are, again, able to capture the inflow non-uniformity better than UMD-FW prediction, especially in regions away from the edge of the rotor. The present method over-predicts longitudinal inflow compared to the measured data, as does VTM and UMD-FW, with UMD-FW being unable

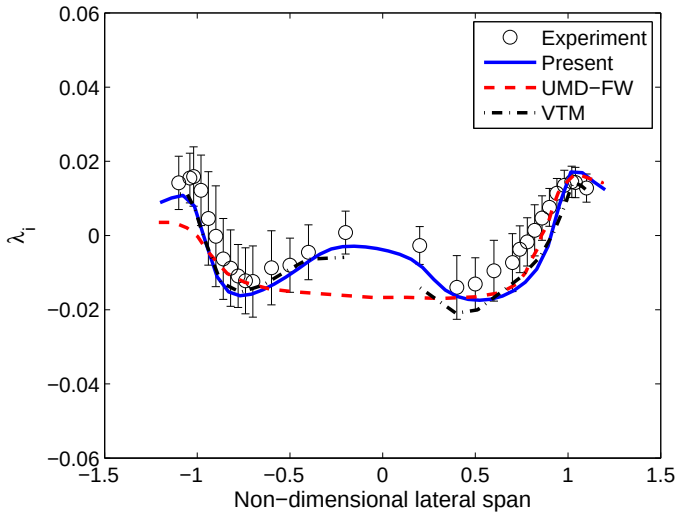

Figure 4.63. Lateral inflow distribution at 1.15c above the TPP ($\mu = 0.23$, $\alpha_{TPP} = -3^o$ and $C_T = 0.0064$).

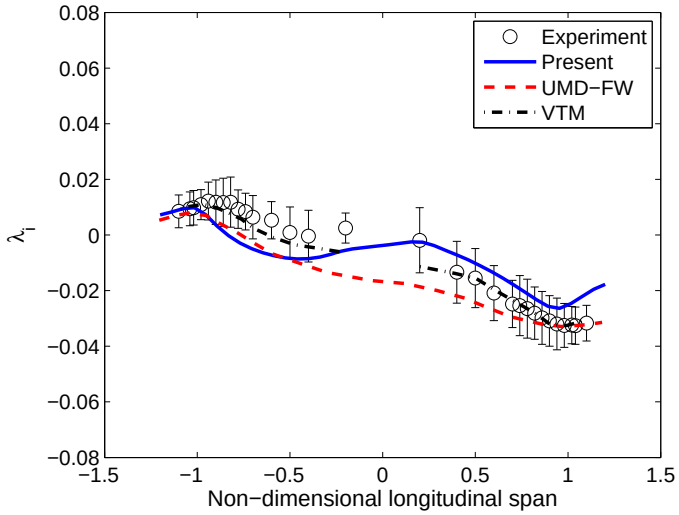

Figure 4.64. Longitudinal inflow distribution at 1.15c above the TPP ($\mu = 0.23$, $\alpha_{TPP} = -3^o$ and $C_T = 0.0064$).

to capture the hump around the center of the rotor.

Based on the three comparison cases discussed here, it appears that, by taking corrective steps in matching the inflow sampling planes, the present free-wake method consistently under-predicts inflow by a small amount in regions aft of the rotor hub. Including a hub model in the analysis, which was not done for any of

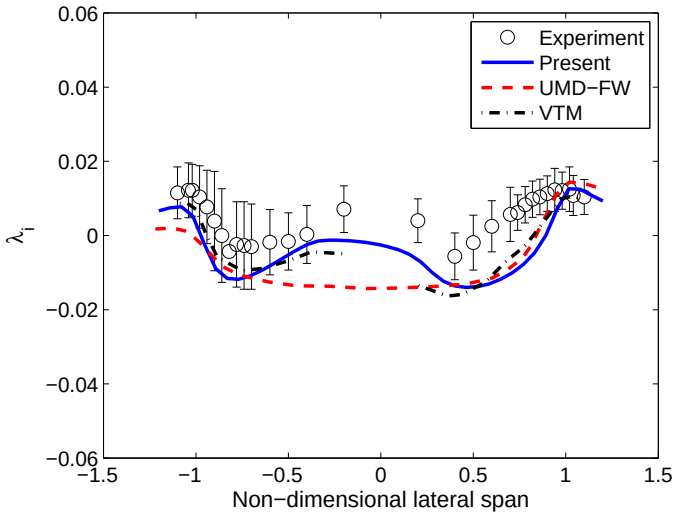

Figure 4.65. Lateral inflow distribution at 1.15c above the TPP ($\mu = 0.30$, $\alpha_{TPP} = -4^o$ and $C_T = 0.0065$).

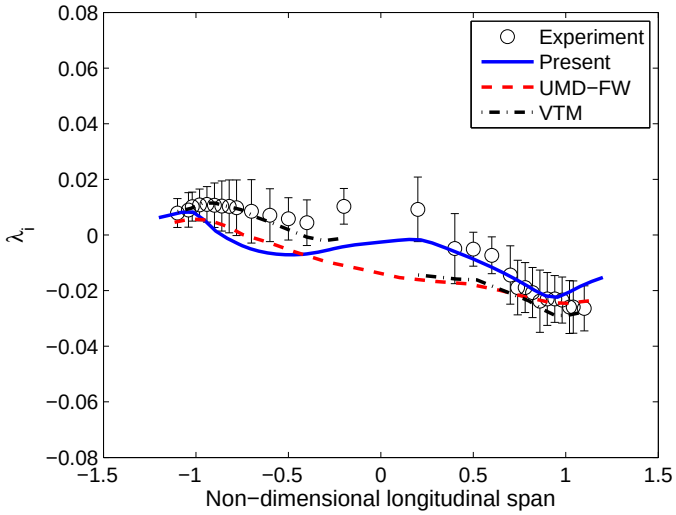

Figure 4.66. Longitudinal inflow distribution at 1.15c above the TPP ($\mu = 0.30$, $\alpha_{TPP} = -4^o$ and $C_T = 0.0065$).

the cases presented here, can probably correct this discrepancy, which is left as a recommendation for future exploration.

4.3 Sensitivity Study

In this section, the effects of two key modeling parameters on the solution fidelity are investigated. The two modeling parameters are blade panel density (number of spanwise distributed vorticity elements representing the blade) and the azimuthal time-step size. Since the induced inflow or downwash is the most significant measure of the effect of the wake on rotor aerodynamics, the downwash distribution across the rotor disk predicted with different modeling parameters is used as the sensitivity criteria here.

4.3.1 Spanwise Panel Density

The effect of changing the number of spanwise distributed vorticity elements representing the blades is studied first. Figure 4.67 shows a comparison of the time-averaged downwash distributions under the rotor for three different panel densities, viz., $N = 15$, 20 and 26. This comparison case is the same as the one presented in section 4.1.3 where the free-wake calculations are run for a prescribed collective pitch of $\theta_o = 11.50^o$. It can be observed that all the computed results have comparable correlations with the measured data, which suggests that the panel density does not have a very significant effect on the simulation fidelity.

The maximum differences in the computed thrust and power coefficients between the three cases lie within 1% and 8% respectively.

N	θ_0	C_T	C_P
15	11.50^o	0.00391	0.000270
20	11.50^o	0.00391	0.000270
26	11.50^o	0.00390	0.000290

Table 4.10. Comparison of predicted variables as a function of number of spanwise distributed vorticity elements (N) for a rotor in hover.

In order to investigate the sensitivity of time-averaged downwash distribution to

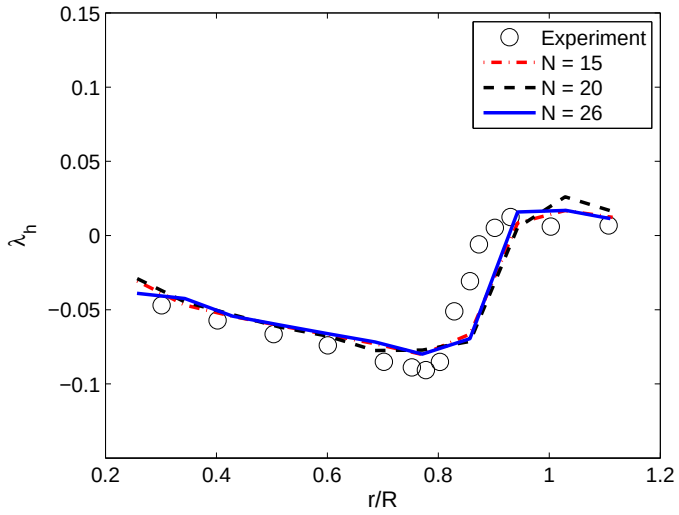

Figure 4.67. Downwash distributions under the rotor disk in hover as a function of number of spanwise distributed vorticity elements (N).

blade panel density in forward flight, the analysis case presented in section 4.2.2.4 for $\mu = 0.23$ and $C_T = 0.008$ is used for comparison. Downwash distributions in both the lateral and longitudinal planes for N =14, 18 and 28 are compared and shown in Figure 4.68 and Figure 4.69. The three panel densities studied here have insignificant influence on the time-averaged downwash distributions which is illustrated by an almost exact overlap of the predicted distributions.

The predicted control and trim variables for the three comparison cases are shown in Table 4.11. It should be noted that the rotor is trimmed to the specified thrust of $C_T = 0.008$ and zero longitudinal and lateral flapping. The maximum percentage variation in any of the control variables (θ_o, θ_{1c} and θ_{1s}) lies within 3% of one another.

The relative insensitivity of the free-wake calculations to blade panel density can be explained by the "higher-order" property of the wake model as explained in section 2.1. Due to the use of a continuous second-order circulation distribution on the lifting line, greater accuracy is achieved with a significantly fewer spanwise elements than would be required by the lifting line method that uses a piecewise

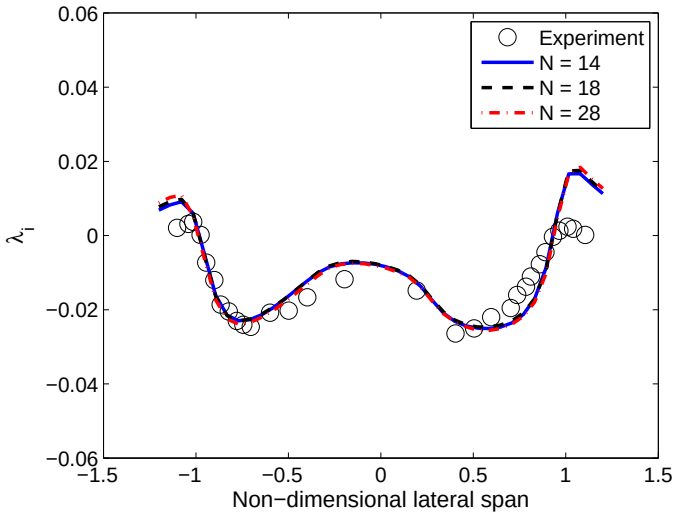

Figure 4.68. Sensitivity of lateral inflow distribution to the number of spanwise distributed vorticity elements (N) in forward flight at $\mu = 0.23$ and $C_T = 0.008$.

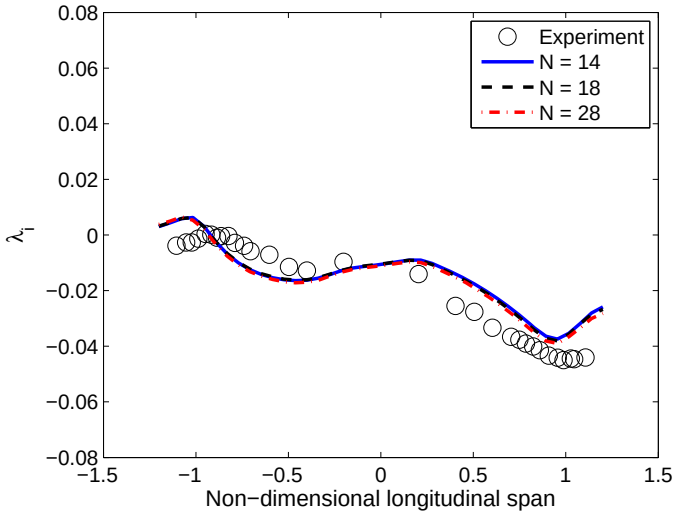

Figure 4.69. Sensitivity of longitudinal inflow distribution to the number of spanwise distributed vorticity elements (N) in forward flight at $\mu = 0.23$ and $C_T = 0.008$.

constant circulation. This allows one to use fewer elements in the spanwise direction, which helps reduce computational time.

N	C_T	θ_0	θ_{1c}	θ_{1s}	β_0	β_{1c}	β_{1s}
14	0.008	8.90^o	1.82^o	-3.80^o	1.90^o	0.00^o	0.00^o
18	0.008	8.95^o	1.86^o	-3.86^o	1.90^o	0.00^o	0.00^o
28	0.008	8.96^o	1.86^o	-3.87^o	1.91^o	0.00^o	0.00^o

Table 4.11. Comparison of thrust and power coefficients as a function of number of spanwise panels (N) for a rotor in forward flight with $\mu = 0.23$ and $C_T = 0.008$.

4.3.2 Time-Step Size

The effect of changing time-step size on the solution fidelity is considered next. The analysis case presented in section 4.1.3 with $N = 26$ is run for different values of time-step size and the results are compared here. Figure 4.70 shows the time-averaged downwash distributions in hover for four different values of azimuthal time-steps, viz., $\Delta\psi = 9^o$, 6^o, 5^o and 3^o. It can be observed that all the computed results have comparable correlations with the measured data. The time-step size has a small, but not significant, influence on the predicted downwash distribution.

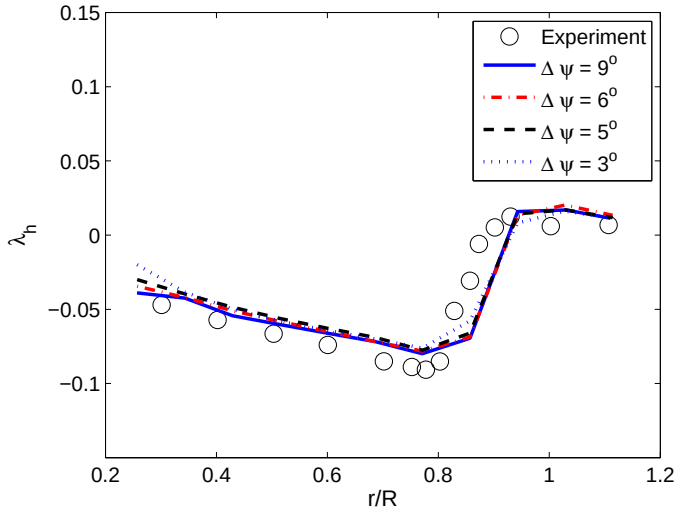

Figure 4.70. Downwash distributions under the rotor disk in hover as a function of azimuthal time-step size ($\Delta\psi$).

The computed thrust and power coefficients for the four cases are summarized in

Table 4.12. The maximum differences in the computed thrust and power coefficients between the four cases lie within 3% and 7% respectively.

$\Delta\psi$	θ_0	C_T	C_P
9^o	11.50^o	0.00389	0.000288
6^o	11.50^o	0.00383	0.000270
5^o	11.50^o	0.00385	0.000270
3^o	11.50^o	0.00380	0.000271

Table 4.12. Comparison of thrust and power coefficients as a function of azimuthal time-step size ($\Delta\psi$) for a rotor in hover.

To investigate the sensitivity of time-averaged downwash distribution to azimuthal time-step size in forward flight, the validation case presented in section 4.2.2.4 for $\mu = 0.23$ and $C_T = 0.008$ with $N = 18$ is used. Downwash distributions in both the lateral and longitudinal planes for $\Delta\psi = 6$, 5 and 3 are compared and shown in Figure 4.71 and Figure 4.72. The three different time-step sizes considered here have little influence on the time-averaged downwash distribution as demonstrated by an almost exact overlap of the predicted distributions except for a small difference at the rear of the rotor disk.

The maximum percentage variations in the predicted control variables lie within 1% for θ_o and θ_{1s}, and within 3% for θ_{1c}.

$\Delta\psi$	C_T	θ_0	θ_{1c}	θ_{1s}	β_0	β_{1c}	β_{1s}
6^o	0.008	8.95^o	1.86^o	-3.86^o	1.91^o	0.00^o	0.00^o
5^o	0.008	8.96^o	1.89^o	-3.88^o	1.90^o	0.00^o	0.00^o
3^o	0.008	8.93^o	1.90^o	-3.85^o	1.90^o	0.00^o	0.00^o

Table 4.13. Comparison of control and trim variables as a function of time-step size ($\Delta\psi$) for a rotor in forward flight with $\mu = 0.23$ and $C_T = 0.008$.

Explicit-type free-wake methods are known to exhibit numerical problems with small time-steps [88]. Since certain rotor analysis problems such as rotor/airframe interaction and rotor acoustics require a high-resolution free-wake method, these

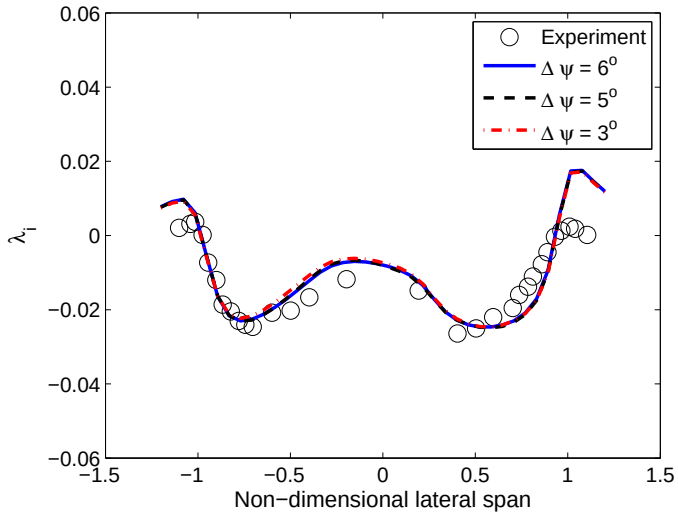

Figure 4.71. Sensitivity of lateral downwash distribution to azimuthal time-step size ($\Delta\psi$) in forward flight at $\mu = 0.23$ and $C_T = 0.008$.

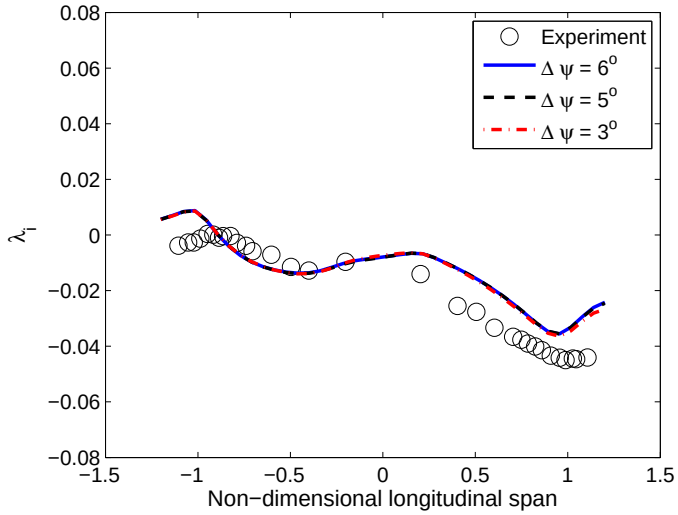

Figure 4.72. Sensitivity of longitudinal downwash distribution to azimuthal time-step size ($\Delta\psi$) in forward flight at $\mu = 0.23$ and $C_T = 0.008$.

methods cannot be used for such problems. With that said, the results presented here demonstrate that the higher-order, free-wake method is able to run without encountering any numerical instability for a time-step size as low as 3^o as shown by the monotonic convergence of the L_2-norm of induced velocity field in Figure 4.73. It should be noted that multiple-blade phasing is activated after the second rotor

revolution which explains the steep drop in L_2-norm going from the second to the third rotor revolution. The wake geometry corresponding to this case is shown in Figure 4.74.

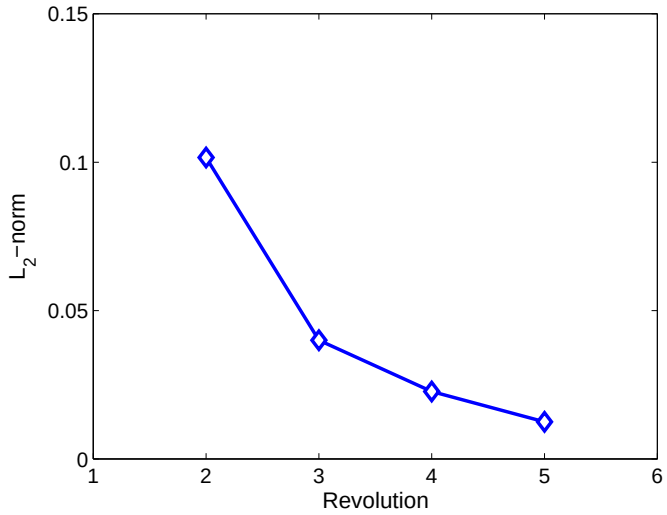

Figure 4.73. L_2-norm convergence in the free-wake calculation for azimuthal time-step size of $\Delta\psi = 3^o(\mu = 0.23$ and $C_T = 0.008)$.

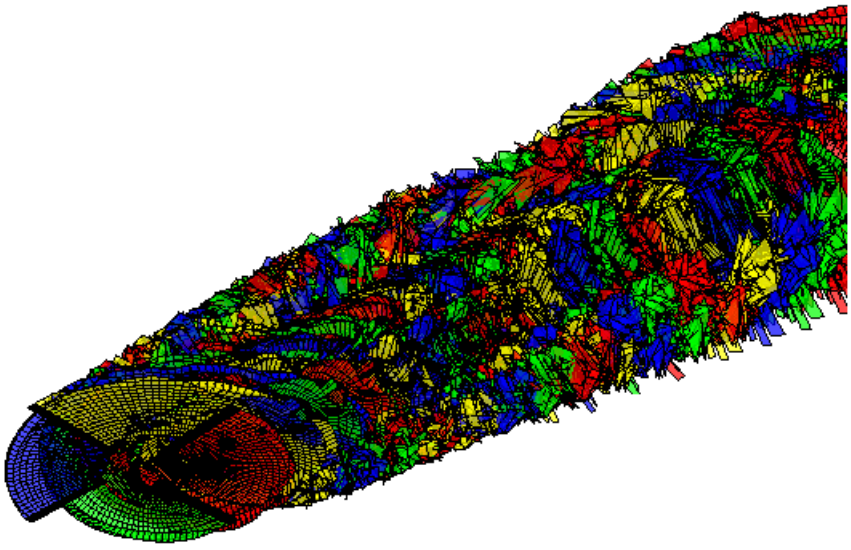

Figure 4.74. Wake geometry for azimuthal time-step size of $\Delta\psi = 3^o(\mu = 0.23$ and $C_T = 0.008)$.

4.4 On-Blade Devices

On-blade aerodynamic control using partial-span devices is becoming increasingly attractive for various end goals including aerodynamic performance enhancement, vibration reduction, and acoustic noise control. An example of a successful implementation of active on-blade concepts is the Boeing Smart Material Actuated Rotor Technology (SMART) rotor, a full-scale MD900 bearingless rotor system with active flaps as shown in Figure 4.75 [21]. It becomes a modeling requirement for a free-wake analysis to account for the influence of such on-blade devices on the wake geometry and hence the induced velocity field which has a strong influence the blade airloads. The higher-order, free-wake method introduced in this work is able to capture the influence of such devices. As an illustration, a free-wake hover analysis with and without a partial-span deflection (deflection being constant around the azimuth) is performed for the rotor presented in section 4.1.3 where the blades use an NACA 0015 airfoil.

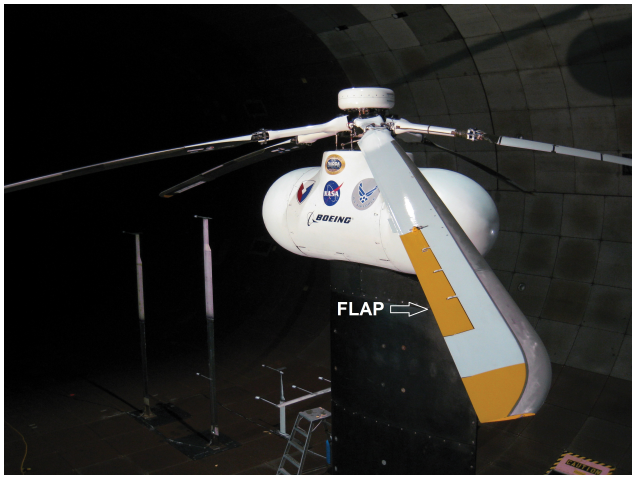

Figure 4.75. SMART rotor with an active flap in a NASA wind tunnel [21].

The blade planform is shown in Figure 4.76 and is modeled with 26 distributed vorticity elements with panel density increasing towards both the root and the tip of blade. The partial-span device spans from 75% to 90% of the blade radius

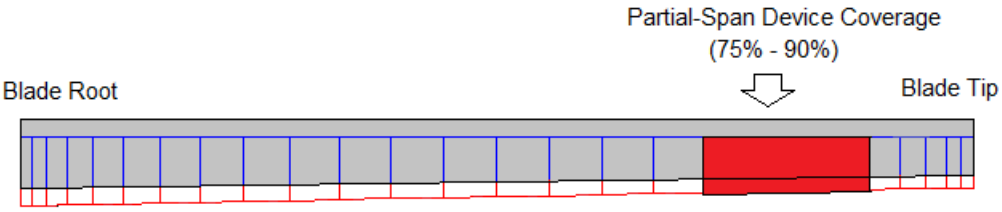

Figure 4.76. Schematic of the blade showing the partial-span device location. The shaded portion represents the physical blade while the gridded panels represent the distributed vorticity elements used to model the blade.

	C_T	C_P
Baseline (No Partial-Span Deflection)	0.00396	0.000269
With Partial-Span Deflection	0.00443	0.000331
Percent Change	11.87%	23.05%

Table 4.14. Change in thrust and power coefficients due to the partial-span deflection at a blade collective pitch of $\theta_o = 11.50^o$

and is simulated in the analysis by providing a constant increment of pitch by the amount of the desired deflection. The partial-span device is modeled by 4 distributed vorticity elements.

Simulations were performed for both the baseline case and the case with partial-span deflection at the same prescribed collective pitch of 11.50^o. Table 4.14 shows the thrust and power coefficients from the two analyses. The baseline case results in $C_T = 0.00396$ while the case with a partial-span deflection of 4^o results in $C_T = 0.00443$, resulting in an increase in thrust by 11.87%.

The increase in thrust is of course due to the local increase in geometric pitch at the device location. The resulting increase in local blade loading is shown in Figure 4.77 where spanwise lift coefficient distributions are compared for the two cases.

At the same time, the partial-span deflection causes the power to increase by 23.05%. This is expected because the increase in geometric pitch at the location of the device, while increasing the local lift, also increases the local drag as shown in Figure 4.78. This increase in drag causes the power to increase by requiring more

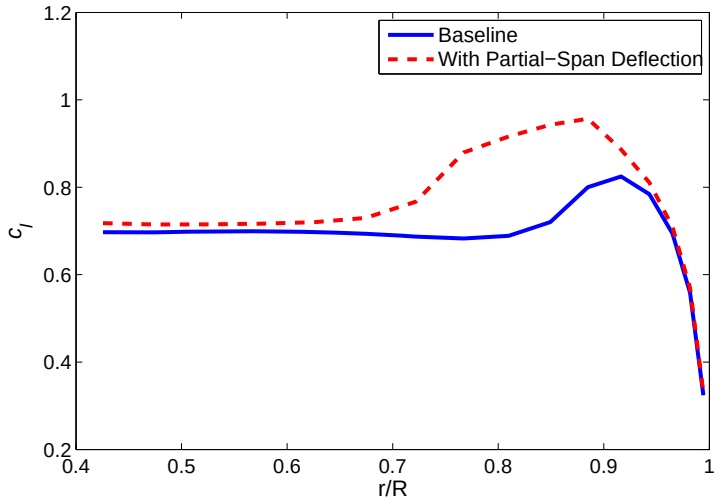

Figure 4.77. Change in time-averaged, spanwise distribution of lift coefficient due to a partial-span deflection of 4^o.

torque to be generated to rotate the blades against profile and induced drags.

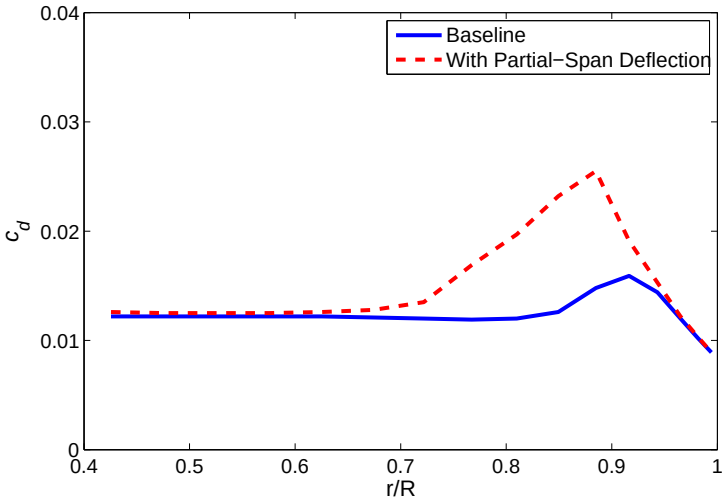

Figure 4.78. Change in time-averaged, spanwise distribution of drag coefficient due to a partial-span deflection of 4^o.

Figure 4.79 shows close-up views of the wake geometries. It can be observed that the partial-span deflection causes a local distortion of the wake geometry in the vicinity of the span location of the device. The partial-span deflection along with the local wake distortion have the effect of the modifying the local induced

velocity field in terms of both magnitude and radial distribution. Comparison of time-averaged, downwash distributions at a vertical distance of $z = 0.10R$ below the rotor disk for the two cases are shown in Figure 4.80. The increased downwash in the vicinity of the radial location of the device is caused by a combination of the increased strength of the local vorticity and the locally distorted configuration of the wake sheet.

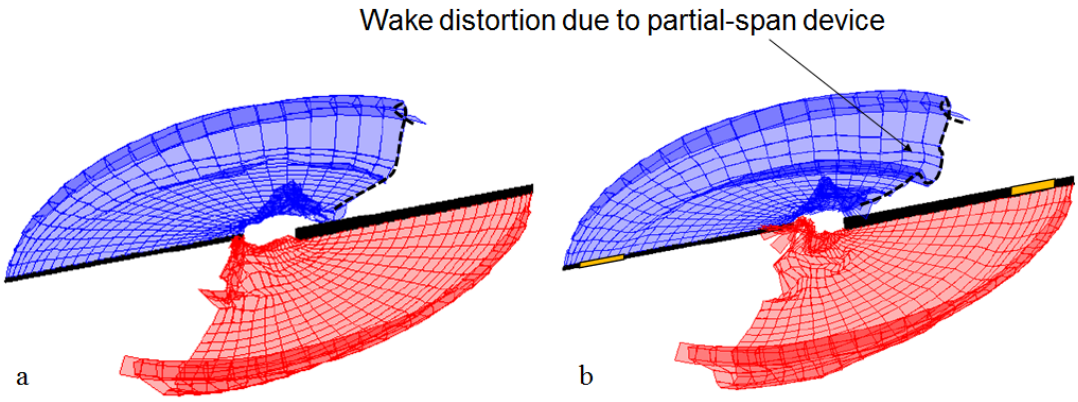

Figure 4.79. Comparison of the wake geometries of: (a) Baseline rotor without partial-span deflection, (b) Rotor with a partial-span deflection of 4^o. The partial-span device spans from 75% to 90% of the rotor radius.

These preliminary results demonstrate the capability of the current free-wake analysis in capturing the effect of on-blade, partial-span, devices. In contrast, traditional filament-based, free-wake analyses which usually make use of a single distorted tip filament with an undistorted near-wake inboard sheet can completely miss the wake physics that is demonstrated here with this new free-wake analysis, making the latter an attractive choice for future rotorcraft analysis.

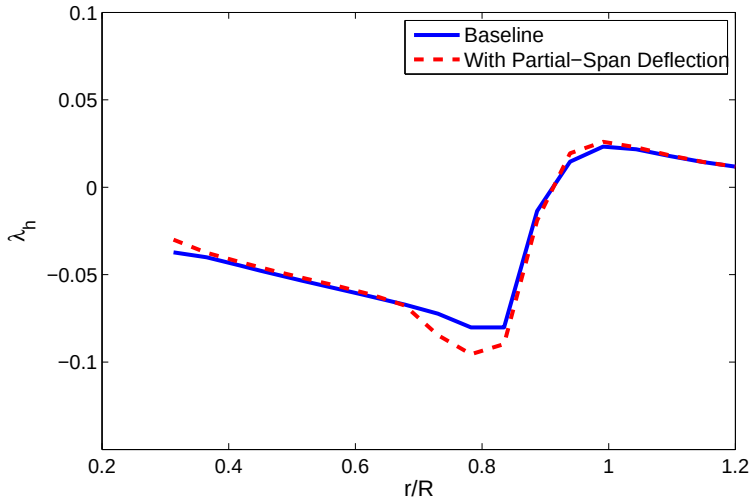

Figure 4.80. Change in time-averaged downwash distribution under the rotor due to a partial-span deflection of 4^o.

4.5 Computational Efficiency

All of the free-wake calculations presented in this work were performed on a single computer processor. Although computational efficiency of the analyses presented in this work would improve greatly with parallel processing, no attempt has been made towards that end at the time this dissertation was completed. Effort was, instead, focused on developing the methodology and performing initial validation of the model to develop confidence in terms of its predictive capability. The computational efficiency of the method is discussed briefly here.

The hover analysis of section 4.1.1required 35,383 seconds, or 9.82 hours, on a single processor of Aerospace Engineering computer cluster comprising of Intel Xeon(E5430) processors.The 2-bladed rotor is spun at a speed of 1250 RPM with the blades collectively pitched at 8^o. In the model, the blades are discretized spanwise into 1 row of 22 distributed vorticity elements. Three time step intervals are used. Interval 1, which covers the beginning of the simulation, consists of a total of 120 time steps with 24 time steps per revolution. Interval 2, which smoothly

connects interval 1 and 3, consists of 24 time steps. Lastly, interval 3 comprises 200 time steps with a finer resolution of 40 time steps per revolution. This results in a total of 344 time steps for the entire calculation constituting a total of 11 rotor revolutions. The total number of distributed vorticity elements involved in this simulation can be obtained by multiplying the total time steps by the number of spanwise elements and the number of blades, which results in 15, 136 elements.

As a qualitative comparison, consider the full domain CFD analysis of an S-76 rotor performed by Narducci [10] of Boeing Company. The calculations were performed using 240 cores of a high performance Linux cluster which took about 117 hrs of CPU time. The solution domain in the analysis contained 63.4 million grid points. To the best knowledge of this author, the details of the computational efficiency of the viscous vortex particle simulation, which is discussed and used for comparison with some of the results in this dissertation, is not published in open literature. However, it is mentioned in Ref. [11] that the viscous vortex particle simulation requires a large number of particles and constitutes an $\mathcal{O}(N^2)$ problem, with N being the number of particles, which is computationally expensive to evaluate. To reduce computational time, He and Zhao [11] uses a combination of summation techniques such as the TreeCode method [89] and fast multipole method (FMM) [90] in their implementation of viscous vortex particle method.

In the coupled RCAS-Free-Wake calculations, the solution time depends almost entirely on the number of coupling iterations required until convergence. As an illustration, the final free-wake run from the coupled solution presented in section 4.2.2 is considered here. The solution converged after 5 revolutions with each revolution discretized into 60 time steps. "Multiple blade phasing," which was discussed in section 3.2.3, is activated after the second rotor revolution. This solution required 27,697 seconds, or 7.69 hours, on a single processor of the Aerospace Engineering computer cluster comprising of Intel Xeon(E5430) processors. The rotor has 4 blades with the blades being discretized into 18 distributed vorticity

elements.The advance ratio and thrust coefficient associated with this run are 0.23 and 0.008 respectively.

To increase computational efficiency and further increase the attractiveness of the free-wake method over existing singularity-based, free-wake methods, such as the ones used in RCAS, it is strongly recommended that the method take advantage of parallel computing infrastructures.

Chapter 5
Conclusions and Future Work

Potential-flow-based, free-wake methods are currently the most popular choice for a fast yet high-fidelity analysis employed in most comprehensive rotorcraft analysis programs. However, these methods rely on empirical parameters such as vortex core size and are often limited to a single relaxed tip filament with the inboard wake details either neglected or approximated with a simplified model. Also, inclusion of more filaments in the wake can lead to numerical instability or, with the help of smoothing parameters, result in solutions that are, arguably, tuned for a particular problem.

In this thesis, a new higher-order, free-wake method for rotorcraft analysis was presented as an answer to the limitations highlighted above. This method uses elements of distributed vorticity to model the lifting surfaces and the wake. Spanwise arrays consisting of such elements are placed along the zero-lift plane to model the rotor blades. Using a time-stepping procedure, the spanwise vorticity elements placed along the blade trailing edge are released into the wake as the blades rotate and translate. These wake elements are then displaced with the local flow field to achieve a force-free, relaxed wake. The main advantages of this method are its singularity-free implementation and a continuous higher-order blade loading with an associated continuous full-span wake vorticity representation. This method has been applied to the analysis of fixed wings as well as wind turbines in the past

and has shown excellent promise in terms of its predictive capability.

This work demonstrated the capability of the new free-wake method in predicting the challenging aerodynamics of helicopter rotors in both hover and forward flight through extensive correlation studies. In hovering flight, the blade spanwise lift coefficients predicted by the free-wake method correlated well with the data from the model rotor experiment conducted by Caradonna and Tung. A fairly good comparison of the predicted results against measured data from the experiments conducted by Knight and Hefner demonstrated the ability of the method in predicting the figure of merit despite that fact that the model is only based on potential-flow theory. Rotor downwash, which is one of the most important considerations in rotor aerodynamic analysis, is predicted very well by the free-wake method when compared to measured data from a hover experiment involving a full-scale helicopter rotor. The free-wake method captures the basic characteristics of the rotor wake, such as the wake contraction without the use of any empirical modeling parameters. Some of the results were also compared with predictions using higher-fidelity methods such as the viscous vortex particle method (VVPM), which showed that the free-wake method did almost equally well in terms of correlating with experimental data.

Comparison of numerical predictions with experimental data in forward flight requires the rotor to be trimmed to the conditions recorded in the experiment. To ensure this, the free-wake program was coupled with RCAS, a comprehensive helicopter analysis code developed by the US Army, in order to take advantage of its robust trim algorithm, among other capabilities. The coupling was achieved through what is called a "loose-coupling methodology", whereby data is exchanged at the end of each coupling iteration or "converged" rotor revolution. The downwash distributions predicted by the present method were compared to the measured data for a model rotor at various advanced ratios and thrust levels taken at the U.S. Army/NASA Langley Research Center (LaRC) facility. The free-wake method was

not only shown to capture the important phenomena observed in the experiments but its predictions also correlated well with the experimental data both in terms of magnitude and distribution with some exceptions at the highest advance ratio, where other existing methods are also seen to do poorly.The predictions from the free-wake analysis were also compared to predictions by other existing methods such as the University of Maryland free-wake method (UMD-FW) and the vortex transport method (VTM). The present method was shown to yield results comparable to the ones obtained using VTM, both of which correlated better with measurements than did UMD-FW.

Sensitivity studies showed that the blade panel density and azimuthal time-step size do not have a significant influence on the solution fidelity. In addition, free-wake analyses with the azimuthal time-step size of $\Delta\psi = 3^o$ demonstrated the robustness of the method even with a small time-step size, which is important for certain problems including rotor acoustics.

A preliminary discussion was also presented regarding the capability of the new free-wake method in resolving on-blade, partial-span devices. An analysis of a 2-bladed rotor with a partial-span deflection was performed and the resulting changes in sectional loadings, downwash distribution, wake geometry and aggregate performance parameters were highlighted to demonstrate its potential as a tool for future rotorcraft analysis.

In short, the new free-wake method for helicopter rotor analysis presented in this work shows very good promise in terms of its predictive capability with an advantage over the current singularity-based, free-wake methods that essentially no explicit user-specified smoothing parameter such as the vortex core size is required. The method is far more efficient than those based on the solution of Navier-Stokes equation on Eulerian grids, and hence is well-suited for preliminary design studies. With that said, there are aspects of this method that need further improvement.

With respect to the implementation of the basic model, it was mentioned that

using a non-uniform rather than uniform paneling might cause numerical issues. This is recognized to be a result of unbalanced singularity that is used in the numerical implementation when discretizing the continuous wake. Hence, from experience, using a uniform paneling is recommended. But a method could possibly be devised whereby the singularity constant (k) used for a particular spanwise element can be a function of the paneling distribution rather than a constant that is currently used for all the elements inboard of the ones at the tips. Another area that could benefit from a future study is the effect of changing the aspect ratio of the distributed vorticity element. Potential singularity-based methods are in general sensitive to the shape and configuration of the elements used vis-a-vis the position of the collocation points. The method introduced in this work is most probably not devoid of such issues and this would be interesting to explore.

In hover analysis, a problem related to wake convection was discussed in this thesis. In the simulations, the wake sheets were observed to not only pile up but also shoot up significantly around the center of the rotor in the absence of any initial artificial downward convection velocity. Increasing the paneling density near the blade root coupled with a user-specified initial convection velocity improved the situation in the solutions presented in this thesis, but further studies should be conducted to ascertain if at least a part of the reason for the observation has to do with the basic implementation of the model.

In the RCAS-free-wake coupling implemented in this work, the blade paneling in RCAS must match the paneling in the free-wake program. This was done to simplify the bound circulation matching procedure, but it should not be difficult to modify the program to have different paneling distributions. Also, the induced velocity tolerance used in the coupled solution was chosen as a compromise between reducing simulation time, recommendation from ART, and solution accuracy. It would be interesting to study the consequences of further reducing the tolerance when a way to speed up the free-wake solution is developed in the future.

The last recommendation concerns the computational efficiency of the free-wake program. The free-wake analysis introduced in this thesis is no doubt more efficient than CFD methods but it is computationally more expensive compared to traditional free-wake analyses that use a single relaxed tip filament per blade. This is of course due to a wake model that consists of elements that extend throughout the length of the blade. This results in a considerable increase in the number of velocity computation points in the wake. Two suggestions are in order for reducing the computational costs. First, the method would benefit greatly from parallel processing, as a large part of the solution time is spent solving the influence of the wake elements on one another, which can be set up as parallel processes with limited overhead. Another method that will reduce solution time is to merge the wake elements into a single filament, with the appropriate strength, after a certain wake age.

Appendix A
A Note on Paneling Distribution

The RCAS-free-wake coupled simulations for forward flight presented in thesis were performed using distributed vorticity elements of equal span along the length of the blade. The choice of a uniform rather than non-uniform paneling (with the span decreasing toward the blade tips) was motivated by a recognition that a non-uniform paneling of the elements results in unbalanced singularity cancellation between adjacent elements. Illustration of this problem is the subject of this appendix.

As described in section 2.2, the normal component of the velocity induced by the vortex sheet element is proportional to a logarithmic term as shown in Eq. (A.1) below.

$$w_2(\eta) \sim \ln\left[\frac{(\eta-\eta_i)^2}{(\eta+\eta_i)^2}\right] \tag{A.1}$$

In the numerical implementation, a constant k is added to both the numerator and the denominator of the term inside the logarithm to prevent numerical singularities at the edges of the sheet elements, resulting in

$$w_2(\eta) \sim \ln\left[\frac{k+(\eta-\eta_i)^2}{k+(\eta+\eta_i)^2}\right] \tag{A.2}$$

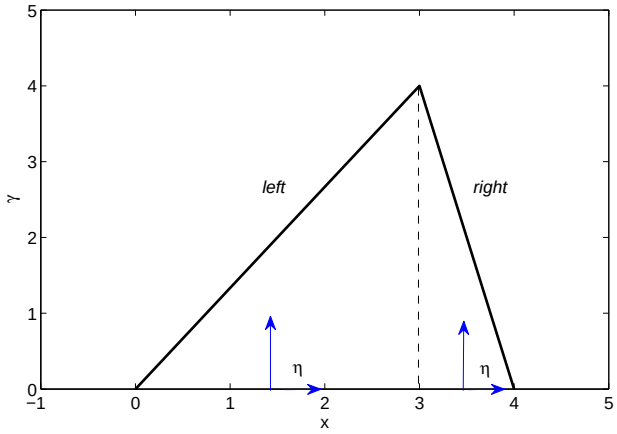

Figure A.1. Distributed vorticity elements with unequal spans.

Two scenarios are now considered. The first scenario has two spanwise vortex sheets with unequal span lengths. The half span of the left element is $\eta_i = 1.5$ and that of the right element is $\eta_i = 0.5$, as shown in Figure A.1. It should be noted that η is measured from a local coordinate system fixed to the element mid-span location. The normal induced velocities due to the left and the right elements at their shared edges are

$$w_2(1.5)_{left} \sim \ln\left[\frac{k + (1.5 - 1.5)^2}{k + (1.5 + 1.5)^2}\right] \tag{A.3}$$

and

$$w_2(-0.5)_{right} \sim \ln\left[\frac{k + (-0.5 - 0.5)^2}{k + (-0.5 + 0.5)^2}\right] \tag{A.4}$$

respectively.

If $k = 0$, which results in the original form described by Eq. (A.1), the velocity contributions reduce to

$$w_2(1.5)_{left} \sim \ln 0 \sim -\infty \tag{A.5}$$

and

$$w_2(-0.5)_{right} \sim \ln \infty \sim +\infty \tag{A.6}$$

which cancel out analytically, however, computers cannot handle such infinities, which is exactly the motivation behind the singularity treatment used in this model.

If $k = 0.5$, for example, the induced velocities evaluate to

$$w_2(1.5)_{left} \sim -2.944 \tag{A.7}$$

and

$$w_2(-0.5)_{right} \sim 1.0986 \tag{A.8}$$

which do not exactly cancel one another.

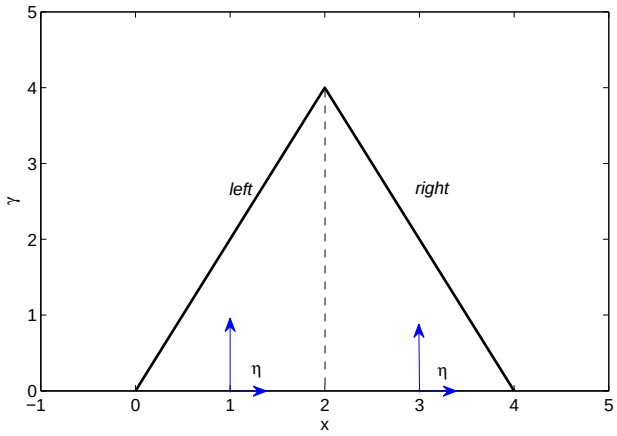

Figure A.2. Distributed vorticity elements with equal spans.

Now consider a scenario in which the elements have equal spans with $\eta_i = 1$ as shown in Figure A.2. The velocity components in this case simplify to

$$w_2(1)_{left} \sim \ln\left[\frac{k + (1-1)^2}{k + (1+1)^2}\right] \sim \ln\left[\frac{k}{k+1}\right] \tag{A.9}$$

and

$$w_2(-1)_{right} \sim \ln\left[\frac{k+(-1-1)^2}{k+(-1+1)^2}\right] \sim \ln\left[\frac{k+1}{k}\right] \tag{A.10}$$

It can be clearly seen that, with uniform spans, the velocities cancel one another regardless of the value of k.

Appendix B
RCAS Trim Analysis

In general, a helicopter trim solution involves determining the blade control settings, rotor disk orientation, and overall helicopter orientation for a prescribed flight condition. The adjustment of forces and moments about all the three axes is required to control the orientation of the helicopter in free-flight. Typically, for most helicopters, three independent controls are used for this purpose. They are collective pitch(θ_o), lateral and longitudinal cyclic pitch(θ_{1c} and θ_{1s}), and tail rotor collective pitch (θ_{TR}).

Helicopter trim analysis, in general, falls into two categories: free-flight trim and wind-tunnel trim. In a wind-tunnel trim, which is used for model rotors that are tested in the wind tunnel, only the force equations are considered. In a free-flight trim, on the other hand, the solution simulates the free-flight conditions of the vehicle, and hence moment equations are also taken into account.

In RCAS, trimmed flight is generally defined by the satisfaction of two sets of equations:

1. The periodicity constraint equations for the system dynamic response and,
2. The trim target constraint equations that determine if the desired equilibrium condition has been reached.

Rotorcraft trim analysis involves the determination of the periodic steady

response and control settings that satisfy the above conditions. The time-average value of any output parameter, such as the aerodynamic forces/moments and tip-path-plane angles, may be selected as a trim target. Any control input or variable that independently affects the trim target responses may be selected as a trim variable. In doing so, the trim targets and the corresponding trim variables have to be related. For instance, the change in collective pitch has the biggest influence on the rotor thrust. The change in lateral cyclic pitch has the most influence on the roll moment and lateral flapping. Similarly, the longitudinal cyclic has the most effect on the rotor pitch moment and longitudinal flapping.

In a normal free-flight case of the helicopter with six degrees of freedom, the trim variables are collective pitch (θ_o), lateral cyclic pitch (θ_{1c}), longitudinal cyclic pitch (θ_{1s}), tail rotor collective (θ_{TR}), and the aircraft orientation angles. The trim targets corresponding to these trim variables are the vehicle forces and moments.

One can also perform trim analysis on an isolated rotor in RCAS. In this situation, the vertical force and the roll and pitch moments are trimmed to the desired values using the collective, and the lateral and longitudinal cyclic pitch. This option amounts to trimming for a desired thrust and tip-path-plane angle.

Trim Solution Procedure

The trim procedure used in RCAS involves the following steps:

1. The trim variables are organized into an array (V_t), which may include a combination of pilot controls (θ_o, θ_{1c}, θ_{1s}, θ_{TR}), global frame orientations and/or any appropriate user defined variable.

2. A wake model is then chosen. By default, RCAS invokes uniform inflow for the initial trim; however, one may specify any initial wake model (uniform inflow, prescribed wake, free wake, dynamic inflow, or CFD wake).

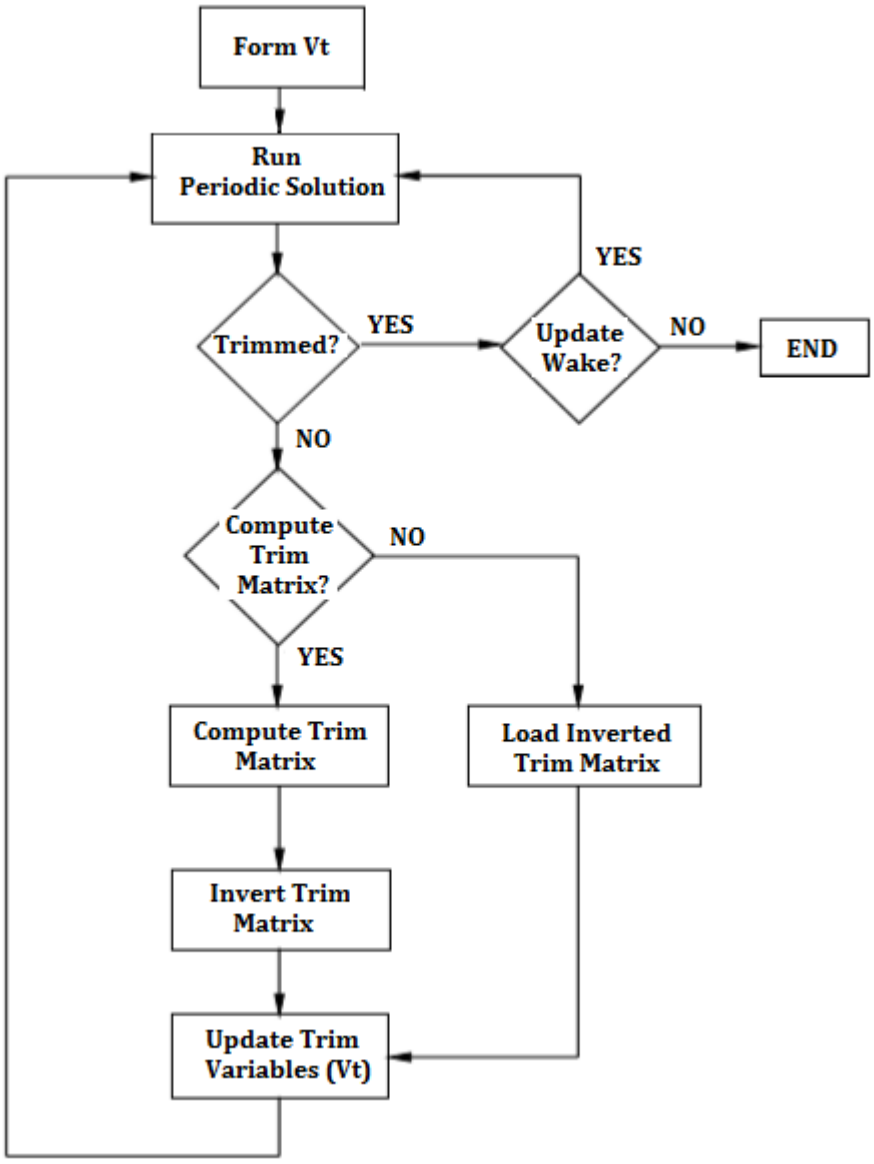

Figure B.1. RCAS trim procedure [22].

3. With the selected wake model for trim updates, the periodic solution of the system dynamic equations is performed.

4. Next, it is checked if trim is achieved. If the net forces are within the trim constraints, then the system is considered to be trimmed. otherwise the trim procedure will continue with the following step. If the system achieves a trimmed state and the current wake model is the final wake model, then the

final trim has been reached and the simulation terminates. If the system is trimmed and the current wake model is not the final wake model, then the wake is updated to the next selected wake model. Step 3 is then repeated.

5. It is then determined if the trim sensitivity matrix needs to be calculated. By default, RCAS calculates a new trim sensitivity matrix at the beginning of each trim and uses this matrix for the rest of the trim (or until the wake model is changed). The user may, however, define an interval of trim iterations between successive trim sensitivity matrix updates. A preexisting trim matrix may also be used to avoid calculation of the trim matrix and thus save simulation time. If a new trim sensitivity matrix is to be calculated, then step 6 is executed, otherwise step 7 is performed next.

6. The trim sensitivity matrix (derivative matrix), $\left[\frac{\partial g}{\partial V_i}\right]$, where g is an array of the trim constraint forces and moments, is assembled. The trim sensitivity matrix represents the change in trim constraints with respect to a perturbation of each trim variable. One may specify the wake model (uniform inflow, prescribed wake, free wake, or dynamic inflow) specifically for the calculation of the trim sensitivity matrix. If a wake model is not specified for the trim matrix calculation, then uniform inflow is used by default. Choosing uniform inflow is usually good enough and saves time.

   The trim sensitivity matrix is evaluated via the following procedure:

   (a) The first element ($j = 1$) of V_t is decreased by an increment ΔV_{tj}. The trim constraint forces and moments, g_j, are calculated by performing a periodic solution and averaging each trim constraint force/moment.

   (b) The j_{th} column of the trim sensitivity matrix is calculated by $\left[\frac{\partial g}{\partial V_t}\right]_j = \frac{g_j - g_{old}}{\Delta V_{tj}}$, where g_{old} is the net forces and moments of each trim constraint obtained using the initial values of V_t.

(c) Steps 6(a) to 6(b) are repeated for each parameter, j, of the trim variable array V_{t_j} until the full trim sensitivity matrix, $\left[\frac{\partial g}{\partial V_i}\right]$, is generated.

(d) Then the inverse of the trim sensitivity matrix, $\left[\frac{\partial g}{\partial V_i}\right]^{-1}$, is computed .

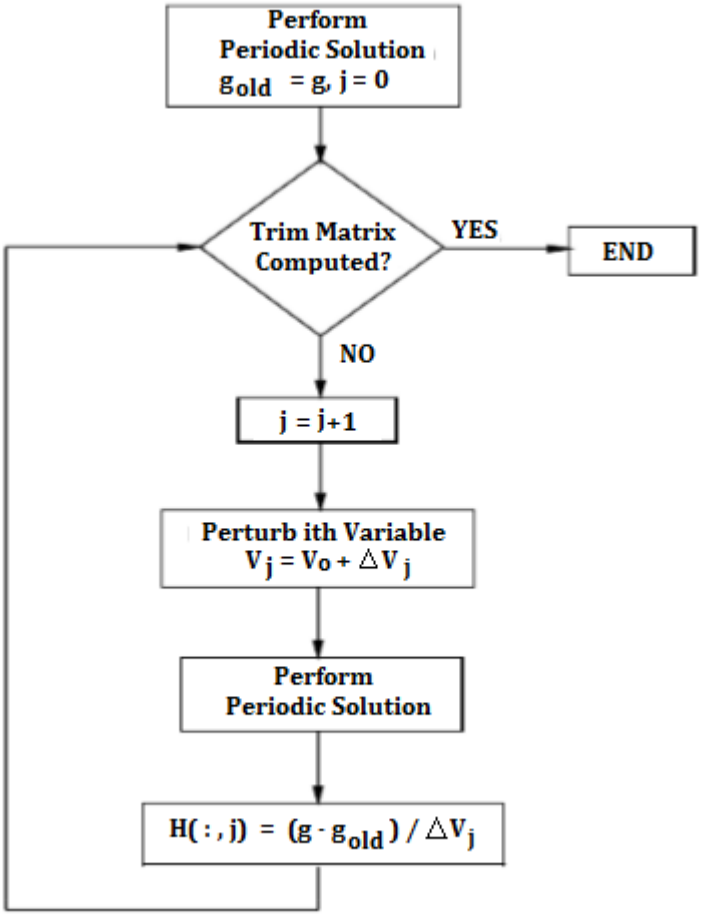

Figure B.2. RCAS trim matrix computation flowchart [22].

7. The elements of V_t are updated using the modified Newton-Raphson method. $V_{t_{i+1}} = V_{t_i} + \left[\frac{\partial g}{\partial V_i}\right]^{-1} g_i \cdot R_{FAC}$. For the first iteration ($i = 1$), V_{t_i} is the initial assumed value of V_t and g_i is the corresponding net forces and moments (g_{old}). $R_{FAC} \leq 1$ is a factor used to avoid overshooting of the parameters of V_t.

8. Using the selected wake model for trim updates, the periodic solution is performed and the averaged forces and moments of the trim constraints are

calculated.

9. It is checked again if trim has been reached. Trim completion for the current loop is achieved when the net forces are within the trim constraints. When the current trim loop has been completed, RCAS checks if the current wake model is the final wake model. If so, the final trim has been reached and the trim procedure is completed. If not, then the wake is updated to the next selected wake and the next trim loop is started from Step 5. When the system is still not trimmed, RCAS will check if the maximum number of iterations has been exceeded. If so, the trim solution has failed, and RCAS terminates the analysis. Otherwise, the trim solution will continue from Step 5 for another iteration.

Figures B.1 and B.2 show flow diagrams of the trim procedure and trim matrix computation procedure respectively.

Appendix C
RCAS Coupling Files

C.1 RCAS Input Script

```
***begin-RCAS-file: scriptfile ***
! Initialize RDB - use menu RCASROOT
MENU RCASROOT
! Choose Reinitialize RCAS
11
E

! <carriage return> and choose Initialize RCAS...
1

! <carriage return> and return to command mode
COMMAND

!========================================================================
!============================ MODEL =====================================
!========================================================================

S SUBSYSIDS
!  Model Composition
!  Subsystem Name(s)
a      rotor1

S GFRAMEORIG
!    Rigid Body Frame Attachment Node and Active Degrees of Freedom
!   Subsystem       Prim. Struc.    Node    Active Degrees of Freedom
!     Name             Name         ID      u   v   w   p   q   r
a    rotor1          blade11         20       0   0   0   0   0   0

S SSORIGIN
!    Subsystem              Origin Coordinates
!      Name             X            Y            Z
a     rotor1            0            0            0

S SSORIENT
!   Subsystem     Rotation 1        Rotation 2        Rotation 3
!     Name      Axis Angle(Deg)   Axis Angle(Deg)   Axis Angle(Deg)
a    rotor1      2      177        0        0        0       0

S CONTROLMIXER
! Control  Value at Zero    -------- Coefficients for Pilot Control --------
!   ID     Pilot Control    Coll.       Lat.       Long.      Pedal     Throt.
a    1           0          .017453       0          0          0         0
a    2           0            0        .017453       0          0         0
a    3           0            0          0         .017453       0         0

!========================================================================
```

```
!============================== SUBSYSTEM ================================
!=========================================================================

S SELSUBSYS
! Subsystem Name
a    rotor1

S SINGLEBLADE
!   Single Blade        Number of     Maneuver
!  Analysis Option       Blades       allowed
!      (Y/N)             (1:30)        (0/1)
a        Y                 4            0

S SUBSYSTYP
! Subsystem Type
! 1=Rotor, 2=Fuselage
a         1

S SUBSYSCOMP
!          Primitive Structure
!                Name
a                blade11

S CORNODE
!  Primitive    Rotor/Shaft   Torque           Rotor Reference
!  Structure    Connection    Bearing             Azimuth ID
!    Name        Node ID      Defined          SSname_PSname_ELname
a   blade11         20

S BLADECOMP
! Blade                  Primitive Structure Name(s)
! Index     1          2         3         4         5         6         7
a   1    blade11      --        --        --        --        --        --

S PSORIGIN
!    Primitive            Primitive Origin Offset
!      Name             x            y            z
a     blade11           0            0            0

S PSORIENT
!   Primitive      Rotation 1        Rotation 2        Rotation 3
!     Name       Axis  Angle(deg)  Axis  Angle(deg)  Axis  Angle(deg)
a   blade11      3        0        0        0        0        0

S ROTORPARAM
!          Rotor Rotational
!          Speed (rad/sec)
a               221.45

!=========================================================================
!======================== PRIMITIVE STRUCTURE ============================
!=========================================================================

S PRIMITIVEID
! Primitive Structure Name
a          blade11

S ELDATASETID
!   Element Data Table Name
a           ELPROPR

S FENODE
!    Node             Node Coordinates (feet)
!     ID           x            y            z
a     20           0            0            0      ! Blade root Node
a     8         2.82333           0            0      ! blade tip node

S RIGIDBLADE
!  Element   Node   Prop       Hinge Sequence Number (0-3)
!    ID       ID     ID     Lead-Lag    Flap     Pitch Bearing
a     1       20     1         0         1             0

S CONTROLCONNECT
! Control   Swashplate   Swashplate    Element Type        Element
!   ID      or Direct    Phase(deg)  (HIN/AUX/MLD ...)    or ACP ID
a    1        SPCOLL        0.0             RBE              1
a    2        SPLATR        0.0             RBE              1
a    3        SPLONG        0.0             RBE              1
```

```
!========================================================================
!======================== STRUCTURAL PROPERTIES =========================
!========================================================================

S ELEPROPID
!    Element Data Table Name
a          ELPROPR

S RBEPRP
!             -------------------- Lead-Lag Hinge ---------------------
!  Prop        Hinge Offset        Mass         Damping         Stiffness
!   ID             (ft)          (slugs)  (ft-lbf-sec/rad)  (ft-lbf/rad)
a   1             0.167            0              0               0

N
!             -------------------- Flap Hinge ------------------------
!  Prop        Hinge Offset        Mass         Damping         Stiffness
!   ID             (ft)          (slugs)  (ft-lbf-sec/rad)  (ft-lbf/rad)
a   1             0.167            0              0               0

N
!             -------------------- Pitch Bearing ---------------------
!  Prop        Hinge Offset        Mass         Damping         Stiffness
!   ID             (ft)          (slugs)  (ft-lbf-sec/rad)  (ft-lbf/rad)
a   1              0                0              0               0

N
!  Prop        Blade Mass      Blade CG          Ixx             Iyy
!   ID          (slugs)          (ft)       (slug-ft**2)    (slug-ft**2)
a   1          0.0177           0.521         0.0002          0.04436

!========================================================================
!============================ AIRFOIL DATA ==============================
!========================================================================

S AIRFOIL
!   Airfoil              Quasi Steady Airloads
!     ID                  2D Table File Name
a   bladeaf                 NACA0012.C81

!========================================================================
!======================== AERODYNAMIC MODEL =============================
!========================================================================

S AEROMODCOMP
!    Supercomponent Name
a        ADROTOR

S SCORIGIN
! Supercomponent            Origin Coordinates
!      Name             x            y            z
a     ADROTOR           0            0            0

S SCORIENT
! Supercomponent    Rotation 1       Rotation 2        Rotation 3
!      Name       Axis Angle(deg)  Axis Angle(deg)  Axis Angle(deg)
a    ADROTOR       2      177       0       0        0       0

!========================================================================
!====================== AERODYNAMIC SUPERCOMPONENT ======================
!========================================================================

S AEROSUPCOMPID
!  Supercomponent Name
a        ADROTOR

S SUPCMPTYP
! Supercomponent Type
! 1=Rotor, 2=Wing, 3=Body, 4=Aux. Rotor
a         1

S COMPID
!  Aerodynamics  Primitive   Auxrotor/   Wing Left End    Wing
!   Component    Structure   Body/Wing   or Blade Tip   Right End
!    Name(s)      Name(s)   Root EL_ID     Node_ID       Node_ID
a   ablade11      blade11       0             8            0

S CPORIGIN
!    Component            Component Origin Offset
```

```
!      Name              X             Y             Z
a    ablade11            0             0             0

S CPORIENT
!   Component     Rotation 1          Rotation 2         Rotation 3
!     Name       Axis  Angle(Deg)  Axis  Angle(Deg)  Axis  Angle(Deg)
a   ablade11      3        0        0        0        0        0

S INFLOW
! Inflow Model
!   0. No Inflow
!   1. Uniform Momentum Inflow (half wings and rotors)
!   2. Uniform Momentum Inflow (full wings)
!   3  Peters and He Inflow Model (rotors & wings)
!   4. Wing Vortex Wake
!   5. Prescribed Vortex Wake (rotors only)
!   6. Free Vortex Wake (Scully, Maryland, etc.)
!   7. Vortex Particle Method (VVPM)
!   8. External Vortex Wake
!   9. Blade Element (Annular Disk) Momentum Inflow
!  33. Peters and He inflow (variable diameter rotors)
a         8

S DYNINFDATA
!     Number of          Number of       Instantaneous or Mean
!    Polynomials         Harmonics         Inflow Flag (0/1)
a        8                  8

S AEROPTION
!  Yawed     Tip      Linear     Nonlinear-Unsteady  Airfoil-Coeff Compress
!  Flow      Loss    Unsteady    With Dynamic Stall  Table-Lookup  -ibility
! Effects  Option   Effects     LEISHBED/ONERA/PHT    or Linear     Effects
!  (0:1)   (0:1)     (0:1)            (0:12)            (0:1)        (0:1)
a    0       1         0                0                 0            0

S TIPLOSS
!Radial Location
! for Zero Lift
!   (nondim)
a 0.98

S THRUSTAVE
! Thrust Average      # Time Steps          Prescribed     # of Revolutions
!     Option          in Thrust Ave.          Thrust         to Average TPP
a        2                 72               14190              1

S SUPCMPTOSS
!  Subsystem Name
a     rotor1

!========================================================================
!======================== AERODYNAMIC COMPONENT =========================
!========================================================================

S AEROCOMPID
!     Aerodynamic Component Name
a              ablade11

S COMPTYPE
! Component Type
! 1=Lifting Surface, 2=Body, 3=Aux/tail rotor
a         1

S AERONODE
!    Aerodynamic node IDs and their coordinates WRT component
!  Node       ------------------ Coordinates ------------------
!   ID              X                 Y                Z
a    1               0.69                0                0
a    2               0.81                0                0
a    3               0.92                0                0
a    4               1.04                0                0
a    5               1.16                0                0
a    6               1.28                0                0
a    7               1.40                0                0
a    8               1.52                0                0
a    9               1.64                0                0
a    10               1.76                0                0
a    11               1.87                0                0
```

```
a    12                  1.99                  0                  0
a    13                  2.11                  0                  0
a    14                  2.23                  0                  0
a    15                  2.35                  0                  0
a    16                  2.47                  0                  0
a    17                  2.59                  0                  0
a    18                  2.70                  0                  0
a    19                  2.82                  0                  0


S AEROSEG
!  Seg.  Aerodyn Node IDs    Chord    Airfoil  Element    Twist      Shear Ang
!  ID    (Pnode)  (Cnode)     (ft)      ID       ID       (rad)       (rad)
a   1       1        2       0.2167   bladeaf     0       0.0678
a   2       2        3       0.2167   bladeaf     0       0.0619
a   3       3        4       0.2167   bladeaf     0       0.0560
a   4       4        5       0.2167   bladeaf     0       0.0502
a   5       5        6       0.2167   bladeaf     0       0.0443
a   6       6        7       0.2167   bladeaf     0       0.0384
a   7       7        8       0.2167   bladeaf     0       0.0326
a   8       8        9       0.2167   bladeaf     0       0.0267
a   9       9        10       0.2167   bladeaf     0       0.0208
a   10       10        11       0.2167   bladeaf     0       0.0150
a   11       11        12       0.2167   bladeaf     0       0.0091
a   12       12        13       0.2167   bladeaf     0       0.0032
a   13       13        14       0.2167   bladeaf     0       -0.0027
a   14       14        15       0.2167   bladeaf     0       -0.0087
a   15       15        16       0.2167   bladeaf     0       -0.0147
a   16       16        17       0.2167   bladeaf     0       -0.0204
a   17       17        18       0.2167   bladeaf     0       -0.0261
a   18       18        19       0.2167   bladeaf     0       -0.0320

!====================================================================
!========================== ANALYSIS DATA ===========================
!====================================================================

S SELANALYSIS
!  Case    Trim    Mane    Stab    Init
!   ID     (0-3)   (0-1)   (0-1)   Cond
a   01       1       0       0       S   NO

N
!  Case ID          Case Title (Maximum 30 Characters)
a    01                          EXTVW

S INITCOND
!  Collective      Lateral      Longitudinal      Pedal      Throttle
a     8.5           1.52            -4.13           0.0         0.0

N
!      Xo            Yo            Zo           Roll         Pitch          Yaw
a      0.            .0            0            0.0          -.04            0

S SYSTEMFLAGS
!     Gravity         Aero
!     Effects        Effects
a        1              1

S CONSTWIND
!          V_x                 V_y                 V_z
!       (ft/sec)            (ft/sec)            (ft/sec)
a       -143.90               0.0                 0.0

S AEROSTATCONST
!    Spec       Vehicle          Air             Air        Speed of
!    Type       Altitude     Temperature       Density       Sound
a     0            0              0              0            0

!====================================================================
!========================= TIME INTEGRATION =========================
!====================================================================

S CONVERGETOL
! Max.   Max.   # of    ------------------- Tolerances ------------------    Min.
! # of   # of   Time     Translation    Rotation    Translation    Rotation    # of
! trim   Revs   Steps    Displacement    Angles     Displacement     Angles    Revs
! Upds   PSol   /Rev        DOFs         DOFs          DOFs           DOFs     PSol
a  30     50     72         0.001        0.0005          1             .2       6
```

```
S INTEGPARAM
! No. of| Newmark Constants|   HHT   |  Displace.  | Velocity | Relax.
! Iter. | Alpha  |  Delta  |  Param  |    Tol      |   Tol    | Factor
a  70      .25       .5       -.03       1.0E-6       1.0E-5     1.0

!=========================================================================
!============================ TRIM DATA ==================================
!=========================================================================

S TRIMVAR
! Trim    TrimVar     TrimVar    Target   Target      Target
! VarID  PertValue    DampFac     ID      Value        Tol
a   1      0.25         0.5        8     8.0E-03      1.0E-04
a   2      0.25         0.5        9     0.0E+00      1.0E-03
a   3      0.25         0.5       10     0.0E+00      1.0E-03

N
! Target ID                      Concatenated Name of the Trim Target
a     8                              rotor1_aeropar_rotct
a     9                              rotor1_tppc_betac
a    10                              rotor1_tppc_betas
!N
!!  LOAD, SAVE,               Trim Sensitivity
!!  PREV, PNS                 Matrix File Name
!!N
!! Row    Number of  Inflow Model for  Option to Compute   Inflow Model
!! ID   Trim Updates   Trim Updates    Trim Matrix (0/1)  for Trim Matrix
!a  1        6           uniform              1              uniform
!a  2        6           uniform              1              uniform
!a  3        6           uniform              1              uniform
!a  4        6           uniform              1              uniform


!=========================================================================
!========================== OUTPUT DATA ==================================
!=========================================================================

S PERIODICOUTPUT
!  Row   Subsystem   Prim. Struc.           Output
!  ID      Name         Name               Category
a   1       all          all              Internal.Loads
a   2       all          all                 Airloads

S LOGFILEOPTIONS
! Conversion to    Internal     Default
! Rscope Scripts    Loads       Report
!   (Y/N)           (Y/N)       (Y/N)
aY     Y     Y

S SAVESC
!  Form of SC Data          Directory and File Name         Number of
!   (RDB or FILES)              for SC Data               Output Steps
!    <SCFORM>                    <SCFILNAM>                in One File
a        RDB                      extvw.sav

S CONFIRMSCR
!  Single blade
!  confirm value
!      (0/1)
a                          1

S RUNALLCASES
!    Run All Cases Flag ( 0/1 )
a                0

EXIT

M  RUNANALYSIS

m

1

r

*****end-RCAS-file: scriptfile ***

***begin-RCAS-file: useradditionalmodel.exc ***
```

```
// Cleanup sdx shared memory
//  if TMPDIR is not set you may want to set it to /tmp
     // setenv TMPDIR /tmp
     // setenv USER txc279

shell("\rm -rf $TMPDIR/sdx-$USER ")


//  External wake configuration

  pushg(world_model_rotor1)
    world_analysis_extvwakeflag =1    // flag to turn on extvww
    world_analysis_extvwakepers = 0   // exchange flag for periodic solution
                                      // when 1 exchange after each peri. solu
    world_analysis_vwakemaxniter = 12  // max N exchange for trim

    world_model_rotor1_unifextwake_selfivextflag = 1;

    // After the next release remove next line and
    //      uncomment the following line
  shell("cp  ../vortexwakecplfiles2014/* .")
   //shell("cp $rfunc/vortexwakecplfiles2014/* .")
  popg

  //
  // If trim exchange then set maxnpersloop to 1
  //
  world_analysis_trim_maxnpersloop = 10
  if  world_analysis_extvwakepers ==0,
    world_analysis_trim_maxnpersloop = 1
  end
*****end-RCAS-file: useradditionalmodel.exc  ***

***begin-RCAS-file: useradditionalpretrim.exc ***

  //
  // Set additional parameters right before starting trim
  //
  pushg(world)
    group vwakeio
      nrotor = 1
      exec("vwake_setup.exc",1)
      urelaxbcdata = 0.4  // Under-relaxion for bcdata (bound circ.)
      urelaxivdata = 0.8  // Under-relaxion for ivdata ( induced Veloc)
      diffplot = 1;      // Not used
      iterno2save = 1  // LCP iteration number to save coupling data
      reldiffivtol = 0.03  // change to a reasonable number like .1
                           // aqfter emulation is done
  popg

*****end-RCAS-file: useradditionalpretrim.exc ***


***begin-RCAS-file: NACA0012.C81 ***
      0012                    11391165 947
       0.     .20    .30    .40    .50    .60    .7     .75    .8
       .9     1.
-180.  0.     0.     0.     0.     0.     0.     0.     0.     0.
       0.     0.
-172.5 .78    .78    .78    .78    .78    .78    .78    .78    .78
       .78    .78
-161.  .62    .62    .62    .62    .62    .62    .62    .62    .62
       .62    .62
-147.  1.     1.     1.     1.     1.     1.     1.     1.     1.
       1.     1.
-129.  1.     1.     1.     1.     1.     1.     1.     1.     1.
       1.     1.
-49.   -1.18  -1.18  -1.18  -1.18  -1.18  -1.18  -1.18  -1.18  -1.18
       -1.18  -1.18
-39.   -1.18  -1.18  -1.18  -1.18  -1.18  -1.18  -1.18  -1.18  -1.18
       -1.18  -1.18
-21.   -.8    -.8    -.81   -.83   -.85   -.85   -.85   -.71   -.68
       -.64   -.64
-16.5  -1.007 -1.007 -.944  -.96   -.965  -.965  -.965  -.795  -.76
```

```
        -.7     -.7
-15.    -1.19   -1.19   -1.09   -1.055  -.99    -.98    -.98    -.83    -.79
        -.72    -.72
-14.    -1.333  -1.333  -1.22   -1.096  -1.     -.97    -.97    -.84    -.805
        -.73    -.73
-13.    -1.334  -1.334  -1.28   -1.12   -1.     -.96    -.96    -.85    -.815
        -.735   -.735
-12.    -1.255  -1.255  -1.26   -1.13   -1.     -.947   -.94    -.85    -.82
        -.74    -.74
-11.     -1.161 -1.161  -1.19   -1.12   -.994   -.93    -.923   -.85    -.81
        -.74    -.74
-10.    -1.055  -1.055  -1.01   -1.082  -.985   -.91    -.90    -.845   -.805
        -.73    -.73
-8.     -.844   -.844   -.88    -.907   -.922   -.87    -.84    -.82    -.77
        -.695   -.695
-6.     -.633   -.633   -.66    -.684   -.741   -.77    -.75    -.77    -.72
        -.593   -.593
-4.     -.422   -.422   -.440   -.456   -.494   -.544   -.578   -.627   -.603
        -.396   -.396
-2.     -.211   -.211   -.22    -.228   -.247   -.272   -.313   -.350   -.395
        -.2     -.2
0.      0.      0.      0.      0.      0.      0.      0.      0.      0.
        0.      0.
2.      .211    .211    .22     .228    .247    .272    .313    .350    .395
        .2      .2
4.      .422    .422    .44     .456    .494    .544    .578    .627    .603
        .396    .396
6.      .633    .633    .66     .684    .741    .77     .75     .77     .72
        .593    .593
8.      .844    .844    .88     .907    .922    .87     .84     .82     .77
        .695    .695
10.     1.055   1.055   1.1     1.082   .985    .91     .90     .845    .805
        .73     .73
11.     1.161   1.161   1.19    1.12    .994    .93     .923    .850    .810
        .74     .74
12.     1.255   1.255   1.26    1.13    1.      .947    .94     .85     .82
        .74     .74
13.     1.334   1.334   1.28    1.12    1.      .96     .96     .85     .815
        .735    .735
14.     1.333   1.333   1.22    1.096   1.      .97     .97     .84     .805
        .73     .73
15.     1.19    1.19    1.09    1.055   .99     .98     .98     .83     .79
        .73     .73
16.5    1.007   1.007   .944    .96     .965    .965    .965    .795    .76
        .7      .7
21.     .8      .8      .81     .83     .85     .85     .85     .71     .68
        .64     .64
39.     1.18    1.18    1.18    1.18    1.18    1.18    1.18    1.18    1.18
        1.18    1.18
49.     1.18    1.18    1.18    1.18    1.18    1.18    1.18    1.18    1.18
        1.18    1.18
129.    -1.     -1.     -1.     -1.     -1.     -1.     -1.     -1.     -1.
        -1.     -1.
147.    -1.     -1.     -1.     -1.     -1.     -1.     -1.     -1.     -1.
        -1.     -1.
161.    -.62    -.62    -.62    -.62    -.62    -.62    -.62    -.62    -.62
        -.62    -.62
172.5   -.78    -.78    -.78    -.78    -.78    -.78    -.78    -.78    -.78
        -.78    -.78
180.    0.      0.      0.      0.      0.      0.      0.      0.      0.
        0.      0.
        0.      .18     .28     .38     .48     .62     .72     .77     .82
        .92     1.0
-180.   .022    .022    .022    .022    .022    .022    .022    .022    .022
        .022    .022
-175.   .062    .062    .062    .062    .062    .062    .062    .062    .062
        .062    .062
-170.   .132    .132    .132    .132    .132    .132    .132    .132    .132
        .132    .132
-165.   .242    .242    .242    .242    .242    .242    .242    .242    .242
        .242    .242
-160.   .302    .302    .302    .302    .302    .302    .302    .302    .302
        .302    .302
-140.   1.042   1.042   1.042   1.042   1.042   1.042   1.042   1.042   1.042
        1.042   1.042
-120.   1.652   1.652   1.652   1.652   1.652   1.652   1.652   1.652   1.652
        1.652   1.652
-110.   1.852   1.852   1.852   1.852   1.852   1.852   1.852   1.852   1.852
        1.852   1.852
-100.   2.022   2.022   2.022   2.022   2.022   2.022   2.022   2.022   2.022
```

	2.022	2.022							
-90.	2.022	2.022	2.022	2.022	2.022	2.022	2.022	2.022	2.022
	2.022	2.022							
-80.	1.962	1.962	1.962	1.962	1.962	1.962	1.962	1.962	1.962
	1.962	1.962							
-70.	1.842	1.842	1.842	1.842	1.842	1.842	1.842	1.842	1.842
	1.842	1.842							
-60.	1.662	1.662	1.662	1.662	1.662	1.662	1.662	1.662	1.662
	1.662	1.662							
-50.	1.392	1.392	1.392	1.392	1.392	1.399	1.392	1.392	1.392
	1.392	1.392							
-30.	.562	.562	.562	.562	.562	.562	.562	.562	.562
	.562	.562							
-21.	.332	.332	.332	.332	.332	.332	.332	.332	.332
	.332	.332							
-16.	.155	.155	.181	.207	.235	.257	.274	.292	.305
	.342	.342							
-15.	.102	.102	.148	.181	.209	.233	.252	.271	.282
	.298	.298							
-14.	.038	.038	.099	.146	.180	.212	.233	.249	.260
	.293	.293							
-13.	.0264	.0264	.0455	.094	.148	.191	.216	.231	.239
	.272	.292							
-12.	.022	.022	.030	.06	.111	.164	.198	.211	.220
	.252	.291							
-11.	.0196	.0196	.0232	.038	.078	.135	.17	.192	.202
	.232	.275							
-10.	.0174	.0174	.0189	.0259	.053	.105	.145	.176	.186
	.213	.254							
-9.	.0154	.0154	.0159	.0187	.0351	.077	.122	.159	.172
	.199	.232							
-8.	.0138	.0138	.0138	.0147	.0220	.053	.101	.140	.155
	.183	.214							
-7.	.0122	.0122	.0122	.0123	.0141	.035	.082	.111	.139
	.169	.192							
-6.	.011	.011	.011	.011	.011	.0212	.0615	.082	.12
	.14	.17							
-5.	.01	.01	.01	.01	.01	.0132	.038	.054	.084
	.111	.14							
-4.	.0093	.0093	.0093	.0093	.0093	.01	.0167	.03	.0575
	.095	.112							
-3.	.0088	.0088	.0088	.0088	.0088	.009	.0102	.0175	.0355
	.086	.102							
-2.	.0085	.0085	.0085	.0085	.0085	.0085	.0086	.0117	.0240
	.081	.098							
-1.	.0083	.0083	.0083	.0083	.0083	.0083	.0083	.0091	.0175
	.078	.096							
0.	.008	.008	.008	.008	.008	.008	.008	.008	.0137
	.078	.095							
1.	.0083	.0083	.0083	.0083	.0083	.0083	.0083	.0091	.0175
	.078	.096							
2.	.0085	.0085	.0085	.0085	.0085	.0085	.0086	.0117	.024
	.081	.098							
3.	.0088	.0088	.0088	.0088	.0088	.0090	.0102	.0175	.0355
	.086	.102							
4.	.0093	.0093	.0093	.0093	.0093	.01	.0167	.03	.0575
	.095	.112							
5.	.01	.01	.01	.01	.01	.0132	.038	.054	.084
	.111	.14							
6.	.011	.011	.011	.011	.011	.0212	.0615	.082	.12
	.14	.17							
7.	.0122	.0122	.0122	.0123	.0141	.035	.082	.111	.139
	.169	.192							
8.	.0138	.0138	.0138	.0147	.022	.053	.101	.14	.155
	.183	.214							
9.	.0154	.0154	.0159	.0187	.0351	.077	.122	.159	.172
	.199	.232							
10.	.0174	.0174	.0189	.0259	.053	.105	.145	.176	.186
	.213	.254							
11.	.0196	.0196	.0232	.038	.078	.135	.17	.192	.202
	.232	.275							
12.	.022	.022	.03	.06	.111	.164	.198	.211	.22
	.252	.291							
13.	.0264	.0264	.0455	.094	.148	.191	.216	.231	.239
	.272	.292							
14.	.038	.038	.099	.146	.18	.212	.233	.249	.26
	.293	.293							
15.	.102	.102	.148	.181	.209	.233	.252	.271	.282
	.298	.298							
16.	.155	.155	.181	.207	.235	.257	.274	.292	.305

	.342	.342							
21.	.332	.332	.332	.332	.332	.332	.332	.332	.332
	.332	.332							
30.	.562	.562	.562	.562	.562	.562	.562	.562	.562
	.562	.562							
50.	1.392	1.392	1.392	1.392	1.392	1.392	1.392	1.392	1.392
	1.392	1.392							
60.	1.662	1.662	1.662	1.662	1.662	1.662	1.662	1.662	1.662
	1.662	1.662							
70.	1.842	1.842	1.842	1.842	1.842	1.842	1.842	1.842	1.842
	1.842	1.842							
80.	1.962	1.962	1.962	1.962	1.962	1.962	1.962	1.962	1.962
	1.962	1.962							
90.	2.022	2.022	2.022	2.022	2.022	2.022	2.022	2.022	2.022
	2.022	2.022							
100.	2.022	2.022	2.022	2.022	2.022	2.022	2.022	2.022	2.022
	2.022	2.022							
110.	1.852	1.852	1.852	1.852	1.852	1.852	1.852	1.852	1.852
	1.852	1.852							
120.	1.652	1.652	1.652	1.652	1.652	1.652	1.652	1.652	1.652
	1.652	1.652							
140.	1.042	1.042	1.042	1.042	1.042	1.042	1.042	1.042	1.042
	1.042	1.042							
160.	.302	.302	.302	.302	.302	.302	.302	.302	.302
	.302	.302							
165.	.242	.242	.242	.242	.242	.242	.242	.242	.242
	.242	.242							
170.	.132	.132	.132	.132	.132	.132	.132	.132	.132
	.132	.132							
175.	.062	.062	.062	.062	.062	.062	.062	.062	.062
	.062	.062							
180.	.022	.022	.022	.022	.022	.022	.022	.022	.022
	.022	.022							
	.20	.30	.40	.50	.6	.7	.75	.8	.9
-180.	0.	0.	0.	0.	0.	0.	0.	0.	0.
-170.	.4	.4	.4	.4	.4	.4	.4	.4	.4
-165.	.3	.3	.3	.3	.3	.3	.3	.3	.3
-160.	.3	.3	.3	.3	.3	.3	.3	.3	.3
-135.	.5	.5	.5	.5	.5	.5	.5	.5	.5
-90.	.5	.5	.5	.5	.5	.5	.5	.5	.5
-30.	.174	.184	.196	.214	.235	.25	.264	.277	.298
-23.	.112	.118	.128	.144	.157	.171	.183	.206	.232
-16.	.073	.078	.086	.097	.108	.117	.137	.176	.200
-15.	.054	.065	.073	.084	.097	.111	.133	.173	.195
-14.	0.	.027	.054	.068	.086	.103	.127	.167	.189
-13.	0.	.0015	.025	.05	.074	.093	.122	.163	.184
-12.	0.	0.	.002	.03	.06	.083	.116	.157	.176
-11.	0.	0.	-.003	.014	.046	.074	.108	.149	.17
-10.	0.	0.	-.0015	.002	.032	.065	.10	.142	.163
-9.	0.	0.	0.	-.003	.016	.054	.089	.132	.154
-8.	0.	0.	0.	-.004	.005	.041	.082	.123	.145
-7.	0.	0.	0.	0.	-.004	.0275	.072	.1125	.136
-6.	0.	0.	0.	0.	-.003	.016	.0625	.10	.125
-4.	0.	0.	0.	0.	0.	.005	.04	.076	.102
-3.	0.	0.	0.	0.	0.	-.0025	.026	.0665	.087
-2.	0.	0.	0.	0.	0.	0.	.013	.053	.07
-1.	0.	0.	0.	0.	0.	0.	.0035	.033	.045
0.	0.	0.	0.	0.	0.	0.	0.	0.	0.
1.	0.	0.	0.	0.	0.	0.	-.0035	-.033	-.045
2.	0.	0.	0.	0.	0.	0.	-.013	-.053	-.07
3.	0.	0.	0.	0.	0.	.0025	-.026	-.0665	-.087
4.	0.	0.	0.	0.	0.	-.005	-.04	-.076	-.102
6.	0.	0.	0.	0.	.003	-.016	-.0625	-.1	-.125
7.	0.	0.	0.	0.	.004	-.0275	-.072	-.1125	-.136
8.	0.	0.	0.	.004	-.005	-.041	-.082	-.123	-.145
9.	0.	0.	0.	.003	-.016	-.054	-.089	-.132	-.154
10.	0.	0.	.0015	-.002	-.032	-.065	-.1	-.142	-.163
11.	0.	0.	.003	-.014	-.046	-.074	-.108	-.149	-.17
12.	0.	0.	-.002	-.03	-.06	-.083	-.116	-.157	-.176
13.	0.	-.0015	-.025	-.05	-.074	-.093	-.122	-.163	-.184
14.	0.	-.027	-.054	-.068	-.086	-.103	-.127	-.167	-.189
15.	-.054	-.065	-.073	-.084	-.097	-.111	-.133	-.173	-.195
16.	-.073	-.078	-.086	-.097	-.108	-.117	-.137	-.176	-.20
23.	-.112	-.118	-.128	-.144	-.157	-.171	-.183	-.206	-.232
30.	-.174	-.184	-.196	-.214	-.235	-.250	-.264	-.277	-.298
90.	-.5	-.5	-.5	-.5	-.5	-.5	-.5	-.5	-.5
135.	-.5	-.5	-.5	-.5	-.5	-.5	-.5	-.5	-.5
160.	-.3	-.3	-.3	-.3	-.3	-.3	-.3	-.3	-.3
165.	-.3	-.3	-.3	-.3	-.3	-.3	-.3	-.3	-.3
170.	-.4	-.4	-.4	-.4	-.4	-.4	-.4	-.4	-.4

```
180.   0.     0.     0.     0.     0.     0.     0.     0.     0.

NACA0012 for Puma
from Bousman, US Army, October 1988

corrected cd typo at alpha=-10; October 1988

*****end-RCAS-file: NACA0012.C81 ***
```

C.2 Coupling Intermediary Program

```
C     Modified by Tenzin Choephel based on the program by Hossein Saberi (2011).

      Program  emuextvwlcp
      implicit none

      double precision couplingstatus, couplingtype
      double precision rcasvwiterno
      double precision rframedatarev(5000)
      double precision hubdatarev(10000)
      double precision acpdatarev(50000)
      double precision bcdatarev(10000)
      double precision ivdatarev(50000)
      double precision rframedatacur(50)
      double precision hubdatacur(100)
      double precision acpdatacur(500)
      double precision bcdatacur(100)
      double precision ivdatacur(500)
      double precision temp_acpposr(40,72) ! temporary vector
      double precision avg_acpposr(40)

      double precision extvwiterno
      character filnam*72, varname*20
      integer ios, nrow, ncol
      integer itstep, its, iter
      integer ii, jj, ndat, ioff, counter, countt
      integer nblade, naseg, ntstep
      integer IterStatus
      integer status, system

c      character*20 string1 /'./freewakeemu'/  ! freewake executable
      character*20 string1 /'./DVEforward'/  ! freewake executable

      double precision d2r
      parameter ( d2r = 1.745329251994330e-02 )
C
C=====================================================================
      ios = 1
C     Reading the number of aerodynamic segments or panels from free-wake input file
      open(unit=60, file='input.txt', iostat = ios,status='old')
      do ii = 1,63
        read(60,*)
      enddo
      read(60,'(44X, I3)') naseg

      nblade = 1    ! should be ``1'' for single-blade analysis in RCAS
      ntstep = 72

C     Loop for loose coupling iteration (maximum 100 times)
      do iter = 1, 100  !Max number of lcp iteration
        IterStatus = 0
        print *, ' loose coupling iteration number = ', iter
C
C       Coupling status- it is set by RCAS
C           1 = loose coupling (lcp)
C           2 = tight coupling (tcp)
C          99 = Terminate
        print *, ' Waiting to receive @couplingstatus lcp'
        call sdxget('@COUPLINGSTATUS'//char(0), couplingstatus, 1 )
        print *, ' Received couplingstatus lcp = ', couplingstatus
```

```
         if( couplingstatus .eq. 99 ) go to 5000  ! terminate run
         if( couplingstatus .eq. 2 ) go to 1000   ! move to tight coupling
C
         print *, ' Waiting to receive rframedatarev'
         ndat = 27*ntstep
         call sdxget('@RFRAMEDATAREV'//char(0), rframedatarev, ndat )
         print *, ' Received rframedatarev'

c       ================================Controls and Flapping=======================
         open( unit=40, file='data_vault/blade_harmonics.sav', iostat= ios, status='old')
         write(40,'(A8, A8, A8)') '&theta0', 'theta1c', 'theta1s'
         write(40,'(f8.4, f8.4,f8.4,)') rframedatarev(10),rframedatarev(11), &
                        rframedatarev(12)
         write(40,'(A8, A8, A8)') '&beta0', 'beta1c', 'beta1s'
         write(40,'(f8.4, f8.4,f8.4,)') rframedatarev(13),rframedatarev(14), &
                        rframedatarev(15)
         close(40)
c      ============================================================================
         print *, ' Waiting to receive hubdatarev'
         ndat =  (27+nblade*12)*ntstep
         call sdxget('@HUBDATAREV'//char(0), hubdatarev, ndat )
         print *, ' Received hubdatarev'

c     ============================Operational Parameters=========================
         open( unit=90, file='data_vault/operational_param.sav', iostat= ios, status='old')
         write(90,'(A9, A9, A9, A9)') '&Ux', 'Uy', 'Uz', 'Omega'
         write(90,'(f9.4,f9.4,f9.4,f9.4)') rframedatarev(25),rframedatarev(26), &
       rframedatarev(27), hubdatarev(2)
         write(90,'(A8, A8, A8)') '&pitch', 'roll', 'yaw'
         write(90,'(f8.4,f8.4,f8.4,)') hubdatarev(16),hubdatarev(17),hubdatarev(18)
         close(90)
c     ============================================================================
C
C        ACPPOSR is aero seg mid position with respect to blade ref
C        positions of all the acps. nseg*nblade*3*ntstep
C
         print *, ' Waiting to receive acpdatarev'
         ndat =  3*nblade*naseg*ntstep
         call sdxget('@ACPDATAREV'//char(0), acpdatarev, ndat )
         print *, ' Received acpdatarev'

c     ===================================ACP locations============================
         open( unit=60, file='data_vault/acp_position.sav', iostat= ios, status='old')
         counter = 1
         do ii = 1,naseg
         write(60,'(f8.4)') sqrt(acpdatarev(counter)**2+acpdatarev(counter+1)**2 + &
         acpdatarev(counter+2)**2)
         counter = counter+ 3
         enddo
         close(60)
c     ============================================================================
C
C        Bound circulation data  nseg*nblade*ntstep
C
         print *, ' Waiting to receive bcdatarev'
         ndat =  nblade*naseg*ntstep
         call sdxget('@BCDATAREV'//char(0), bcdatarev, ndat )
         print *, ' Received bcdatarev'

c     ============================Bound Circulation Data==========================
         open( unit=50, file='data_vault/bcdatarevemu.sav', iostat= ios, status='old')
         counter = 1
         do ii = 1,ntstep
         write(50,'(f8.4)') (bcdatarev(countt), countt = counter, (naseg + counter-1))
         counter = counter + naseg
         enddo
         close(50)
c     ============================================================================

c     ============================Free-wake Input=================================
c     This is where all the input data for free-wake (retrieved from RCAS analysis)
c     are collected in a single file
          open( unit=85, file='freewake_input.sav', iostat= ios, status='old')
          write(85,'(A)')'Input file for the freewake program.'
```

```
         write(85,'(A)')'=========================================='
         write(85,'(A8,A8,A8)')'@ nblade','naseg','ntstep'
         write(85,'(I8, I8, I8)') nblade, naseg, ntstep
         write(85,'(A)')'------------------------------------------'
         write(85,'(A9, A9, A9, A9)') '@      Ux', 'Uy', 'Uz', 'Omega'
         write(85,'(f9.4,f9.4,f9.4,f9.4)') rframedatarev(25),rframedatarev(26), &
      rframedatarev(27), hubdatarev(2)
         write(85,'(A)')'------------------------------------------'
         write(85,'(A8, A8, A8)') '@  pitch', 'roll', 'yaw'
         write(85,'(f8.4,f8.4,f8.4,)') hubdatarev(16),hubdatarev(17), &
      hubdatarev(18)   ! Not used in the freewake
         write(85,'(A)')'------------------------------------------'
         write(85,'(A8, A8, A8)') '@ theta0', 'theta1c', 'theta1s'
         write(85,'(f8.4, f8.4,f8.4,)') rframedatarev(10),rframedatarev(11), &
      rframedatarev(12)
         write(85,'(A)')'------------------------------------------'
         write(85,'(A8, A8, A8)') '@  beta0', 'beta1c', 'beta1s'
         write(85,'(f8.4, f8.4,f8.4,)') rframedatarev(13),rframedatarev(14), &
      rframedatarev(15)
         write(85,'(A)')'------------------------------------------'
         write(85,'(A)')'@acp radial stations.'

         counter = 1
         do ii = 1,naseg
         write(85,'(f8.4)') sqrt(acpdatarev(counter)**2+acpdatarev(counter+1)**2 &
      + acpdatarev(counter+2)**2)
         counter = counter+ 3
         enddo
         write(85,'(A)')'------------------------------------------'
         write(85,'(A)')'@bound circulation distribution.'

         counter = 1
         do ii = 1,ntstep
         write(85,'(f8.4)') (bcdatarev(countt), countt = counter, (naseg + counter-1))
         counter = counter + naseg
         enddo
         close(85)
c     ================================================================================

         status = system(string1)  ! free-wake executable
         if(status .ne. 0) stop 'system: error'

C     This program must wait here until free-wake is done, which is
C     achieved by the following while loop.

         do while(IterStatus .ne. 1)
         call sleep(20)           ! pauses for 20 seconds
         ! -open the file fw_iterstatus.dat
         open(unit = 65, file = 'fw_iterstatus.dat',iostat = ios, status = 'old')
         read(65,*)IterStatus          ! -assign the inter flag to 'IterStatus'
         close(65)                     ! -close the file
         enddo
c     The program waits in the above while loop until flag
c     in the file fw_iterstatus.dat is ``1''. The induced velocity file written by
c     free-wake is opened here and its contents copied to the
c     variable ivdatarev
         open( unit=78, file='ivdatarevemu.sav', iostat=ios, status='old' )!IV file

         if( ios .ne. 0 ) then
         print *, 'Error: Unable to open file '//filnam(1:25)
         endif
         read(78,*) varname, nrow, ncol
         print *, ' varname = ', varname
         print *, ' nrow=3*nacp*nblade = ', nrow
         print *, ' ncol=ntstep = ', ncol

C
C      Read the data in a one diemnsional array
C      ivdata(3,nseg,nblade,ntstep)
C
         read(78,*) (ivdatarev(ii),ii=1,nrow*ncol)
         close(78)
         if( 3*naseg*ntstep .ne. nrow*ncol) then
```

```
          print *, ' Error: Data mismatch '
          print *, ' 3*naseg, ntstep = ', 3*naseg, ntstep
          print *, ' nrow, ncol = ', nrow, ncol
          stop 134
          endif

          ndat = 3*nblade*naseg*ntstep
          print *, ' Posting ivdatarev 3*nacp*nblade*ntstep ', ndat
          call sdxput('@IVDATAREV'//char(0), ivdatarev, ndat )
          print *, ' DonePosting ivdatarev ndat done'
C
C         RCAS coupling iteration numbercccc
C
          print *, ' Waiting to receive rcasvwiterno'
          call sdxget('@RCASVWITERNO'//char(0), rcasvwiterno, 1 )
          print *, ' Received RCASVWITERNO'
          print *, ' rcasvwiterno = ', rcasvwiterno
C
C         Vortex wake iteration  number
C
          extvwiterno = iter
          print *, ' Posting extvwiterno  '
          call sdxput('@EXTVWITERNO'//char(0), extvwiterno, 1 )
          print *, ' Posting extvwiterno done '
          print *, ' extvwiterno = ', extvwiterno
          print *, '=========================================='
          print *, '=========================================='
          print *, ' '

c    ============================Reinitializing f-W flag==========================
c      the file fw_iterstatus.dat is opened here again and the flag set to ``0''.
         IterStatus = 0
         open( unit=65, file='fw_iterstatus.dat', iostat= ios, status='old')
         write(65,*)IterStatus
         close(65)
c    ===============================================================================
      enddo
 1000 continue

      stop
      end
```

References

[1] McCroskey, W. (1995) "Vortex Wakes of Rotorcraft," AIAA 1995-0530, *33rd AIAA Aerospace Sciences Meeting and Exhibit*, Reno, NV.

[2] Leishman, J. (2002) *Principles of Helicopter Aerodynamics*, Cambridge Aerospace Series, Cambridge University Press.

[3] Leishman, J. and A. Bagai (1998) "Challenges in Understanding the Vortex Dynamics Helicopter Rotor Wakes," *AIAA Journal*, **36**(7), pp. 1130–1140.

[4] Mangler, H., K.W.and Squire (1950) *The Induced Velocity Field of a Rotor*, ARC R & M–2642.

[5] Johnson, W. (2011) "Milestones in Rotorcraft Aeromechanics," *Journal of the American Helicopter Society*, **56**(3), pp. 1–24.

[6] Landgrebe, A. (1969) "An Analytical Method for Predicting Rotor Wake Geometry," *Journal of the American Helicopter Society*, **14**(4), pp. 20–32.

[7] Miller, W. and D. Bliss (1993) "Direct Periodic Solutions of Rotor Free Wake Calculations," *Journal of the American Helicopter Society*, **38**(2), pp. 53–60.

[8] Bagai, A. and J. Leishman (1995) "Rotor Free-Wake Modeling Using a Pseudo-Implicit Technique-Including Comparisons with Experimental Data," *Journal of the American Helicopter Society*, **40**(3), pp. 29–41.

[9] Bliss, D., L. Dadone, and D. Wachpress (1987) "Rotor Wake Modeling for High Speed Applications," in *The Proceedings of the 43rd Forum of the American Helicopter Society*, St. Louis, MO.

[10] Narducci, R. (2014) "OVERFLOW Simulation of Rotors in Hover: The Boeing Company," AIAA 2014-0208, *52nd Aerospace Sciences Meeting*, AIAA, National Harbor, MD.

[11] He, C. and J. Zhao (2009) "Modeling Rotor Wake Dynamics with Viscous Vortex Particle Method," *AIAA Journal*, **47**(4), pp. 902–915.

[12] Collins, K. (2008) *A Multi-Fidelity Framework for Physics Based Rotor Blade Simulation and Optimization*, Ph.D. thesis, Georgia Institute of Technology, Atlanta, Georgia.

[13] Horstmann, K. H. (1987) *Ein Mehrfach Traglinienverfahren und seine Verwendung für Entwurf und Nachrechnung nichtplanarer Flügelanordnungen*, Ph.D. thesis, Institut ür Entwurfsaerodynamik, Braunschweig, Germany.

[14] Bramesfeld, G. (2006) *A Higher Order Vortex-Lattice Method with a Force-Free Wake*, Ph.D. thesis, The Pennsylvania State University, University Park, PA.

[15] Basom, B. (2010) *Inviscid Wind Turbine Analysis Using Distributed Vorticity Elements*, Master's thesis, The Pennsylvania State University, University Park, PA.

[16] Maniaci, D. (2013) *Wind Turbine Design Using a Free-Wake Vortex Method with Winglet Application*, Ph.D. thesis, The Pennsylvania State University, University Park, PA.

[17] Caradonna, F. and C. Tung (1981) *Experimental and Analytical Studies of a Model Helicopter Rotor in Hover*, NASA TM–81232.

[18] Knight, M. and R. Hefner (1937) *Static Thrust Analysis of the Lifting Airscrew*, NACA TN–626.

[19] Boatwright, D. W. (1972) *Measurements of Velocity Components in the Wake of a Full-Scale Helicopter Rotor in Hover*, U.S. Army Air Mobility research and Development Lab. TR 72-33, Fort Eustis, VA.

[20] Susan, A. and D. Hoad (2002) "Assessment of Rotor Blade Angle of Attack from Experimental Inflow Data," *Journal of Aircraft*, **39**(5), pp. 722–730.

[21] Martin, P. B., M. J. Bhagwat, and J. Leishman (2000) "Strobed Laser-sheet Visualization of a Helicopter Rotor Wake," *Journal of Flow Visualization and Image Processing*, **7**(1).

[22] Schmitz, F. (1991) "Rotor Noise," in *Aeroacoustics of Flight Vehicles: Theory and Practice*, vol. 1, chap. 2, NASA Reference Publication 1258.

[23] Rankine, W. (1865) "On the Mechanical Principles of the Action of Propellers," in *Transactions of the Institute of Naval Architects*, vol. 6, pp. 13–39.

[24] Froude, W. (1878) "On the Elementary Relation Between Pitch, Slip and Propulsive Efficiency," in *Transactions of the Institute of Naval Architects*, vol. 19, pp. 47–57.

[25] Froude, R. (1889) "On the Part Played in Propulsion by Difference of Fluid Pressure," in *Transactions of the Institute of Naval Architects*, vol. 30, p. 390.

[26] Lanchester, F. (1915) "A Contribution to the Theory of Propulsion and the Screw Propeller," in *Transactions of the Institute of Naval Architects*, vol. 57, pp. 98–116.

[27] Betz, A. (1922) *The Theory of the Screw Propeller*, NACA TN–83.

[28] Glauert, H. (1928) *0n the Horizontal Flight of a Helicopter*, ARC R & M –1157.

[29] Glauert (1976) "Airplane Propellers," in *Aerodynamic Theory* (W. Durand, ed.), chap. 2, Springer Verlag, Berlin, Germany, reprinted by Peter Smith, Glouster, MA.

[30] Gustafson, F. and A. Gessow (1946) *Effect of Rotor Tip Speed on Helicopter Rotor Performance and Maximum Forward Speed*, NACA WR–L–97.

[31] Gessow, A. (1948) *Effect of Roto-Blade Twist and Plan-Form Taper on Helicopter Hovering Performance*, NASA TN–1542.

[32] Glauert, H. (1926) *A General Theory of the Autogiro*, ARC R & M–786.

[33] Coleman, R., A. Feingold, and C. W. Stempin (1945) *Evaluation of the Induced Velocity Fields of an Idealized Helicopter Rotor*, NACA WR–L–126.

[34] Drees, J. (1949) "The Theory of Airflow Through Rotors and Its Application to Some Helicopter Problems," *Journal of the Helicopter Association of Great Britian*, **3**(2), pp. 79–104.

[35] Payne, P. (1959) *Helicopter Dynamics and Aerodynamics*, Pitman & Sons, London.

[36] White, F. and B. Blake (1979) "Improved Method of Predicting Helicopter COntrol Response and Gust Sensitivity," in *35th Annual Forum of the American Helicopter Society, Washington DC*, pp. 47–57.

[37] Pitt, D. and D. Peters (1981) "Theoretical Prediction of Dynamic Inflow Derivatives," *Vertica*, **5**, pp. 21–34.

[38] Howlett, J. (1981) *UH-60A Blackhawk Engineering Simulation Program: Vol. 1 Mathematical Model*, NASA CR–66309.

[39] Pitt, D. and D. Peters (1983) "Rotor Dynamic Inflow Derivatives and Time Constants from Various Inflow Models," in *9th European Rotorcraft Forum*, Stresa, Italy.

[40] Peters, D., D. Boyd, and C. He (1989) "A Finite-State Induced Flow Model for Rotors in Hover and Forward FLight," *Journal of the American Helicopter Society*, **34**(4), pp. 5–17.

[41] Johnson, W. (2013) *Rotorcraft Aeromechanics*, Cambridge University Press.

[42] Padfield, G. (1996) *Helicopter Flight Dynamics: The Theory and Application of Flying Qualities and Simulation*, AIAA Education Series, Washington, DC.

[43] Landgrebe, A. (1972) "The Wake Geometry of a Hovering Rotor and its Influence on Rotor Performance," *Journal of the American Helicopter Society*, **17**(4), pp. 3–15.

[44] Gray, R. (1992) "Vortex Modeling for Rotor Aerodynamics- 1991 Alexander A. Nikolsky Lecture," *Journal of the American Helicopter Society*, **37**(1), pp. 3–14.

[45] Kocurek, J. and J. Tangler (1976) "A Prescribed Wake Lifting Surface Hover Performance Analysis," in *Proceedings of the 32nd Forum of the American Helicopter Society*, Washington D.C.

[46] Egolf, T. and A. Landgrebe (1983) *Helicopter Rotor Wake Geometry and its Influence in Forward Flight*, NASA CR–3726.

[47] Scully, M. (1967) *A Method of Computing Helicopter Vortex Wake Distortion*, Massachusetts Institute of Technology ASRL TR–138-1.

[48] Clark, D. and A. Leiper (1970) "The Free Wake Analysis - A Method for the Prediction of Helicopter Rotor Hovering Performance," *Journal of the American Helicopter Society*, **15**(1), pp. 3–11.

[49] Scully, M. (1975) *Computation of Helicopter Rotor Wake Geometry and its Influence on Rotor Harmonic Airloads*, Ph.D. thesis, Massachusetts Institute of Technology, Cambridge, Massachusetts.

[50] Johnson, W. (1980) *A Comprehensive Analytical Model of Rotorcraft Aerodynamics and Dynamics, Part 1: Analytical Development*, NASA TM–81182.

[51] Bliss, D., T. Quackenbush, and A. Bilanin (1983) "A New Methodology for Helicopter Free Wake Analysis," in *Proceedings of the 39nd Forum of the American Helicopter Society*, St. Louis, MO.

[52] Bagai, A. (1995) *Contribution to the Mathematical Modeling of Rotor Flow-Fields Using a Pseudo-Implicit Free-Wake Analysis*, Ph.D. thesis, University of Maryland, College Park, MD.

[53] Vatistas, G., V. Kozel, and W. Mih (1991) "A simpler model for concentrated vortices," *Experiments in Fluids*, **11**(1), pp. 73–76.

[54] Sadler, S. (1971) "A Method for Predicting Helicopter Wake Geometry, Wake-Induced Flow and Wake Effects on Blade Airloads," in *Proceedings of the 39nd Forum of the American Helicopter Society*, Washington, DC.

[55] Bliss, D., M. Teske, and T. Quackenbush (1987) *A New Methodology for Free Wake Analysis Using Curved Vortex Elements*, NASA CR–3958.

[56] Quackenbush, T., D. Wachpress, and A. Boschitsch (1995) "Rotor Aerodynamic Loads Computation Using Constant Vorticity Contour Free Wake Model," *Journal of Aircraft*, **32**(5), pp. 910–920.

[57] Egolf, T. (1988) "Helicopter Free Wake Predictions of Complex Wake Structures Under Blade-Vortex Interaction Conditions," in *Proceedings of the 43rd Forum of the American Helicopter Society*, Washington, DC.

[58] M.J., B. and L. G.J. (2000) "Time-Accurate Modeling of Rotor Wake Using a Free-Vortex Wake Method," AIAA 2000-4120,*18th Applied Aerodynamics Conference*, AIAA, Denver, CO.

[59] Sankar, L., B. Wake, and S. Lekoudis (1986) "Solution of the Unsteady Euler equations for fixed and rotor wing configurations," *Journal of Aicraft*, **23**(4), pp. 283–289.

[60] Agarwal, R. and J. Deese (1987) "An Euler Solver for Calculating the Flowfield of a Helicopter Rotor in Hover and Forward Flight," AIAA 1987-1427, *AIAA 19th Fluid Dynamics, Plasma Dynamics and Laser Conference.*

[61] Wake, B. and L. Sankar (April, 1989) "Solution of Navier-Stokes equations for the flow over a Rotor Blade," *Journal of the American Helicopter Society*, **34**(2), pp. 13–23.

[62] Smith, M. and L. Sankar (1991) "Evaluation of a Fourth-Order Compact Operator Scheme for Euler/Navier-Stokes Simulations of a Rotor in Hover," AIAA 1991-766, *29th Aerospace Sciences Meeting*, AIAA, Reno, Nevada.

[63] Chen, C., W. McCroskey, and S. Obayashi (June, 1991) "Numerical Solutions of Forward Flight Rotor Flow Using an Upwind Method," *Journal of Aircraft*, **28**, pp. 374–380.

[64] Srinicasan, G., J. Baeder, S. Obayashi, and W. McCroskey (October, 1992) "Flowfield of a Lifting Rotor in Hover: A Navier-Stokes Simulation," *AIAA Journal*, **30**(10), pp. 2371–2378.

[65] Duque, E. and G. Srinivasan (1992) "Numerical Simulation of a Hovering Rotor Using Embedded Grids," in *Proceedings of the 48th Forum of the American Helicopter Society*, Washington, DC.

[66] Hariharan, N. and L. Sankar (1994) "Higher Order Numerical Simulation of Rotor Flow Field," in *50th AHS Forum and Technology Display*, Washington, DC.

[67] Ahmad, J. and E. Duque (January-February, 1996) "Helicopter Rotor Blade Computation in Unsteady Flows Using Moving Overset Grids," *Journal of Aircraft*, **33**(1), pp. 54–60.

[68] Steinhoff, J. (1994) "Vorticity Confinement: A New Technique for Computing Vortex-Dominated Flows," in *Frontiers of Computational Fluid Dynamics* (H. M. Caughey, D.A, ed.), chap. 2, Wiley.

[69] Steinhoff, J. and G. Raviprakash (1995) "Navier-Stokes COmputation of Blade-Vortex Interaction Using Vorticity Confinement," AIAA 1995-161, *33rd Aerospace Sciences Meeting and Exhibit*, AIAA, Reno, NV.

[70] Strawn, R. and M. Djomehri (2002) "Computational Modeling of Hovering Rotor and Wake Aerodynamics," *Journal of Aircraft*, **39**(5), pp. 786–793.

[71] Duraisamy, K. and J. Baeder (2007) "High Resolution Wake Capturing Methodology for Hovering Rotors," *Journal of the American Helicopter Society*, **52**(2), pp. 110–122.

[72] Brown, R. (2000) "Rotor Wake Modeling for Flight Dynamic Simulation," *AIAA Journal*, **38**(1), pp. 57–63.

[73] Brown, R. and A. Line (2005) "Efficient High-Resolution Wake Modeling Using Vorticity Transport Equation," *AIAA Journal*, **43**(7), pp. 1434–1443.

[74] Schmitz, S., J. Chattot, M. Bhagwat, M. Moulton, and F. Caradonna (2009) "The Prediction and Validation of Hover Performance and Detailed Blade Loads," *Journal of the American Helicopter Society*, **54**(3), p. 32004.

[75] Jose, A. and J. Baeder (2009) "CFD Simulation of UH-60 Rotor Wake with Trailing Edge Flaps," in *Proceedings of the Army Research Office Rotorcraft Wake Prediction Basic Research Workshop at Georgia Tech.*, Atlanta, GA.

[76] Peters, D. (2009) "How Dynamic Inflow Survives in the Competitive World of Rotorcraft Aerodynamics: The Alexander Nikolsky Honorary Lecture," *Journal of the American Helicopter Society*, **54**(1), p. 11001.

[77] Bramesfeld, G. and M. Maughmer (2008) "A Relaxed Wake Vortex-Lattice Method Using Distributed Vorticity Elements," *Journal of Aircraft*, **45**(2), pp. 560–568.

[78] Basom, B. and M. Maughmer (2011) "Inviscid Analysis of Horizontal-Axis Wind Turbines Using Distributed Vorticity Elements," AIAA 2011-0539, *49th AIAA Aerospace Sciences Meeting*, Orlando, FLorida.

[79] Maniaci, D. and M. Maughmer (2012) "Winglet Design for Wind Turbines Using a Free-Wake Vortex Analysis Method," AIAA 2012-1158, *50th AIAA Aerospace Sciences Meeting*, Nashville, TN.

[80] Chung, K., J. Kim, K. Ryu, K. Lee, and D. Lee (2006) "Sound Generation and Radiation from Rotor Tip-Vortex Pairing Phenomenon," *AIAA Journal*, **44**(6), pp. 1181–1187.

[81] US Army Research, Development, and Engineering Command, Moffett Field, CA 94035-1000 (2011) *RCAS Theory Manual*.

[82] Gray, R. B. (1955) *On the Motion of the Helical Vortex Shed from a Single-Bladed Hovering Model Rotor and its Application to the Calculation of the Spanwise Aerodynamic Loading*, *Tech. Rep. 313*, Princeton University Aeronautical Engineering Department.

[83] Elliot, J., S. Althoff, and R. Sailey (April. 1988) *Inflow Measurements with Laser Velocimetry on a Helicopter Model in Forward Flight; Volume I: Rectangular Planform Blades at an Advance Ratio of 0.15*, NASA TM–100542.

[84] Elliot, J., S. Althoff, and R. Sailey (April. 1988) *Inflow Measurements with Laser Velocimetry on a Helicopter Model in Forward Flight; Volume II: Rectangular Planform Blades at an Advance Ratio of 0.23*, NASA TM–100542.

[85] Elliot, J., S. Althoff, and R. Sailey (April. 1988) *Inflow Measurements with Laser Velocimetry on a Helicopter Model in Forward Flight; Volume III: Rectangular Planform Blades at an Advance Ratio of 0.30*, NASA TM–100542.

[86] Kenyon, A. and R. Brown (2009) "Wake Dynamics and Rotor-Fuselage Aerodynamic Interactions," *Journal of the American Helicopter Society*, **54**(1), pp. 1–18.

[87] Bagai, A. and G. Leishman (1995) "Rotor Free-Wake Modeling Using a Pseudoimplicit Relaxation Algorithm," *Journal of Aircraft*, **32**(6), pp. 1276–1285.

[88] Straub, F., D. Kennedy, D. Domzalski, H. Ahmed, H. Ngo, V. Anand, and T. Birchette (2004) "Smart Material-Actuated Rotor Technology-SMART," *Journal of Intelligent Material Systems and Structures*, **15**(4), pp. 249–260.

[89] barnes, J. and P. Hut (1986) "A Hierarchical $\mathcal{O}(n \log n)$ Force Calculation Algorithm," *Nature*, **324**(4), pp. 446–449.

[90] Greengard, L. and V. Rokhlin (1997) "A Fast Algorithm for Particle Simulations," *Journal of Computational Physics*, **135**(2), pp. 280–292.

Vita

Tenzin Choephel

Tenzin Choephel was born in India to Tibetan refugee parents. He completed his K-12 education at the Tibetan Children's Village in the Northern Indian town of Dharamsala. After obtaining a bachelor's degree in Aeronautical Engineering, Tenzin joined the Indian Institute of Science in Bangalore as a project associate and worked on a few interesting projects involving wind-tunnel tests and the development of micro air vehicles. He then went to the United States for graduate studies and obtained his master's degree in Aerospace Engineering from the Pennsylvania State University with a focus on experimental aerodynamics. The Penn State Aerospace Engineering Department has employed him as a teaching assistant and a graduate research assistant during the course of his doctoral studies. At the same time, he has been serving as a board member of Tibetan Scientific Society which is a non-profit organization dedicated to promoting advanced scientific education in the exile Tibetan society since 2009.